

AFM Studies of Smectic Liquid Crystals

— Focal Conic Domains in Smectic Films

Dissertation

zur Erlangung des mathematisch-naturwissenschaftlichen Doktorgrades

“Doctor rerum naturalium”

der Georg-August-Universität Göttingen

vorgelegt von

Wei Guo

aus Jinan (Shandong), China

Göttingen, 2009

Referent : Prof. Dr. Christoph F. Schmidt

Koreferent : Prof. Dr. Stephan Herminghaus

Tag der mündlichen Prüfung :

TO MY DEAR

PARENTS

&

SHAOXIAN

Abstract

This thesis presents an experimental study of focal conic domains in smectic liquid crystal films on solid substrates. Focal conic domains are complex structures in smectic phases and are likely to play an important role in the future development of novel self-assembling soft matter systems. In smectic films on solid substrates, the generation of focal conic domains can be enforced by antagonistic molecular anchoring conditions at the film interfaces, i. e., random planar at the substrate interface and homeotropic at the air interface. The variation of the anchoring conditions at the substrate interface and the resulting influence on the morphology, properties, and spatial arrangement of focal conic domains were the main objects of the present study.

The relation between the diameter of the focal conic domains, the thickness of the smectic film, and the anchoring strength of the substrate has been studied. The strength of the planar anchoring on the solid substrate was systematically varied by coating the substrates with special alkoxy silane compounds. For each anchoring strength value, the relation between the size of the focal conic domains and the film thickness was determined. Analyzing the experimental results by a theoretical model enabled the quantitative determination of the strength of the planar anchoring of the smectic phase on the substrate.

The curved arrangement of the smectic layers in focal conic domains leads to a depression in the film/air interface above each domain. The depth of these depressions enables to estimate the magnitude of the elastic modulus controlling the dilation or compression of the smectic layers. The depression depth was measured in different smectic phases and at different phase transitions. In some cases, e. g., at second-order smectic-A – nematic transitions, a pronounced temperature dependence of the depression depth was observed, indicating a softening of the smectic layers.

A method to prepare anchoring patterns on the substrates is described. The substrates were structured in a way that areas with homeotropic anchoring conditions alternate with areas

possessing random planar anchoring conditions. When smectic films were prepared on such substrates, focal conic domains formed only on the planar anchoring areas, i. e., the anchoring pattern was translated into a presence-and-absence pattern of focal conic domains. The lateral dimensions of the planar anchoring areas determined an upper limit for the diameter of the focal conic domains. Thus, almost arbitrary two-dimensional arrangements of focal conic domains can be achieved by controlling the size and position of individual domains.

Smectic liquid crystal films have been also studied on crystalline substrates with uniaxial planar anchoring conditions. On such substrates, all liquid crystal molecules are aligned parallel to the surface and point into one direction. In thin smectic films on these substrates, linear domains with a hemicylinder-like shape were observed. The relation between the film thickness and the distance and depth of the hemicylinder structures was studied. In thicker films, the linear domains are decorated with a complex corrugated pattern, which becomes more pronounced on further increasing the thickness, and finally ends with the formation of circular focal conic domains.

Kurzzusammenfassung

Die vorliegende Arbeit beschäftigt sich mit der experimentellen Untersuchung von fokalkonischen Domänen in smektischen Flüssigkristallfilmen auf festen Substraten. Fokalkonische Domänen sind komplexe Strukturen in smektischen Phasen, die eine wichtige Rolle in der zukünftigen Entwicklung von neuartigen weichen selbstorganisierenden Systemen spielen könnten. Die Bildung von fokalkonischen Domänen kann in smektischen Filmen durch antagonistische molekulare Verankerungsbedingungen an den Grenzflächen — planare Verankerung ohne Vorzugsrichtung am Substrat und homöotrope Verankerung an der freien Oberfläche — erzwungen werden. Die Variation der Verankerungsbedingungen an der Grenzfläche zum Substrat und der daraus resultierende Einfluss auf die Morphologie, die Eigenschaften und die räumliche Anordnung der fokalkonischen Domänen war der wesentliche Gegenstand der vorliegenden Untersuchung.

Der Zusammenhang zwischen dem Durchmesser der fokalkonischen Domänen, der Dicke der smektischen Filme und der Verankerungsstärke auf der Substratoberfläche wurde untersucht. Die Beschichtung der Substrate mit bestimmten Alkoxysilanverbindungen ermöglichte eine systematische Variation der Stärke der planaren Verankerung auf dem festen Substrat. Für jeden Wert der Verankerungsstärke wurde die Grösse der fokalkonischen Domänen als Funktion der Filmdicke bestimmt. Die Analyse der experimentellen Daten mithilfe eines theoretischen Modells ermöglichte die quantitative Bestimmung der planaren Verankerungsstärke der smektischen Phase auf dem Substrat.

Die Krümmung der smektischen Schichten in fokalkonischen Domänen führt zu einer Vertiefung in der Film/Luft-Grenzfläche über jeder Domäne. Aus dem Betrag der Tiefe dieser Vertiefungen lässt sich die Grösse des Elastizitätsmoduls abschätzen, der die Dehnung und Kompression der smektischen Schichten kontrolliert. Die Tiefe der Vertiefungen wurde in verschiedenen smektischen Phasen und an verschiedenen Phasenübergängen gemessen. In einigen Fällen, beispielsweise an smektisch-A – nematisch Phasenübergängen zweiter Ordnung,

wurde eine ausgeprägte Temperaturabhängigkeit der Tiefe beobachtet, die auf eine starke Abnahme des Elastizitätsmoduls bzw. ein Weichwerden der der smektischen Schichten hindeutet.

Eine Methode zur Herstellung von Mustern aus verschiedenen Verankerungsbedingungen auf den Substraten wurde beschrieben. Dazu wurden die Substrate in der Weise strukturiert, dass auf der Oberfläche sowohl Flächen mit homöotroper Verankerung als auch Flächen mit planarer Verankerung vorhanden sind. Wenn smektische Filme auf solchen Substraten präpariert werden, bilden sich fokalkonische Domänen nur auf den Oberflächen mit planarer Verankerung. Die seitlichen Abmessungen der Substratflächen mit planarer Verankerung legen die Obergrenze für den Durchmesser der fokalkonischen Domänen fest. Auf diese Weise kann sowohl die Position als auch die Grösse einzelner Domänen kontrolliert werden, sodass sich fast beliebige zweidimensionale Anordnungen von fokalkonischen Domänen erzeugen lassen.

Weiterhin wurden smektische Flüssigkristallfilme auf kristallinen Substraten untersucht, die planare Verankerungsbedingungen in Kombination mit einer bevorzugten Ausrichtung der Moleküle aufweisen. Auf diesen Substraten ordnen sich die Flüssigkristallmoleküle parallel zur Substratoberfläche an und orientieren sich zusätzlich mit ihren Längsachsen parallel zu dieser Vorzugsrichtung. In dünnen smektischen Filmen auf solchen Substraten wurden lineare Domänen beobachtet, in denen die smektischen Schichten konzentrische Halbzylinderstrukturen bilden, wobei die freie Oberfläche eine wellblechartige Form zeigt. Der Zusammenhang zwischen der Filmdicke und der Breite der linearen Domänen sowie der Tiefe der linearen Vertiefungen an der freien Oberfläche dieser Filme wurde untersucht. Mit zunehmender Filmdicke sind komplexere Strukturen zu beobachten, die schliesslich in zirkulare fokalkonische Domänen übergehen.

Contents

Abstract	i
Kurzzusammenfassung	iii
Contents	vi
List of Figures	xv
List of Tables	xvii
Introduction	3
1 Physical Background	5
1.1 Liquid Crystals	5
1.2 Structure of Nematic and Smectic Phases	7
1.3 Continuum Description of Liquid Crystals	12
1.4 Anchoring of Liquid Crystals at Interfaces	14
1.4.1 Anchoring on Solid Substrates	16
1.4.2 Microscopic Anchoring Mechanisms at Solid Substrates.	18
1.5 Focal Conic Domains in Smectic Liquid Crystals	19
1.5.1 Defect Structures in Smectic Phases	19
1.5.2 Focal Conic Domains in Thin Films and Microchannels	21
1.5.3 Model for The Energy of A Focal Conic Domain in Thin Films	24
2 Materials, Methods and Experimental Techniques	29
2.1 Liquid Crystal Materials	29
2.2 Preparation Methods	31
2.2.1 Substrate Preparation	31
2.2.2 Sample Preparation	36
2.3 Characterization Techniques	37
2.3.1 Optical Microscopy	37
2.3.2 Fluorescence Confocal Microscopy	37

2.3.3	Atomic Force Microscopy (AFM)	42
3	Focal Conic Domains in Films on Homogenous Substrates	61
3.1	Influence of Film Thickness and Anchoring Strength	62
3.2	Behaviour of Focal Conic Domains at Phase Transitions	70
3.2.1	Formation of Focal Conic Domains at Isotropic to Smectic-A and Nematic to Smectic-A Transitions	70
3.2.2	Behaviour of The Depth of The Domain-Induced Depressions in The Free Surface	74
3.2.3	Relation to The Layer Elastic Modulus B	83
4	Focal Conic Domains in Films on Patterned Substrates	91
4.1	Behavior on Linearly Patterned Substrates	92
4.2	Behavior on Circularly Patterned Substrates	97
4.3	Behavior of The Surface Depressions in Thick Films on Patterned Substrates	104
5	Structure Formation in Smectic Films on Crystalline Substrates	109
5.1	Smectic Liquid Crystal Films on Mica Substrates	110
5.2	Smectic Liquid Crystal Films on MoS ₂ Substrates	113
5.2.1	Film Thickness Dependence of The Linear Structures on MoS ₂ Substrates	113
5.2.2	Fluorescence Confocal Microscopy of Smectic Liquid Crystal Films on MoS ₂ Substrates	115
6	Summary and Outlook	123
	Appendices	127
	A Symbols and notations	129
	References	133
	Acknowledgments	141

List of Figures

1.1	Schematic representation of molecular order in the isotropic liquid, nematic, smectic and crystalline phases. The axis indicates the direction of increasing temperature.	7
1.2	Schematic structure of the molecular arrangement of the smectic- <i>A</i> and smectic- <i>C</i> phase.	9
1.3	(a) Schlieren texture of the nematic phase and (b) focal conic texture with maltese crosses of the smectic- <i>A</i> phase.	10
1.4	Binary phase diagram of 8CB/10CB mixtures. Solid and dashed lines are, respectively, second- and first-order transitions. TCP is the smectic- <i>A</i> – nematic tricritical point. Vertical dashed lines indicate the measured mixtures (from [18]).	11
1.5	The scheme of three fundamental distortions in a nematic liquid crystal (cf. [15]).	12
1.6	Temperature dependence of the layer compressional modulus <i>B</i> for 8CB near the transition to the nematic phase at ≈ 33.6 °C (from [37]).	15
1.7	Temperature dependence of the layer compressional modulus <i>B</i> for the compound 10BIMF9 near a smectic- <i>C</i> – smectic- <i>A</i> transition (from [49]).	15
1.8	Schematic orientation of the liquid crystal molecules at an interface for homeotropic and planar anchoring.	17
1.9	Schematic construction of a focal conic domain: (a) confocal domains degenerated into a cylinder. (b) Toric focal conic domain, singular lines are a circle and a straight line. (c) The general case with an ellipse and a hyperbola as singular lines, the layers form parallel Dupin cyclides (cf. [81]).	20

1.10	Schematic drawing of two neighbouring focal conic domains in a film with homeotropic (top interface) and degenerate planar (bottom interface) anchoring conditions. The smectic layers are wrapped around two singular lines (in this drawing, a straight line and a circle).	21
1.11	Polarized light microscopy images of ordered focal conic domains of smectic 8CB in surface-modified microchannels (Inset images are magnified $\times 2$), with corresponding schematic drawings shown above and below the images. From left to right, the widths of the channels are 20, 10, and 5 μm . In a-c, the channel depth is 10 μm . In d-f, the depth is 5 μm . (Magnification: $\times 400$, from [86].)	22
1.12	Schematic drawing of the hemicylinder arrangement of the smectic layers on a planar anchoring substrate with a preferred in-plane aligning direction. . . .	24
1.13	Schematic cross section through a toric focal conic domains with diameter $2r$ in a smectic film of thickness H . The bend deformation of the smectic layers leads to a depression in the film/air interface with depth h . If the cross sections of the layer planes form concentric circles, the value of h is easily calculated according to the Pythagorean theorem (triangle indicated by the dashed lines).	25
2.1	Molecular formulae of liquid crystals used in the experiments.	32
2.2	AFM image of gold patterned silicon substrate masked by copper grid.	34
2.3	AFM images of the gold patterned silicon substrate masked by different size of microbeads. The size of the microbeads used in experiments is (a) 0.5, (b) 2, (c) 6, and (d) 10 μm , respectively.	35
2.4	Optical microscope Leica DM4000C with TMS 94 temperature controllers and THMSG600 heater stage.	38
2.5	Optical microscopy with polarized light of (a) nematic phase and (b) smectic-A phase of 8CB droplet on silicon substrate.	39
2.6	Scheme of the work principle of fluorescence confocal microscopy (from http://www.olympusfluoview.com/).	40
2.7	Photo of fluorescence confocal microscopy Leica TCS SP2.	40
2.8	Scheme of the work principle of fluorescence confocal microscopy, cf. [100].	41
2.9	Schematic representation of an AFM operation principle. Note that the sizes of the tip and the cantilever are strongly enlarged with respect to other sizes, cf. [108].	43
2.10	Plot of Lennard-Jones potential qualitative form, cf. [110].	44

2.11	Normalized plot of the forces between the tip and sample, highlighted areas are the typical imaging mode ranges (see http://www.veeco.com/).	44
2.12	The comparison scheme of three kinds of AFM working modes: contact mode, non-contact mode, and Tapping TM mode.	45
2.13	Atomic force microscope (Multi Mode V) purchased from Veeco Instruments.	48
2.14	OMCL160TS Tapping TM mode cantilever, Olympus, Japan. The cantilever is 4.6 μm thick, 160 μm long, 50 μm wide. The height of tip is 11 μm and radius is less than 10 nm.	48
2.15	The approaching curve presenting the variation of the amplitude of the oscillating tip moving toward and withdrawing from the surface. The driving amplitude is 2 V, and tip spring constant is 66 N/m.	49
2.16	(a) A series of sweeping curves (resonance frequency of tip vs. amplitude) of different γ_{sp} values. γ_{sp} reduced gradually from top to bottom. (b) The shifting curve of frequency with different γ_{sp} values. The driving amplitude is 2 V, and tip spring constant is 66 N/m.	51
2.17	The profile of 10CB droplet on bare silicon substrate. The γ_{sp} from top to bottom are 0.87, 0.85, 0.7, 0.5, 0.4, 0.35 and 0.3 respectively. The driving amplitude is 2V, and tip spring constant is 66 N/m, and scan rate is 0.2 Hz. . .	52
2.18	The depth of smectic-A defects obtained by AFM measurements scanned with different γ_{sp}	53
2.19	The approaching curve of a tip, spring constant 66 N/m, oscillating with driving amplitude 2 V (black) and 4 V (red).	54
2.20	The shifting curves of frequency, corresponding to γ_{sp} , of tip drove by different amplitudes. For the sake of observation conveniently, the values of each curve are divided by a factor.	55
2.21	The profile of 10CB droplet on bare silicon substrate. The γ_{sp} is 0.85 and the driving amplitudes of tip from top to bottom are 1 V, 2 V, 3 V, 4 V, 5 V and 6 V respectively. The driving tip spring constant is 66 N/m, and scan rate 0.2 Hz.	56
2.22	The variation of the difference of the thickness of 10CB droplet measured by sequential scanning at different scan rates (spring constant 66.14 N/m).	57
2.23	The different scanning regions corresponding to the driving amplitude and γ_{sp} with a tip (a) $k = 66.14$ N/m and (b) $k = 8.753$ N/m. The lines are used to guide for eye.	58

3.1	(a) Optical micrograph of a smectic film of 10CB in which focal conic domains form a hexagonal lattice. (b) AFM image of the smectic 10CB film with focal conic domains. (c) Cross section of the AFM image, indicating the depressions at the air interface induced by the focal conic domains.	62
3.2	Optical microscopy image of a smectic 8CB film on a PEI-coated silicon substrate.	63
3.3	Dependence of diameter $2r$ of focal conic domains on the local film thickness H in films on three different substrates (bare silicon, PEI-coated silicon, MAP-coated silicon).	64
3.4	Dependence of focal conic domain diameter $2r$ on the local thickness H of 8CB smectic films on two substrates coated with different mixtures of MAP and DMOAP. Small dots: $x_{DMOAP} = 0.7 \times 10^{-4}$. Open symbols: $x_{DMOAP} = 4.0 \times 10^{-4}$ (the values of x_{DMOAP} refer to the mole fraction of DMOAP in MAP). Solid lines are fits according to Equation 3.2.	66
3.5	Dependence of planar anchoring strength $\Delta\sigma_{sub}$ on the mol fraction of DMOAP in the substrate coating for the LC compounds 8CB (\circ), 9CB ($*$), and a 6CB/8CB mixture corresponding to 7.5CB (\diamond).	67
3.6	Values of $\Delta\sigma_{sub}$ as a function of temperature for 8CB on a MAP-coated silicon substrate. $\Delta\sigma_{sub}$ remains almost constant, except for a slight decrease near the transition point.	69
3.7	Fluorescence confocal microscopy images of the formation of focal conic domains in 10CB smectic film on bare silicon substrate around smectic-A – isotropic phase transition temperature 44°C	71
3.8	Thickness dependence of the size of focal conic domains in smectic 10CB films on bare silicon substrates. The diameter $2r$ was measured by AFM and the thickness was determined by fluorescence confocal microscopy.	72
3.9	Optical microscopy image and AFM image of smectic 8CB film on a bare silicon substrate, demonstrating the size distribution of focal conic domains when formed at a nematic to smectic-A transition.	73
3.10	Diameter $2r$ of focal conic domains as function of film thickness H of smectic 8CB films on a bare silicon substrate with random planar anchoring. The small dots are data taken from AFM measurements, and data with bars at larger H values are from optical microscopy reflection measurements (the bars indicate approximately the size distribution of the focal conic domains).	74

- 3.11 AFM images and the cross section of the focal conic domain of a smectic 8CB film on a bare silicon substrate. Figure (a) shows a focal conic domain formed at a larger thickness with $H > 5 \mu\text{m}$. Figure (b) shows a focal conic domain at a smaller local thickness ($H < 2 \mu\text{m}$). 75
- 3.12 Fluorescence confocal microscopy image of a single focal conic domain in a smectic 10CB film on a bare silicon substrate. The small image in the right top corner is a magnified image of the depression induced by the focal conic domain at air interface. 75
- 3.13 Schematic cross section through a toric focal conic domain with diameter $2r$ in a smectic film of thickness H . The bend deformation of the smectic layers leads to a depression at the film/air interface with depth h . If the cross sections of the layer planes form concentric circles, the value of h is easily calculated according to the Pythagorean theorem (triangle indicated by the dashed lines). 76
- 3.14 Temperature dependence of the depth h of the domain-induced depressions at the air interface of (a) a 10CB film on a PEI-coated silicon substrate; (b) a 8CB film on a PEI-coated silicon substrate, where h decreases continually and probably vanishes at the transition to the nematic phase. 77
- 3.15 Temperature dependence of h of focal conic domains of Pyp9O7, and Pyp8O8 on bare silicon substrates. 78
- 3.16 Temperature dependence of the ratio h/h_0 (h : measured depth of the domain-induced surface depressions, h_0 : calculated values using Equation 3.5) in $\approx 40 \mu\text{m}$ thick films of the compounds 12CB (\bullet), A7 (\circ), C7 (\blacksquare), 10CB (\diamond), $\bar{8}.S.5$ (\blacktriangle), and 8CB (\square). $T_{A \leftrightarrow N/I}$ designates the smectic-A – nematic or smectic-A – isotropic transition temperature. 81
- 3.17 Temperature dependence of the ratio h/h_0 (h : measured depth of the domain-induced surface depressions, h_0 : calculated values using Equation 3.5) in $\approx 40 \mu\text{m}$ thick films of the compounds 10CB (\diamond), 8CB (\square), and three 8CB/10CB mixtures with x_{10CB} equal to 0.25 ($*$), 0.5 ($+$), and 0.75 (\blacklozenge). $T_{A \leftrightarrow N/I}$ designates the smectic-A – nematic or smectic-A – isotropic transition temperature. 82
- 3.18 Temperature dependence of the ratio h/h_0 (h : measured depth of the domain-induced surface depressions, h_0 : calculated values using Equation 3.5) in $\approx 40 \mu\text{m}$ thick films of the compounds A7 (\circ), C7 (\blacksquare), and $\bar{8}.S.5$ (\blacktriangle). $T_{C \leftrightarrow A}$ designates the smectic-C – smectic-A transition temperature. 83

3.19	Temperature dependence of the depth h of the domain-induced surface depressions in a smectic 8CB film with a thickness of $\approx 42 \mu\text{m}$ on a MAP-coated substrate. The heating (red \blacktriangle) and cooling (blue \bullet) cycle shows a slight hysteresis.	85
3.20	Solid lines: values of h/h_0 as function of modulus B , calculated using Equations 3.7 and 3.10 with $\sigma_{air} = 0.03 \text{ N/m}$, $H = 45 \mu\text{m}$, and $r = 5 \mu\text{m}$ or $r = 10 \mu\text{m}$. For the dashed lines, the intrinsic dilation sheath (see text) of the focal conic domains was additionally taken into account. Grey areas: experimental values of h/h_0 (this study) and B (determined with second sound measurements, from [38]) for the compounds 8CB and $\bar{8}.S.5$	87
4.1	Optical microscopy images of grid masks (left) and corresponding gold coated silicon substrates (right).	93
4.2	Top: the optical microscopy image of the TEM grid used to fabricate the pattern in the bottom image. Bottom: the optical microscopy image of 8CB focal conic domains on a patterned substrate produced by the top TEM grid. The arrows shown in top and bottom images indicate the same deformed curve in the produced pattern as in the grid. Focal conic domains are arrayed along this curve.	95
4.3	AFM image of a smectic 8CB film on patterned substrates with squares, hexagons or linear arrays of focal conic domains.	96
4.4	Top: AFM image of a smectic 8CB film on a silicon substrate patterned with gold-coated squares. The coated areas are separated by $12 \mu\text{m}$ wide bare silicon stripes. The image shows two stripes crossing. Bottom: cross section along the dashed blue line in the AFM image. Each depression at the interface is induced by an underlying focal conic domain.	97
4.5	Left: AFM images of smectic 8CB films on gold coated silicon substrate with $20 \mu\text{m}$ wide stripes of the bare silicon surface; The film thickness increases from $3 \mu\text{m}$ (top) over $5 \mu\text{m}$ (middle) to $15 \mu\text{m}$ (bottom); the corresponding increase of the diameter of the focal conic domains results in the formation of 3-row, 2-row, and single-row arrays of focal conic domains. Note that free space in the stripe areas is sometimes filled with tiny satellite focal conic domains (middle and bottom image, indicated by the blue arrows). Right: cross sections along the dashed blue lines in each AFM image.	98

- 4.6 Fluorescence confocal microscopy images of smectic 8CB films on TEM patterned gold coated substrates. The thickness of the film is (a) $< 1 \mu\text{m}$, (b) $2 \mu\text{m}$, (c) $3 \mu\text{m}$, and (d) $> 18 \mu\text{m}$, and focal conic domains formed 4-row, 3-row, 2-row, and single-row arrays, respectively. 99
- 4.7 AFM images of gold patterns on silicon fabricated by microbead masks and 8CB film on such patterns. The size of microbeads used as masks is (a) $0.5 \mu\text{m}$, (b) $2 \mu\text{m}$, (c) $6 \mu\text{m}$, and (d) $10 \mu\text{m}$. With the exception of the $0.5 \mu\text{m}$ case, the diameter of the focal conic domains is equal to the diameter of each circular pattern. . . 100
- 4.8 AFM images (top) and reflection confocal microscopy images (bottom) of 8CB smectic film on the patterned substrate fabricated by $6 \mu\text{m}$ microbeads. The left image shows the region close to the film edge with the bare silicon at the left top corner. The right image shows a slightly thicker region of the same film. In thin film, several focal conic domains are restricted in one circular pattern. In the thicker film, one focal conic domain occupies one circular pattern, and the diameter remain as large as the circular pattern. 101
- 4.9 Diameter $2r$ of focal conic domains as function of film thickness H for 8CB films on the patterned substrate fabricated by $6 \mu\text{m}$ microbeads. The small dots are data taken from AFM measurements, data with bars at larger H values are from optical microscopy, the red line indicates the position of the data of 8CB on bare silicon substrates without anchoring pattern (see Figure 3.10). 102
- 4.10 Fluorescence confocal microscopy image of 8CB smectic film on the patterned substrate fabricated by $6 \mu\text{m}$ microbeads. The left top image presents a hexagonal array of focal conic domains. And a series images at the right bottom shows the cross section of a single focal conic domain in films with different thickness. 103
- 4.11 Depth h of the surface depressions induced by focal conic domains as a function of thickness H of films on a circularly patterned substrate prepared with $6 \mu\text{m}$ polystyrene microbead monolayer. Solid dots: experimental values determined by AFM; black line: calculated values according to Equation 4.1 with $r = 3 \mu\text{m}$; grey line: calculated values according to Equations 4.2 and 4.3 with $r = 3 \mu\text{m}$, $\sigma_{air} = 30 \text{ mN/m}$, $B = 1.3 \times 10^7 \text{ N/m}^2$, and $h_0 = H - \sqrt{H^2 - r^2}$ 105
- 4.12 Temperature dependence of the depth h of the domain-induced surface depressions in films on substrates with $6 \mu\text{m}$ circular anchoring patterns. The thickness of the films amounts to $11.3 \mu\text{m}$, $44 \mu\text{m}$, and $73 \mu\text{m}$. T_{AN} designates the smectic-A – nematic transition temperature of 8CB. 106

5.1	Hemicylinder scheme of the linear defect structures in a smectic film on a substrate with unidirectional planar anchoring.	110
5.2	Optical microscopy image of a thin 8CB film on mica at room temperature. The black lines indicate the directions of linear defects.	111
5.3	Optical microscopy image of a droplet of 8CB on mica at room temperature. Near the edge of the droplet (running from the lower left to the upper right corner) linear structures are present while in the thicker regions circular focal conic domains are forming.	112
5.4	AFM images of an 8CB droplet on mica at room temperature (a) near the edge of the droplet, and (b) near the center of the droplet.	112
5.5	AFM images of an 8CB droplet on mica at room temperature. (a) shows the region between linear structures and circular focal conic domains. (b) gives a detail image of (a).	113
5.6	Optical microscopy image of a 8CB film on MoS ₂ at room temperature. Different color lines represent the six different in-plane orientations of the linear structures.	114
5.7	AFM images of a 8CB film on MoS ₂ at room temperature. The different anchoring direction domains are separated by sharp boundaries.	114
5.8	AFM images of smectic 8CB films on MoS ₂ for different film thicknesses. The thickness, estimated by the interference colors of the scanning areas, are respectively (a) < 50 nm, (b) ~ 50 nm, (c) ~ 200 nm, (d) ~ 700 nm, (e) ~ 900 nm, (f) ~ 1100 nm, (g) ~ 1300 nm, and (h) > 2000 nm.	116
5.9	Distance between neighbouring hemicylinder domains and depth of the linear surface depressions as function the film thickness (8CB at room temperature). The thickness was estimated by the inference color of the film. The bottom AFM image depicts the distance D and depth h of the linear structures.	117
5.10	Temperature dependence of the depth h of the linear surface depressions of a smectic 8CB film on MoS ₂	118
5.11	AFM and polarized fluorescence confocal microscopy images of smectic 8CB films (doped with the dye BTBP) on MoS ₂ substrates. From (a) to (c), the thickness of the film increases, and are approximately 200 nm, 1 μ m and 1.5 μ m, respectively.	119

- 5.12 (a) and (c) are polarized fluorescence confocal microscopy images of smectic 8CB films on MoS₂ substrates. The bottom and the right side images of (a) are vertical sections, which were obtained from the vertical scan along the grey lines. The white arrows in (c) indicate the orientation of the plane of polarization. (b) is an AFM image of the corresponding area of the confocal microscopy images. The arrows indicate orientations of the liquid crystal molecules near the MoS₂ substrate which could explain the behaviour observed in the confocal microscope on rotation of the plane of polarization. . . 120

List of Tables

2.1	Liquid crystals used in the experiments and their phase transition temperature (experimental data).	30
2.2	Phase transition of the mixtures of 6CB and 8CB and their phase transition temperatures (experimental data).	30
2.3	Liquid crystals with smectic- <i>C</i> phase, and their phase transition temperature (experimental data).	31
2.4	Contact angles of 8CB and 10CB on bare silicon, PEI and MAP self-assembled silicon substrates.	36
3.1	Film thickness H , domain diameter $2r$ and depth h_0 of the domain-induced surface depression as calculated by Equation 3.5 for the six one-component samples and three binary mixtures under investigation.	80
4.1	The dimension of grid masks used in the experiments. The column ‘width’ refers to the width of the masked stripes.	94

“Live simply with great ambition; Fare serenely toward high goal.”

Zhuge Liang (181 – 234)

Introduction

Since their discovery over one hundred years ago, liquid crystals have attracted large scientific interest. Because of their application in electro-optic displays, these materials are now ubiquitous in everyday life. In fundamental research, besides representing unique partially ordered systems in their own right, liquid crystals are important model systems for the study of phase transitions, correlations in liquids, surface phenomena, wetting, thin films and membranes, and many other fields. The results, findings, and theoretical treatments of liquid crystal research can be widely used in the research of other partially ordered complex systems, like polymers or biological materials.

In recent years, the concept has emerged to use structural features of liquid crystal phases as matrices or templates to control the self-assembly of micro- and nanosystems. Liquid crystal structures comprise a wide range of length scales from a few nanometers (smectic density wave) to hundreds of micrometers (cholesteric helix) and are susceptible to external influences arising, e. g., from electric fields or surface command layers. One example for the use of liquid crystals for the realization of new self-assembling systems is the distortion of the director field of a nematic phase by small water droplets or solid particles. These distortions, which are caused by anchoring the orientation of the liquid crystal molecules on the surface of the droplets or particles, lead to novel long-distance interactions [1] which can be used for the design of new colloidal systems [2].

Whereas the nematic phase is just a liquid in which the molecules show orientational order, smectic phases possess in addition a one-dimensional positional order which can be described as a density wave or weakly defined layer structure. Smectic phases form, in response to weak external perturbations, complex structures called focal conic domains. In focal conic domains, the smectic layers are wrapped around two singular lines which are in general an ellipse and a hyperbola passing through each other focal point. The properties of focal conic domains in bulk smectic phases are well understood, but their targeted generation by surface effects,

their properties in thin films, and their potential as templates for self-assembly are still widely unexplored.

In my thesis, I present an experimental investigation of the fundamental properties of focal conic domains in smectic liquid crystal films on solid substrates. The general goal was to explore possible methods for the targeted generation and for the control of the dimensions and the spatial arrangement of focal conic domains in such films and to study how their behavior depends on properties of the liquid crystal compounds, e. g., on their phase types and phase sequence. Since focal conic domains in smectic films cause characteristic features in the free surface of the film, atomic force microscopy is an important method for my investigation.

My thesis is organized as follows: The first two chapters provide the required physical background and a description of the employed experimental techniques and procedures.

In Chapter 3, I discuss general aspects of the formation of focal conic domains which are induced by antagonistic molecular anchoring conditions at the film interfaces. The relation between the film thickness and the size of the focal domains, the influence of the strength of the molecular anchoring on the focal conic domains, and their behavior at different phase transitions are studied. These studies are carried out — in contrast to the investigations described in the following chapter — on substrates possessing homogeneous conditions on their whole surface.

In Chapter 4, I introduce a method to fabricate anchoring patterns on the substrates, i. e., the surface of these substrates possesses only in some regions those anchoring conditions that lead to the formation of focal conic domains. With this method, it is possible to control the positional arrangement of focal conic domains. Furthermore, confinement effects can be studied since the formation of the focal conic domains can be restricted to a small fraction of the substrate surface.

In the last chapter, preliminary results will be reported which concern the formation of structures in smectic films on crystalline substrates. In contrast to the substrates used in the preceding chapters, crystalline substrates impose a certain in-plane aligning direction to the liquid crystal molecules which leads to the formation of new linear defect domains.

Chapter 1

Physical Background

“Anything one man can imagine, other men can make real.”

Jules Verne (1828 – 1905)

1.1 Liquid Crystals

Exhibiting properties between those of a conventional liquid and those of a solid crystal, liquid crystals have attracted enormous scientific research interests since they were discovered by the Austrian botanical physiologist Friedrich Reinitzer and the German physicist Otto Lehmann in 1888 [3]. Many fundamental properties of liquid crystals were explored already in the 1920s [4], but then the interest in these materials calmed down. In 1957, an article published by the American chemist Glenn H. Brown [5] on the liquid crystalline state sparked an international resurgence in liquid crystal research. The door for optical applications of liquid crystals was opened in the 1970s with the demonstration of the electro-optical effect by Schadt and Helfrich [6] and the synthesis of chemically stable liquid crystals with low melting temperatures by George Gray [7]. Since then, the use of liquid crystals in display industry [8–10] and thermography [11] is steadily growing, in turn triggering the growth of scientific research on liquid crystals [12].

As now well known, liquid crystalline phases, also called mesophases, possess an orderly intermediate state between the crystalline state and the isotropic liquid phase. Liquid crystalline phases correspond in some sense to liquid phases, e. g., they can still flow like a liquid. On the other hand, they exhibit anisotropic physical properties which are usually found only in solids, like optical birefringence or static torques transmission.

Liquid crystals cover a wide range of chemical structures [13], including rod-like molecules, disc-like molecules, metallomesogens, amphiphilic compounds, and biomaterials like cellulose derivatives, steroids, glycolipides, etc.. Two main classes of liquid crystal materials are distinguished: thermotropic and lyotropic liquid crystals. Lyotropic liquid crystals are always multi-component systems, e. g., amphiphilic molecules in water, which self-assemble to different kinds of ordered phases. The composition and the temperature are the essential variables of state. My study concerns thermotropic liquid crystals. These materials are composed of organic, asymmetric molecules, i. e., rod-like or disc-like molecules, and can form liquid crystal phases as one-component systems. The temperature alone is the essential state variable.

Thermotropic liquid crystals can show, with changing temperature, one or a sequence of several liquid crystalline phases with different degrees of order. Figure 1.1 shows the schematic structures of isotropic liquid, nematic, smectic and crystalline phases. At high temperatures, the liquid crystal compounds are in the isotropic liquid phase (shown in Figure 1.1 (a)) and possess the same properties as ordinary liquids. Upon cooling, a first-order phase transition to the nematic phase can occur (Figure 1.1 (b)). The nematic phase is a liquid, but the molecules possess a long-range orientational order. X-ray observations of the nematic phase reveal that a positional order does not exist, but the asymmetrically shaped molecules are on average aligned along a single direction, causing an anisotropy of the physical properties. With further cooling, a phase transition to a smectic phase can occur (Figure 1.1 (c)). Smectic phases possess, in addition to the long range orientational order of the nematic phase, a positional order in one spatial direction which can be described as a layered structure. X-ray show, that this positional order can be characterized as a quasi long range order. At still lower temperatures, liquid crystal compounds form solid crystals like ordinary organic substances (Figure 1.1 (d)).

The presence of chiral molecules can influence the structure of liquid crystal phases. For instance, if chiral molecules are added to a nematic phase (or if the chiral compound itself forms a nematic phase), the so-called cholesteric phase is obtained. In this phase, a helical superstructure is present, i. e., the direction of the parallel nematic ordering rotates if one proceeds perpendicular to this direction.

Different liquid crystal compounds can show different types of phase transition sequences. For example, a sequence of crystal – smectic – nematic – isotropic has been given above, but liquid crystals with the sequence crystal – nematic – isotropic or crystal – smectic – isotropic can also be found. Liquid crystals with different phase transition sequences exhibit different

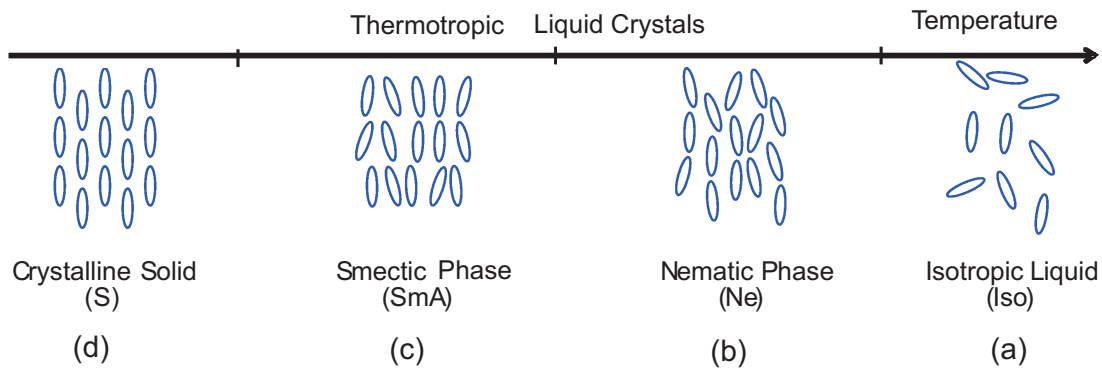


Figure 1.1: Schematic representation of molecular order in the isotropic liquid, nematic, smectic and crystalline phases. The axis indicates the direction of increasing temperature.

properties, which will be elaborated further in following sections. My study concerns mainly properties of smectic phases and the behaviour at smectic – nematic and smectic – isotropic phase transitions.

1.2 Structure of Nematic and Smectic Phases

First studied in detail by Friedel [14], nematic and smectic phases are important and common mesophases studied and applied nowadays.

In the study of liquid crystals, two parameters are important to describe the bulk state of liquid crystals [15]. The first is called the director \mathbf{n} , which represents the orientation of the average direction of the long molecular axes in the liquid crystal bulk phase. It gives the average orientation of the molecules in a volume v_0 , which is small compared with the dimension of the system and large compared with the molecule's scale. Liquid crystals are easily influenced by external distortions, resulting in a variation of the director orientation in space describable by a director field $\mathbf{n}(\mathbf{r})$. The second parameter is the order parameter S , which characterizes the distribution of the orientations of the molecules. It is defined as the average $\langle(3 \cos^2 \theta - 1)/2\rangle$ over all molecules in the volume v_0 , where θ is the angle between the long axis of an individual molecule and the director \mathbf{n} . S is equal to 1 when all the molecules are aligned parallel to \mathbf{n} , and to 0 when the distribution of orientations is isotropic. For example, in the bulk nematic phase, S is of the order of 0.4 just below the nematic – isotropic transition and increases with decreasing temperature to values of 0.6 to 0.8 [16].

The phase transition from the isotropic to the nematic phase is always observed to be

a first-order transition, i. e., the order parameter S is discontinuous at the transition. The magnitude of S jumps from zero in the isotropic phase to the value mentioned above (≈ 0.4) in the nematic phase just below the transition.

Nematic liquid crystals exhibit anisotropic physical properties, e. g., they are optically uniaxial birefringent. The magnitude of the anisotropy, e. g., the difference $\Delta n = n_e - n_o$ between extraordinary and ordinary refractive index, is proportional to the order parameter S . Other anisotropic properties are the magnetic and the dielectric susceptibilities. This results, in combination with the liquid nature of the nematic phase, in the feature that the orientation of the director \mathbf{n} can be easily aligned by external magnetic or electric fields. This is the base of the application of the nematic phase in electro-optical displays [10], since \mathbf{n} corresponds to the optical axis of the material.

As shown in Figure 1.1, smectic phases possess a layered structure, in which molecules are restricted in planes with a well-defined interlayer spacing. The interaction between the layers are weak and the layers slide easily over each other. The smectic order can also be described as a one-dimensional density wave with the wave vector corresponding to the layer normal and the wavelength to the layer thickness.

According to the arrangement of molecules within the layers and the orientation of the director \mathbf{n} with respect to the layer normal \mathbf{z} , a large number of distinct smectic phases can be identified, macroscopic textures of which are readily recognized by polarized optical microscopy [17]. The most common smectic phase is the smectic-A phase. In the smectic-A phase (see Figure 1.2), the molecules are perpendicular to the smectic plane, i. e., \mathbf{n} is parallel to \mathbf{z} . There is no particular positional order in the layer, each layer can be regarded as a two-dimensional liquid. The smectic-C phase is a tilted form of smectic-A phase, i. e., the molecules are arranged as in the smectic-A phase, but \mathbf{n} is tilted by an angle θ with respect to \mathbf{z} . If the smectic-C is made of chiral molecules (it is then designated as smectic-C*), the azimuthal direction of the tilt builds up a helical structure as one proceeds along \mathbf{z} (unless mentioned otherwise, chiral molecules are not considered in this thesis).

There are also smectic phases in which the positions of the molecular mass centers are arranged in a short-range hexagonal positional order within a given layer and the orientation of the local hexagons is ordered on a long range; these are the hexatic phases smectic- B_{hex} , F , and I . Finally, some compounds show at lower temperatures layered phases with a three-dimensional long-range positional order. Initially designated as higher-ordered smectic phases, these phases are now considered as crystals: B_{cryst} , G , J , E , H , and K . The difference from ordinary crystals consists in a rotational disorder around the long axis, similar as in the

rotator phases of alkanes.

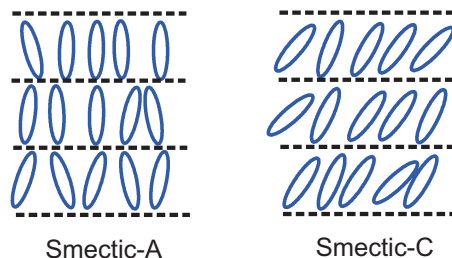


Figure 1.2: Schematic structure of the molecular arrangement of the smectic-A and smectic-C phase.

Under a polarizing optical microscope, nematic and smectic phases exhibit unique textures. When a liquid crystal sample is prepared between two glass slides with planar anchoring conditions, the director \mathbf{n} is parallel to substrates but can point in different in-plane directions. In the nematic phase, a so-called schlieren texture is then obtained between crossed polarizers (Figure 1.3 (a)) [17]. The dark brushes shown in the schlieren texture correspond to the extinction orientation of \mathbf{n} , i. e., \mathbf{n} lies either parallel or perpendicular to the polarizer or analyzer axes. Rotating the sample, the black brushes rotate continuously indicating a continuous change of the orientation of \mathbf{n} .

For smectic liquid crystals (Figure 1.3 (b)), more complex textures are observed in comparison to nematics. The most typical textures for the smectic-A phase are the so-called fan-shaped texture and the so-called maltese-cross texture. Both textures result from the spontaneous formation of focal conic domains, which will be discussed in detail in Section 1.5.

With decreasing temperature, the smectic-A phase can be entered either from the nematic phase or from the isotropic phase, depending on the liquid crystal compound. The smectic-A – isotropic transition is always first-order. The smectic-A – nematic transition is in most cases a second-order transition. The order parameter of the transition, the amplitude of the smectic density wave, decreases continuously to zero, following a power law, as the transition to the nematic phase is approached. There are, however, also compounds showing a first-order smectic-A – nematic transition. First-order smectic-A – nematic transitions are also obtained in mixtures of a second-order smectic-A – nematic compound with a compound possessing a smectic-A – isotropic transition. A well studied example are binary mixtures of the two cyanobiphenyl compounds 8CB and 10CB. The binary phase diagram is shown in Figure 1.4. Precise adiabatic scanning measurements [18] demonstrate the existence of a tricritical point

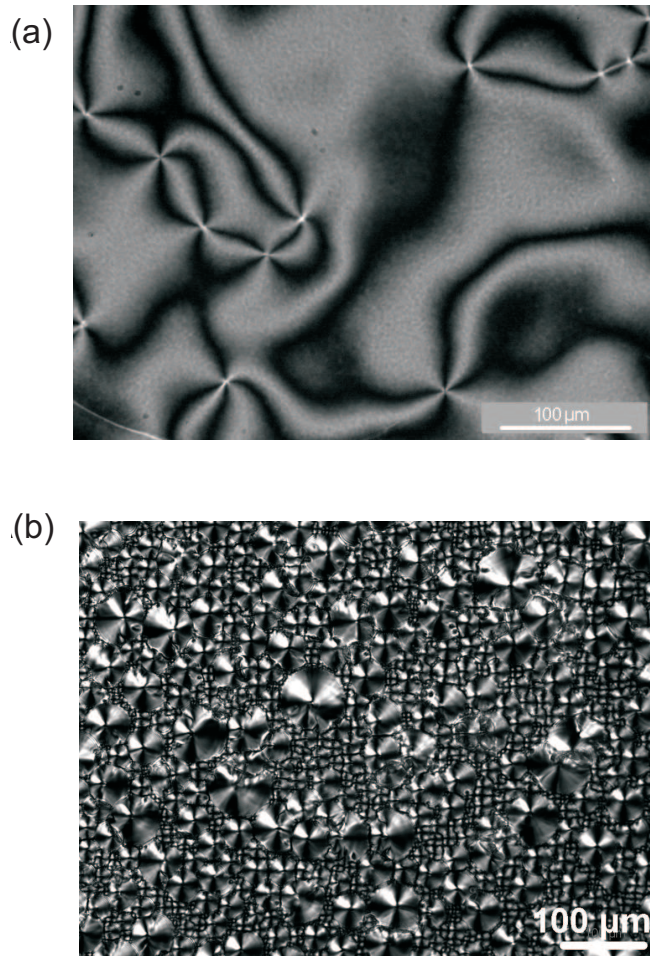


Figure 1.3: (a) Schlieren texture of the nematic phase and (b) focal conic texture with maltese crosses of the smectic-A phase.

in the smectic-A – nematic transition line, where the nature of the transition changes from second-order to first-order. The tricritical composition was reported for $x_{10CB} \approx 0.3$ (x_{10CB} is the mole fraction of 10CB in the sample), i. e., a second-order smectic-A – nematic transition is present for $x_{10CB} < 0.3$, while a first-order transition is detected for $x_{10CB} > 0.3$.

Unlike nematic and cholesteric phases, which both are extremely sensitive to weak external perturbations, smectic liquid crystals possess a relative stable layer structure, which make them progressively studied in the field of physics of detergents, membrane biophysics, and elastic and hydrodynamic studies. It should be noted that the higher rigidity of smectic phases leads to much shorter time constants compared to those of nematics: thermal excitation of smectic-A phases can provide a promising type of displays with intrinsic memory and speed.

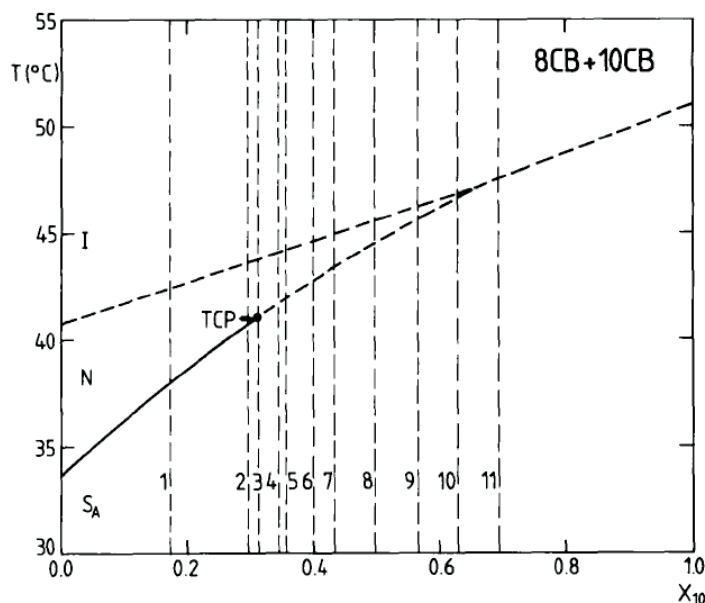


Figure 1.4: Binary phase diagram of 8CB/10CB mixtures. Solid and dashed lines are, respectively, second- and first-order transitions. TCP is the smectic-A – nematic tricritical point. Vertical dashed lines indicate the measured mixtures (from [18]).

A selective control of smectic textures can provide new types of memories addressable and readable optically and also displays compatible with video rates [19]. Moreover, new structures could be produced by distortions induced by external fields (electric fields, magnetic fields, or surfaces). The recent demonstration [20] of the use of surface-induced focal conic domains in smectic films on solid substrates for the positioning of microparticles highlights the increase of possible applications of smectic phases in the field of nanotechnology.

The rapid progress of applications of smectic liquid crystals also results in the need of a better understanding of the behaviour of smectic phases. In smectic liquid crystals, surface interactions play an important role in the formation of defect textures and structural domains. Therefore, my work is mainly attributed to the study of the behaviour of smectic phases on solid substrates.

1.3 Continuum Description of Liquid Crystals

There are various theoretical approaches to describe structures of liquid crystals and phase transitions between them [15]. Among these theories, elastic continuum theory is one of the basic theories, and used today. My study is based on this theory.

The foundations of the continuum model were developed in the late 1920s by Oseen [21] and Zöcher [22], who laid the basis of the static theory. After nearly thirty years, Frank reformulated Oseen's model and presented it as a theory of curvature elasticity [23]. Later, additions by Ericksen [24, 25] and Leslie [26, 27] completed the theory to the standard model which is now widely used for the description of many phenomena in nematic liquid crystals [15, 28, 29].

In continuum theory, the liquid crystal is treated as a continuous medium, entirely ignoring the molecular details. A macroscopic nematic sample is described by the director field $\mathbf{n}(\mathbf{r})$, which is subject to elastic distortions. In most cases, an arbitrary distortion can be described by a combination of three fundamental distortion types: splay, twist, and bend (Figure 1.5).

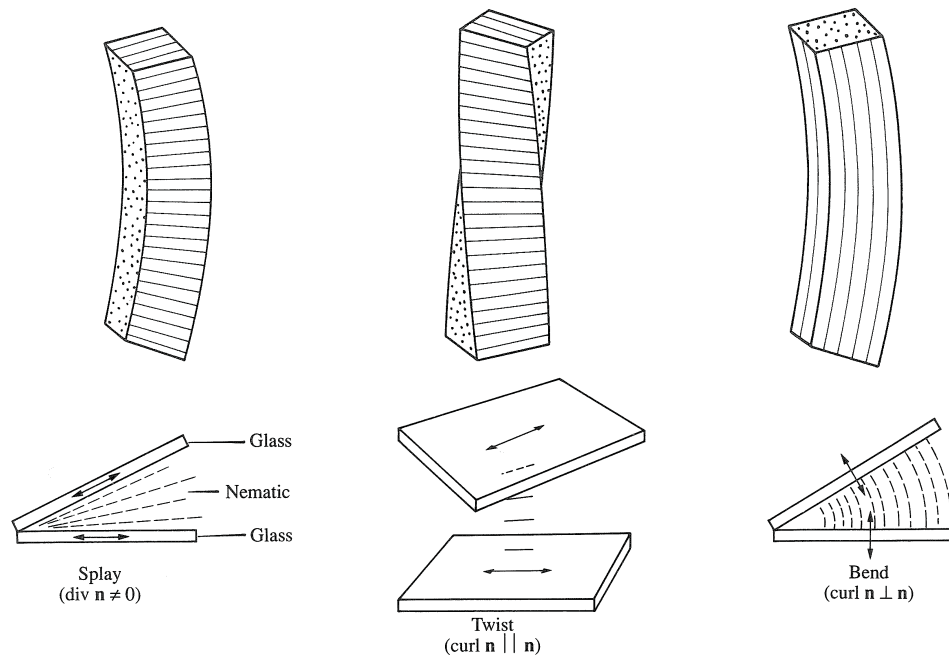


Figure 1.5: The scheme of three fundamental distortions in a nematic liquid crystal (cf. [15]).

The splay deformation corresponds to a divergence of $\mathbf{n}(\mathbf{r})$, i. e., $\text{div } \mathbf{n} \neq 0$. In a twist deformation, $\mathbf{n}(\mathbf{r})$ forms a helical structure with the helix axis being perpendicular to \mathbf{n} , resulting

in $\mathbf{n} \cdot \text{curl } \mathbf{n} \neq 0$. The bend deformation is characterized by a curl of $\mathbf{n}(\mathbf{r})$ perpendicular to \mathbf{n} , thus $\mathbf{n} \times \text{curl } \mathbf{n} \neq 0$. All three types of distortions cost a certain energy which is described by three elastic constants, K_1 , K_2 , and K_3 , associated with these distortions. The free energy f per unit volume of a deformed liquid crystal relative to the state of uniform orientation is then written as:

$$f = \frac{1}{2}K_1(\text{div } \mathbf{n})^2 + \frac{1}{2}K_2(\mathbf{n} \cdot \text{curl } \mathbf{n})^2 + \frac{1}{2}K_3(\mathbf{n} \times \text{curl } \mathbf{n})^2 \quad (1.1)$$

The magnitude of the elastic constants K_i is of the order of 10^{-11} J/m and the distortions are easily induced (and thus usually present in a macroscopic sample) by weak external influences. Equation 1.1 can be extended with terms describing the interactions with external electric and magnetic fields. However, for the present study the extension of the continuum description to smectic liquid crystals is of special importance.

In a smectic-*A* phase, the molecules are arranged in layers the thickness, of which is of the order of the length of the molecules. Looking at Figure 1.5, it is obvious that two of the three fundamental distortions, twist and bend, are not compatible with such a layer structure. In a twist deformation of the director field, a continuous layer structure is not possible (some chiral compounds show a so-called twist grain boundary — smectic-*A* (TGBA) phase, in which neighboring domains of plane parallel smectic layers are twisted with respect to each other, thereby forming a discontinuous helical structure [30]). In a bend deformation of $\mathbf{n}(\mathbf{r})$, the thickness of the smectic layers cannot be constant. Indeed, experiments show that the corresponding elastic constants K_2 and K_3 diverge at the transition from nematic to smectic-*A* [31].

A splay deformation of $\mathbf{n}(\mathbf{r})$ is compatible with the smectic layer since it requires only a bend deformation of the layer planes which is possible without changing the layer thickness. For instance, the layers could form a system of concentric shells around a singular point or concentric cylinders around a singular line. Thus, from the three terms in Equation 1.1, only the term associated with K_1 is of relevance in the smectic-*A* phase. On the other hand, in the smectic-*A* phase a new elastic distortion can occur which is not possible in the nematic phase, namely a compression or dilation of the smectic layers. Therefore, the continuum equation for the free energy density for the fundamental distortions in a smectic-*A* phase reads:

$$f = \frac{1}{2}K_1(\text{div } \mathbf{n})^2 + \frac{1}{2}B\left(\frac{d - d_0}{d_0}\right)^2 \quad (1.2)$$

Here, d_0 is the equilibrium value of the smectic layer thickness, d is the actual thickness, and B the elastic compression/dilation modulus. The magnitude of B can be experimentally

determined (see below) and is of the order of 10^7 J/m^3 indicating that, under normal conditions, $(d - d_0) \ll 1 \text{ \AA}$. For many purposes, the thickness of the smectic layers can be therefore considered to be practically constant. However, a major part of my thesis is concerned with results for which small deviations from the equilibrium thickness value d_0 are important. I therefore summarize here the known results on the compression/dilation modulus B .

The experimental behaviour of B has been studied especially near the second-order smectic- A – nematic transition; the studies are based either on light scattering measurements (yielding the ratio B/K_1) [32–36], or on mechanical techniques enabling the determination of absolute values of B [37–48]. When a smectic- A – nematic transition is approached from below, B decreases with increasing temperature to values close to zero at the transition. The behaviour can be described either by a simple power law, or by more complex models in which a small but finite value of B at the transition is assumed. The nature of the critical behaviour of B is still under investigation, recent studies indicate, that the observation of a finite value of B at the transition might result from a dynamical effect [41, 47]. Also for the exponent φ , which is used for a power-law description on approaching the smectic- A – nematic transition temperature T_{AN} according to

$$B = B_0(T_{AN} - T)^\varphi \quad (1.3)$$

the obtained values differ within a range from 0.3 to 0.6, the value is of importance to different theoretical models of the smectic- A – nematic transition, see [33, 37, 38]. However, all measurements show that B becomes small near a second-order transition to the nematic phase. An example for the decrease of B on approaching the smectic- A – nematic transition in the compound 8CB is shown in Figure 1.6.

The behaviour of B has been studied also at transitions between the smectic- A phase and different types of smectic- C phases [49–51]; B was found to show a pronounced minimum at the transition (Figure 1.7).

1.4 Anchoring of Liquid Crystals at Interfaces

The behaviour of liquid crystals at interfaces to solid substrates has received a wide attention [52]. One reason is definitely the application of liquid crystals in optical displays, where the liquid crystal is confined between two parallel transparent surfaces. Without certain boundary conditions, liquid crystals form differently ordered domains, which would destroy

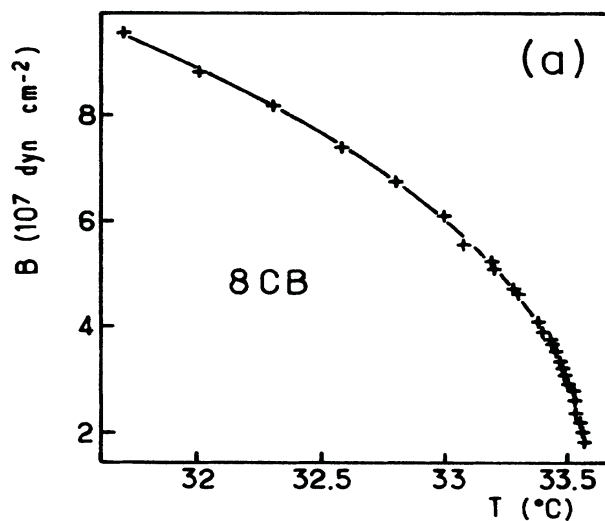


Figure 1.6: Temperature dependence of the layer compressional modulus B for 8CB near the transition to the nematic phase at $\approx 33.6^{\circ}\text{C}$ (from [37]).

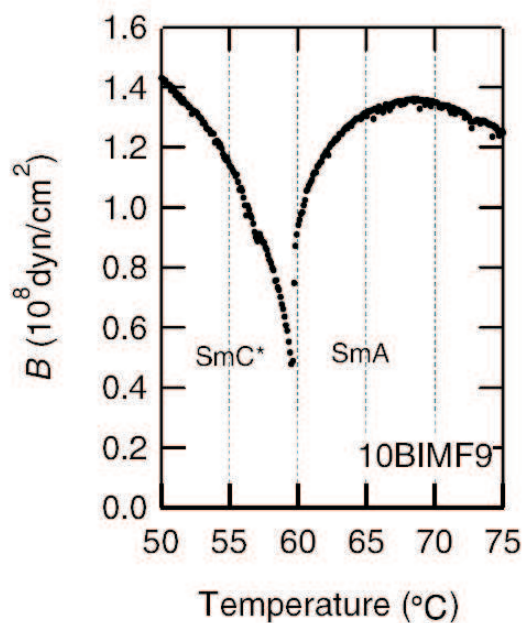


Figure 1.7: Temperature dependence of the layer compressional modulus B for the compound 10BIMF9 near a smectic-C – smectic-A transition (from [49]).

the functionality of liquid crystal displays. For the purpose to create a functional liquid crystal cell used as a display, a homogeneous texture of the liquid crystal is needed, i. e., the liquid crystal molecules have to be oriented in the same direction over a large surface area. And the solid surface is required to be designed to avoid the formation of domains. Generally, the surfaces (of, e. g., a glass cell) are covered with a stable organic layer like nylon, which promotes a certain orientation of molecules on the surface with their long axis parallel to the surface. Additionally, rubbing of the organic layer with a cloth causes the preferred orientation of all molecules to point into the same direction. Alternatively, surfaces treated with specific surfactants can impose a perpendicular orientation of the long axes of liquid crystal molecules on the surface. The ability of a surface to align the liquid crystal molecules in a specific way is called anchoring.

1.4.1 Anchoring on Solid Substrates

The phenomenon that a solid surface can impose a certain orientation to the molecules of a liquid crystal phase was discovered in 1913 by Mauguin [53], who reported that on cleaved surfaces of mica, the nematic liquid crystal oriented with its director \mathbf{n} parallel to the substrate and with an angle of 60° to the optical axis of the mica slide.

In general, \mathbf{n} close to the surface will take a fixed mean orientation, which is called the anchoring direction of the liquid crystal at the surface. Without any other external fields (electric or magnetic fields, flow, or another surface), this orientation is transferred to the bulk phase via the elastic forces of the director field which tend to produce a uniform orientation of \mathbf{n} in the whole sample, similar to epitaxy of solids on substrates. There may be several equivalent orientations of the director, and the anchoring is then designated as monostable, multistable, or degenerate, corresponding to one, a finite number bigger than one, or infinite orientations, respectively. Instead of the notation ‘degenerate’, often the term ‘random’ is used. With regard to the anchoring directions on the substrate, one can also classify the anchoring as planar, tilted or homeotropic, corresponding to a parallel, tilted or perpendicular orientation of \mathbf{n} to the plane of the substrate, respectively (cf. Figure 1.8).

The anchoring on a specific substrate can be simply characterized by the combination of the above terms. For example, on most crystalline substrates, the anchoring is monostable planar, except some examples with bistable or tristable planar anchoring (e. g., NaCl), and some examples with homeotropic anchoring (e. g., on LiNbO_3 , and Al_2O_3 [54]).

A large variety of anchoring states can be induced on modified glass substrates, treated by

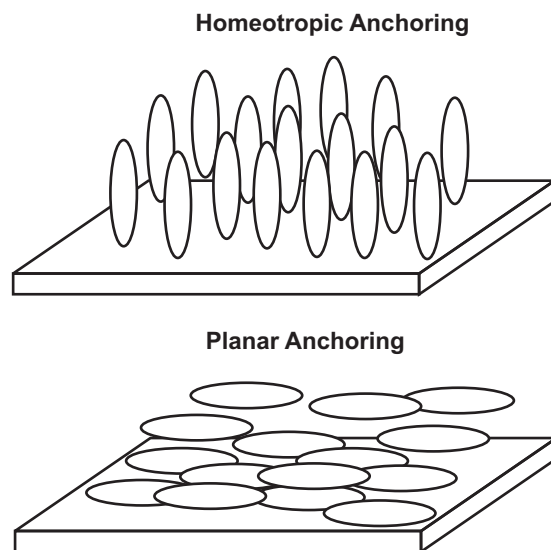


Figure 1.8: Schematic orientation of the liquid crystal molecules at an interface for homeotropic and planar anchoring.

mechanical rubbing or chemical deposition of a layer of surfactant, polymer, inorganic etc.. I shall not describe in detail these different anchorings induced by these surfaces, which have been reviewed by Cognard [55] and Jérôme [52]. On these substrates, the most commonly obtained anchoring states are the homeotropic, and the degenerate or monostable planar anchoring. Monostable tilted anchoring states are less present and multistable anchorings are seldom obtained.

For multistable or degenerate anchoring states, the selection of anchoring directions is generally made by the history of the sample. For instance, when the liquid crystal in the isotropic phase is placed in contact with a substrate which induces a degenerate planar anchoring, and then cooled down to the nematic phase in the presence of an external magnetic field, an anchoring direction parallel to the field will be obtained [56–58]. A selection can also be made when the nematic liquid crystal spreads onto the substrate [59–63]. The selected anchoring direction depends on the direction of spreading and, when the anchoring is tilted, on the dynamic contact angle [64, 65]. Moreover, once the selection has been made, the anchoring direction is not easily be changed on the substrate surface. Even in the case of the degenerate anchoring mentioned above, the orientation still remains without the external field, and is stable while heating up to several degrees above the nematic – isotropic temperature or applying a field in another direction [56–58]. This might result from a physisorption of the molecules onto the

substrate (which is confirmed by scanning tunnelling microscopy), or a chemisorption (even although there is no experimental evidence reported).

In my study, the anchoring obtained on mica is a planar monostable anchoring, but on MoS_2 , six possible planar anchoring directions are found. Bare silicon substrates exhibit random planar anchoring, as well as silicon substrates self-assembled with polyethyleneimine (PEI) or *n*-trimethoxysilylpropyl-*n,n,n*-trimethylammonium chloride (MAP). Silicon substrates self-assembled with octadecyldimethyl(3-trimethoxysilylpropyl)ammonium chloride (DMOAP) lead to a homeotropic anchoring.

An important point for my study is also the anchoring at liquid crystal/air interfaces, where most liquid crystals show a strong homeotropic anchoring.

1.4.2 Microscopic Anchoring Mechanisms at Solid Substrates.

The mechanisms responsible for the creation of anchoring on solid substrates are not well known. Ordered monolayers of liquid crystal molecules on crystalline substrates (such as graphite [66–70] and MoS_2 [71, 72]) have been observed by scanning tunnelling microscopy, and the azimuthal orientation of the liquid crystals must result from the molecule/substrate interactions. On rubbed polymer films, in which the polymer chains orient along the direction of rubbing, it has been found that also the liquid crystal molecules orient parallel to the rubbing direction [73]. This indicates that the orientation of the molecules arise from the interaction with the polymer chains which induces them to align parallel to the chains. Further evidence for the existence of such an interaction is the fact that an isotropic polymer film can be made anisotropic by placing a homogeneously aligned nematic liquid crystal on it [74].

For tilted anchoring states, the value of the tilt angle between the anchoring direction and the surface normal might result from a polar ordering, i. e., the way of how polar molecules like cyanobiphenyls arrange themselves with their polar groups facing to or against the substrate. Such polar order is found in the 8CB monolayers on water [75], clean glass, glass coated with silane surfactants DMOAP and MAP [76], and glass coated with a polyimide film (rubbed or unrubbed) [77, 78]. The existence of polar substrate/molecule interactions breaks the symmetry of the non-polar dimer structure in the cyanobiphenyl bulk phase. In the case of glass coated with octadecyltrichlorosilane (OTS), which gives an excellent homeotropic alignment of liquid crystals in the nematic and smectic phases, the aliphatic chains of 8CB are in contact with the substrate, followed by a non-polar ‘dimers’ structure of 8CB, which is similar to the situation occurring at the interface with a gas phase [79]. However, on a

DMOAP coated substrate, the adsorption of a polar layer of 8CB is allowed [80], because the large head group and loose structure of DMOAP permit the access of the polar cyano group of 8CB to surface polar sites. The tilt of the hard biphenyl core of the 8CB molecules in polar monolayers is found to be approximately 70° and does not seem to depend on the surface coverage or on temperature. The presence of this tilt can be explained by the fact that it reduces the dipole-dipole interaction between the polar heads of 8CB molecules [75].

On rubbed substrates, e. g., polyimide films rubbed by velvet in one direction, the cyanobiphenyl molecules tend to align along the rubbing direction, with more molecules pointing with their tails in the rubbing direction than in the opposite direction. Also in this polar layer the molecules are tilted, similar to the structure of isolated monolayers. It should be noted that the anisotropy of the interfacial layer remains even at 20°C above the isotropic – nematic transition temperature. In contrast, rubbing of bare glass or MAP-coated glass does not distort the isotropic azimuthal distribution of the anchoring direction [77, 78].

1.5 Focal Conic Domains in Smectic Liquid Crystals

1.5.1 Defect Structures in Smectic Phases

Among the three types of elastic distortions of the director field $\mathbf{n}(\mathbf{r})$ — splay, twist, and bend, only the splay distortion survives in smectic phases, because the incompressibility of the smectic layer structure suppresses the twist and bend distortions. In smectic-A liquid crystals, a fairly large energy is necessary to change the layer spacing which can be considered as practically constant. Deformations of the smectic layer structure therefore transfer the smectic planes into parallel surfaces with the same center of curvature. The resulting arrangement of the smectic layers is a so-called focal conic domain; its construction is shown in Figure 1.9: In (a) the smectic layers form concentric cylinders around one straight singular line. In (b), the straight singular line has been looped into a circle which creates another straight singular line running through the center of the circle. The smectic layers form a system of concentric tori. In (c), the general case of this structure is shown, in which the circular and the straight singular line of (b) has become an ellipse and a hyperbola; ellipse and hyperbola run through each other focal point. The smectic layers form a system of parallel Dupin cylinders.

The presence of focal conic domains leads to the typical textures of smectic phases in the polarizing microscope. Their detailed study has already led, by Friedel in 1922, to the conclusion that the smectic-A phase must possess a layered structure [14]. Comprehensive

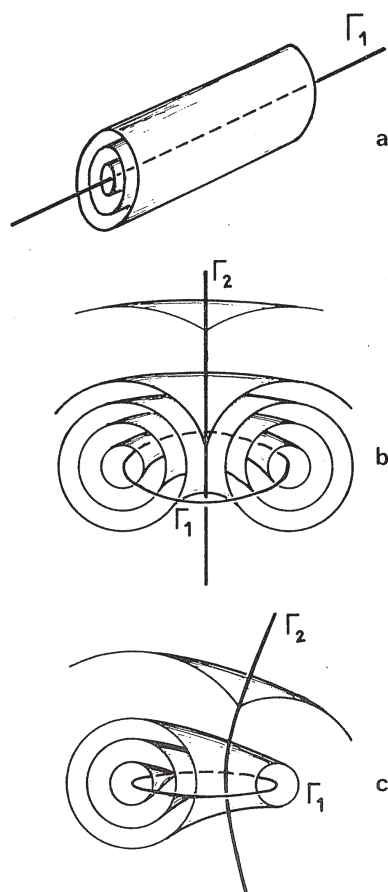


Figure 1.9: Schematic construction of a focal conic domain: (a) confocal domains degenerated into a cylinder. (b) Toric focal conic domain, singular lines are a circle and a straight line. (c) The general case with an ellipse and a hyperbola as singular lines, the layers form parallel Dupin cyclides (cf. [81]).

studies of focal conic domains in bulk smectic phases started again in 1972 with a series of papers by Bouligand [82]. The properties of focal conic domains in the bulk smectic-A phase are now well understood (see review [83]). Recently, the interest in these structures has been renewed with respect to the concept of using liquid crystal structures as matrices or templates for new self-organizing systems. In this context, the targeted generation, the properties, and the control of focal conic domains in thin films and in confined environments like microchannels are important issues.

1.5.2 Focal Conic Domains in Thin Films and Microchannels

Focal conic domains are formed in response of the smectic liquid crystal to a frustration between an external influence inducing a bent configuration and the incompressibility of the smectic layers. For instance, in a cell with homeotropic anchoring at both interfaces, the smectic layers usually form a simple stack with the layer planes aligned parallel to the interfaces; if an electric field of sufficient strength is applied perpendicular to the layers and the liquid crystal material possesses a negative dielectric anisotropy, the formation of focal conic domains is induced [84]. Another method is the preparation of a film with antagonistic anchoring conditions at its interfaces. If one interface exhibits a homeotropic anchoring condition and the other interface a degenerate planar anchoring, the smectic layers will form focal conic domains. Actually, the generated structures are half-domains since one of the singular lines (the ellipse or circle) is located at one interface of the film, and the smectic phase extends only in one direction. Figure 1.10 shows a schematic drawing of the arrangement of the smectic layers.

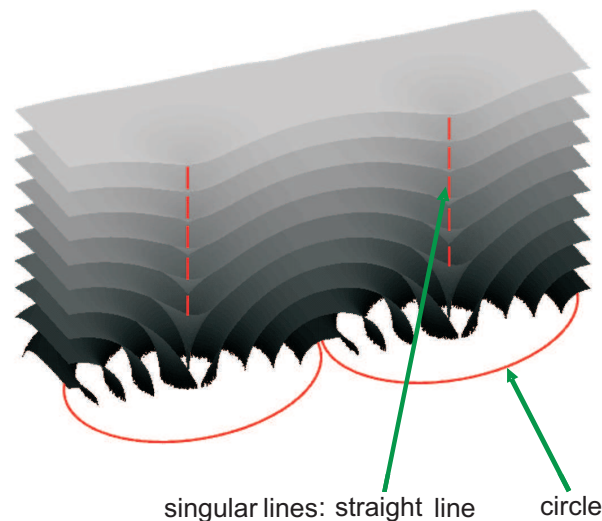


Figure 1.10: Schematic drawing of two neighboring focal conic domains in a film with homeotropic (top interface) and degenerate planar (bottom interface) anchoring conditions. The smectic layers are wrapped around two singular lines (in this drawing, a straight line and a circle).

A corresponding experimental system has been studied first by Fournier et al. [85] who investigated smectic-A films floating on their isotropic melt (the liquid crystal compounds

possessed a smectic-*A* – isotropic phase transition). The air interface of the film provided the homeotropic anchoring, and at the smectic-*A*/isotropic interface a degenerate planar anchoring was observed. Fournier et al. obtained a two-dimensional hexagonal lattice of focal conic domains and provided a quantitative model of the energy of focal domains in such films. Since this model is used in the present study to analyze my results, I describe it below (Section 1.5.3) in more detail.

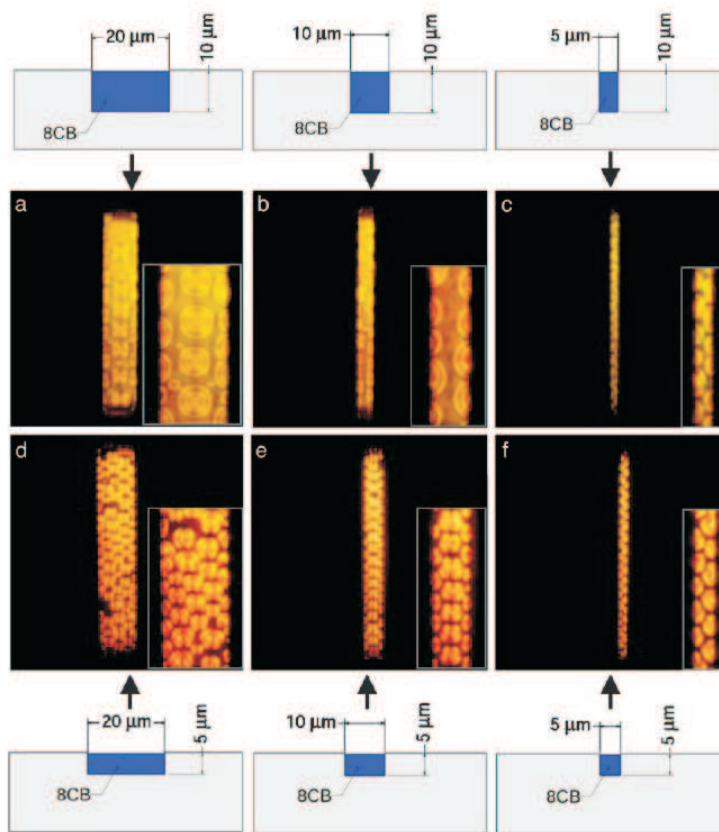


Figure 1.11: Polarized light microscopy images of ordered focal conic domains of smectic 8CB in surface-modified microchannels (Inset images are magnified $\times 2$), with corresponding schematic drawings shown above and below the images. From left to right, the widths of the channels are 20, 10, and 5 μm . In a-c, the channel depth is 10 μm . In d-f, the depth is 5 μm . (Magnification: $\times 400$, from [86].)

On solid substrates, first studies were carried out in open microchannels with polyethyleneimine-coated walls [86, 87] or in microchannels in PDMS substrates [88]. These studies are concerned with the effects of geometric confinement on focal conic domains. It was shown that

regular arrays of focal conic domains can be obtained. The details of the generated structures depend on the width and depth of the microchannels and the anchoring conditions at the channel walls. Figure 1.11 shows an example of regular patterns of focal conic domains formed in microchannels with different dimensions. The geometry of surface-modified microchannels confines the size and spatial arrangement of focal conic domains. Two-dimensional ordered patterns of nearly uniform sized units can be obtained by controlling the width and the depth of the channels. During the course of my study, more papers [20, 89] appeared extending the concept of controlling the arrangement of focal conic domains by microchannels. In [20], it was also demonstrated that focal conic domains can be used as a matrix for the positioning of microbeads.

A different concept of confinement and arrangement control of focal conic domains was used by Bramble et al. [90], who prepared on a gold-coated substrate with different self-assembled monolayers. They used two organothiols leading either to homeotropic or degenerate planar anchoring on the substrate. When a smectic film is prepared on such a substrate, the focal conic domains form only in (and are confined to) the planar anchoring areas. The concept of creating anchoring patterns on a solid substrate is also a major topic of my thesis and is discussed in Chapter 4.

Focal conic domains in films on homogeneous flat substrates without confinement effects have been studied by Designolle et al. [91], who have shown that AFM microscopy measurements of the shape of the film/air interface can be used to characterize the underlying focal conic domains and their behaviour at smectic-A – nematic and smectic-A – isotropic phase transitions.

Smectic films have also been studied on the surface of freshly cleaved MoS₂ crystals [92–95]. This is a planar anchoring substrate possessing six preferred in-plane aligning directions, $\pm 17.5^\circ \pm 0.4$ (modulo 60°) away from the MoS₂ [100] direction, confirmed by X-ray grazing incidence diffraction. Instead of circular focal conic domains, linear structures are obtained as shown in Figure 1.12. The circular or elliptical singular lines of the focal conic domains are replaced in these structures by a straight singular line running in the substrate plane perpendicular to the preferred in-plane anchoring direction. The studies were concerned with very thin films in which the curved smectic layer structure around the linear singular line was used as a model system for X-ray structural studies of smectic defect cores. In Chapter 5, I present preliminary results concerning thicker liquid crystal films on MoS₂ and mica substrates which indicate that the hemicylinder structure observed in thin films is replaced by a more complex structure possibly consisting of fragmented focal conic domains.

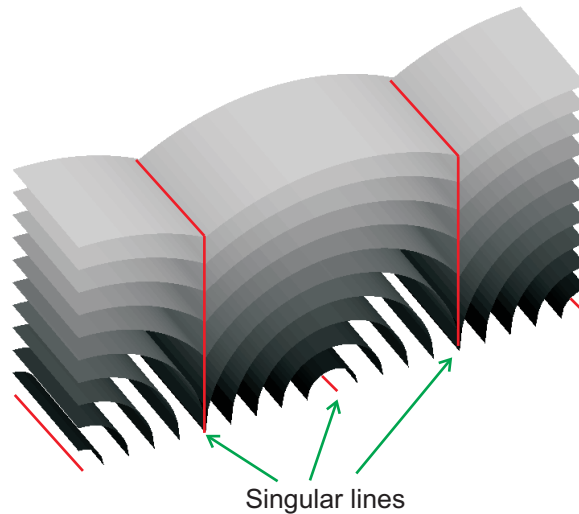


Figure 1.12: Schematic drawing of the hemicylinder arrangement of the smectic layers on a planar anchoring substrate with a preferred in-plane aligning direction.

1.5.3 Model for The Energy of A Focal Conic Domain in Thin Films

To analyze my results on focal conic domains, I use the model created by Fournier et al. [85]. A cross section of a focal conic domain between the two antagonistic interfaces, air and solid substrate, is shown in Figure 1.13. The singular lines (in general an ellipse and a hyperbola) are assumed to adopt the shape of a circle and a straight line. H stands for the thickness of the smectic film, r for the radius of the domain base, and h for the depth of the depression induced by the focal conic domain in the air interface.

Fournier et al. compared the structure shown in Figure 1.13 with the undistorted smectic- A structure, which is a simple stack of plane parallel layers. There are three energy contributions by which the focal conic domain differs from the undistorted case: the energy F_1 related to the curvature of the smectic layers and the singular lines which are not present in the undistorted case, the surface energy F_2 of the random planar anchoring on the substrate (in the undistorted case, the anchoring is homeotropic), and the energy F_3 related to the increased area of the curved smectic- A /air interface (in the undistorted case, this interface is completely flat).

Concerning contribution F_1 , the curvature energy F_{curv} of a toric (circular) focal conic

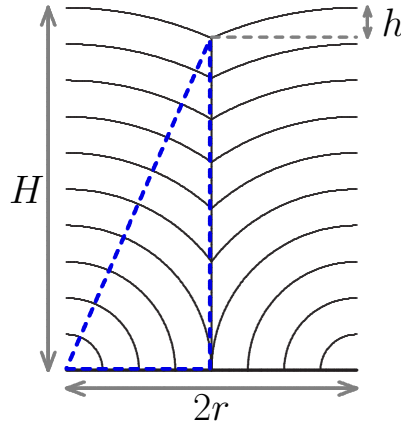


Figure 1.13: Schematic cross section through a toric focal conic domains with diameter $2r$ in a smectic film of thickness H . The bend deformation of the smectic layers leads to a depression in the film/air interface with depth h . If the cross sections of the layer planes form concentric circles, the value of h is easily calculated according to the Pythagorean theorem (triangle indicated by the dashed lines).

domain in bulk is given by [96]:

$$F_{curv} = 2\pi^2 K_1 r \left(\ln \frac{2r}{r_c} - 2 \right) \quad (1.4)$$

with r denoting the domain radius and K_1 the splay elastic constant; r_c is a core radius and of the order of one layer thickness (a few nm). Fournier et al. approximate $\ln(2r/r_c)$ by a constant mean value so that F_{curv} becomes simply proportional to r . The core energy of the circular singular line is also assumed to be proportional to r while the core energy of the straight singular line is assumed to be proportional to the film thickness H . Thus, Fournier et al. wrote F_1 as $F_1 \approx 2\pi\alpha K_1 r + 2\pi\beta K_1 H$, where α and β are dimensionless unknown constants.

The second contribution F_2 , related to the different anchoring conditions, is given by $F_2 = \pi r^2 \Delta\sigma_{sub}$. πr^2 is the area of the domain base on the substrate and $\Delta\sigma_{sub}$ the surface energy difference between homeotropic and planar anchoring.

For the third contribution F_3 , the area A of the surface of the depression above the focal conic domain must be taken into account. This area is given by

$$A = 2\pi H^2 \left(\rho \arcsin \rho + \sqrt{1 - \rho^2} - 1 \right) \quad (1.5)$$

with $\rho = r/H$. A Taylor expansion to the fourth power around $\rho = 0$ gives $A \approx \pi r^2 + \pi r^4/(12H^2)$,

the latter summand representing the additional area caused by the curvature of the surface above the focal conic domain. F_3 is thus given as $F_3 \approx \pi r^4 \sigma_{air} / (12H^2)$ with σ_{air} denoting the smectic-A/air surface tension. Thus, Fournier et al. obtained for the energy F of a focal conic domain:

$$F = 2\pi\alpha K_1 r + 2\pi\beta K_1 H - \pi r^2 \Delta\sigma_{sub} + \frac{\pi r^4 \sigma_{air}}{12H^2} \quad (1.6)$$

Equation 1.6 predicts a minimum of F with respect to r , provided that $r > r_c = 3\alpha K / (2\Delta\sigma_{sub})$, and a nearly linear relationship between film thickness H and radius r is obtained:

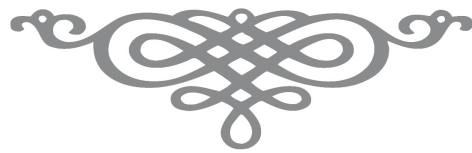
$$H = \left[\frac{\sigma_{air} r^3}{6\Delta\sigma_{sub} \left(r - \frac{\alpha K}{\Delta\sigma_{sub}} \right)} \right]^{1/2} \quad (1.7)$$

Thus, the diameter $2r$ of the focal conic domains is expected to increase with the thickness H of the smectic film. For a given smectic film, σ_{air} and αK are intrinsic properties. The relation between r and H is then determined by $\Delta\sigma_{sub}$ which can be considered as a kind of anchoring strength. Experimental studies concerning this topic and the relation between the thickness the smectic film and the diameter of the focal conic domains are presented in Chapter 3.

Liquid crystals have been a subject of interest since many years, due to their unusual physical properties by virtue of their intermediate position between isotropic liquids and crystalline solids. Although liquid crystal properties are not yet fully understood in all aspects, these materials are widely applied in a number of fields. The aim of my thesis is a fundamental study of focal conic domains in films on different types of solid substrates. After describing my experimental methods, I will discuss in the following chapters the morphology and the behaviour at phase transitions of focal conic domains on homogenous substrates with a degenerate planar anchoring (Chapter 3), on patterned substrates possessing regions with planar and homeotropic anchoring (Chapter 4), and on crystalline substrates with a mono- or multi-stable anchoring (Chapter 5).

So far, liquid crystal research is still powered in liquid crystal display industry and fundamental scientific interest. Liquid crystals represent a great system to study phase transitions, correlations in the liquids or interaction of the liquid with the surface. The results, findings and theoretical treatments of liquid crystal research can be widely used in the research of other

partially ordered complex systems, like polymers or biological materials.



Chapter 2

Materials, Methods and Experimental Techniques

“Progress is the activity of today and the assurance of tomorrow.”

Ralph Waldo Emerson (1803 – 1882)

This chapter will introduce the main experiments in my work, including materials, preparation methods and characterization techniques. Atomic Force Microscope (AFM), as an important measurement technique in my work, will be discussed in details in this chapter, including its physics background and its operation.

2.1 Liquid Crystal Materials

The liquid crystals, mainly used in my experiments, are 4'-alkyl-4-cyanobiphenyls (n CBs), which were purchased from Syntho Chemicals (Germany). n CB molecules and their derivatives are standardly used to study anchoring and alignment of liquid crystals on various substrates. This is because they are stable, widely available, well characterized, and constitute many commercial mixtures used in display devices.

Between the solid phase and the isotropic liquid phase, the members of n CBs with $n = 5-7$ show a nematic phase, and those with $n = 8$ and 9 exhibit nematic and smectic-A phase, while for $n > 10$ there appears only the smectic-A phase. The compounds and their phase transition temperatures are shown in the Table 2.1.

Name of liquid crystals	Phase Transition Temperature (°C)				
	Solid → Sm-A	Solid → Ne	Sm-A → Ne	Sm-A → Iso	Ne → Iso
6CB	–	14.8	–	–	29
8CB	21.5	–	33.4	–	40.5
9CB	40	–	47	–	49
10CB	44	–	–	50.5	–
12CB	48	–	–	58.5	–

Table 2.1: Liquid crystals used in the experiments and their phase transition temperature (experimental data).

In some experiments, mixtures of *n*CBs were prepared. Compared with the component liquid crystals, the phase transition of the mixtures changes, and transition temperatures shift according to the ratio of mixture.

Table 2.2 lists an example of the phase transition temperatures of the mixture of 6CB and 8CB. As the content of 6CB increasing in the mixtures, both phase transition temperatures of smectic-A → nematic and nematic → isotropic decrease gradually.

The phase transitions of mixtures of 10CB and 8CB have been discussed in Chapter 1, Section 1.3, and I will discuss it further in Chapter 3, Section 3.2.2.

Mol Ratio of 6CB and 8CB Mixture	Phase Transition Temperature (°C)	
	Sm-A → Ne	Ne → Iso
1:9	30.3	40.3
1:4.5	27	39.3
1:3.6	25	38.3
1:2.7	22	38

Table 2.2: Phase transition of the mixtures of 6CB and 8CB and their phase transition temperatures (experimental data).

Besides above alkyl-cyanobiphenyl liquid crystals, the liquid crystals with smectic-*C* phase were used in my experiments, which are listed in Table 2.3, and their molecular formulae are illustrated in Figure 2.1.

All materials are used without further purified.

Name of liquid crystals	Phase Transition Temperature (°C)				
	Sm-C → Sm-A	Sm-C → Ne	Sm-A → Ne	Sm-A → Iso	Ne → Iso
Pyp9O7	52	–	–	73.2	–
Pyp8O8	58.2	–	65	–	71
A7	74.5	–	–	82.5	–
C9	53	–	–	62.5	–
C7	55.5	–	–	62.7	–
$\bar{8}.S.5$	55	–	62	–	85

Table 2.3: Liquid crystals with smectic-C phase, and their phase transition temperature (experimental data).

2.2 Preparation Methods

2.2.1 Substrate Preparation

Homogenous Substrate

In my work, liquid crystal droplets or films on solid substrates were studied. With respect to the generation of focal conic domains or other defect structures in the liquid crystal, the most important property of the substrate is the anchoring condition which is imposed on the liquid crystal by the substrate. On substrates with random planar anchoring, toric focal domains are obtained, while substrates with unidirectional or multidirectional planar anchoring lead to linear defect structures.

In my experiments, the homogenous substrates, e. g., silicon wafers, modified silicon wafers, mica, and MoS₂, were used as substrates.

Substrates with random planer anchoring

Either the bare surface or the coated silicon surface, were served as substrates with random anchoring. In both case, the wafers were initially cleaned with ‘Piranha solution’.

Two kinds of Piranha solution were used. One is the acid Piranha solution, prepared by mixing three volumes of concentrated H₂SO₄ (98%, provided by VWR International, Germany) and one volume 30% aqueous solution of H₂O₂ (provided by Merck, Germany). The

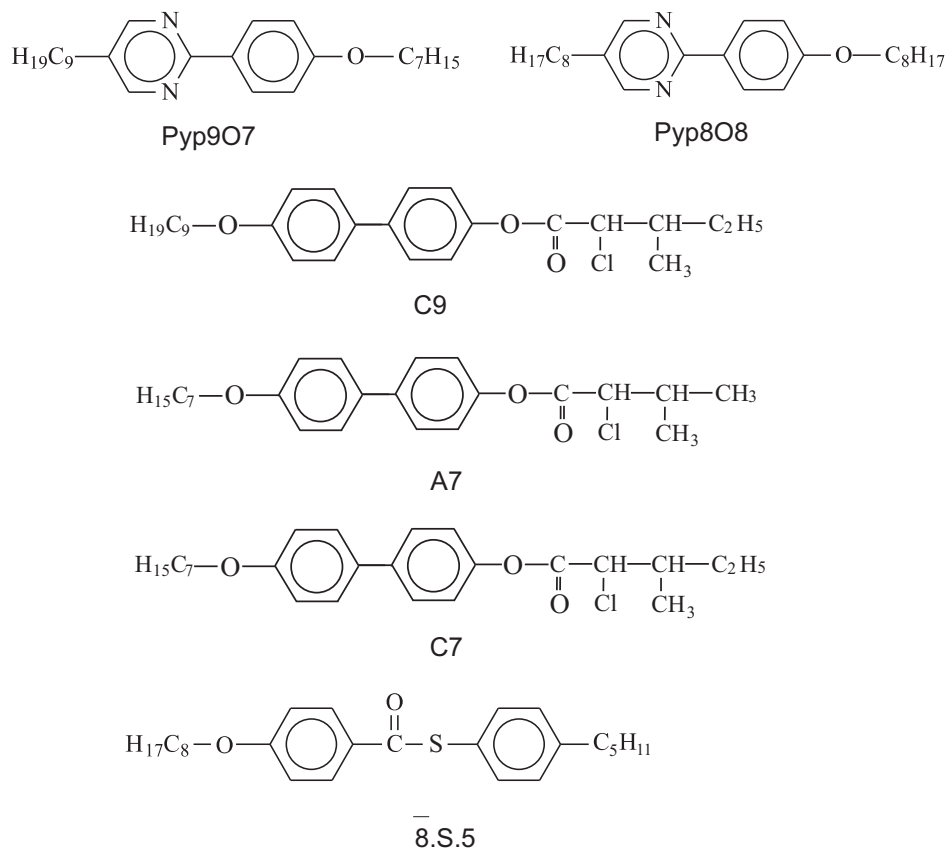


Figure 2.1: Molecular formulae of liquid crystals used in the experiments.

other is the base Piranha solution, obtained by mixing 3:1 of ammoniac solution (25%, from Merck, Germany) and 30% aqueous solution of H_2O_2 .

Silicon wafers were cleaned as the following procedures. First, silicon wafers were rinsed in acetone and sonicated for 15 minutes, followed by sonication in distilled water for 15 minutes. After dried by a nitrogen flow, these wafers were put in a fresh Piranha solution and kept at 80°C for 30 minutes. Next, the wafers were thoroughly washed with Millipore water. At last, store the wafers in the distilled water. Before used, the wafer was dried with a nitrogen flow.

To obtain the hydrophilic surface, the wafers were only treated by the acid Piranha solution. To make the surface negatively polarized, the base Piranha solution were also used after cleaning the wafers with the acid Piranha solution.

A bare silicon surface, cleaned with Piranha solutions, imposes a random planar anchoring on liquid crystal compounds. However, it still induces to a larger contact angle of the droplet

of the liquid crystals. To reduce the contact angle and modify the strength of the planar anchoring, the bare silicon surface was coated with organic layers for some experiments. Two types of coating, a cationic polymer and alkoxy silanes, were employed.

A layer of a cationic polymer, polyethyleneimine (PEI) (from sigma-Aldrich Chemie GmbH, Germany), was self-assembled on a clean silicon wafer. To enhance the absorption of PEI, the substrate was firstly treated by the base Piranha solution. And then immerse the treated wafer in a 2 g/l PEI aqueous solution for 30-60 minutes, followed by shortly washing with the Millipore water, and drying under a nitrogen flow.

Two kinds of alkoxy silanes were also chemisorbed on silicon substrates, which are octadecyldimethyl(3-trimethoxysilylpropyl)ammonium chloride ($C_{26}H_{58}ClNO_3Si$, DMOAP, 60% methanol solution) and n-trimethoxysilylpropyl-n,n,n-trimethylammonium chloride ($C_9H_{24}ClNO_3Si$, MAP, 50% methanol solution) (purchased from ABCR GmbH & Co. KG, Germany). To prepare the alkoxy silane substrate, the clean silicon substrate was dipped in the 0.1% (by volume, the fraction $x \approx 3 \times 10^{-3}$ mol/l) aqueous MAP or DMOAP solution for 5 minutes, and then remove extra silane with Millipore water. After dried with a nitrogen flow, the substrate was then thermally cured at 110°C for 1 hour.

These surfaces are known to yield different bulk liquid crystal alignments. DMOAP-coated substrates lead to homeotropic alignment, while MAP-coated substrates give planar alignment. To obtain different substrates with different planar anchoring strength, a series of proportions of MAP and DMOAP mixtures were self-assembled on the silicon substrates. The mixtures were prepared by diluting a certain proportion of MAP and DMOAP mixture with the Millipore water till the concentrate in total is up to 0.1% (by volume). The details of the anchoring strength of the MAP and DMOAP mixture will be discussed in Chapter 3.

Substrates with uni-or multidirectional planar anchoring

The surface of inorganic crystals served as substrates possessing planar anchoring in conjunction with one or several preferred in-plane directions for the orientation of director. Two types of inorganic crystals were used: mica and MoS_2 crystals. Both compounds possess a layered crystal structure which allows to remove the thin crystal layers easily, so as to obtain a 'fresh' and atomic-level flat surface. To prepare the substrates, a piece of mica or MoS_2 is fixed on a rigid carrier (e. g., a metal disc used for AFM measurements) and a thin crystal layer is removed with a razor blade or a piece of scotch tape. The liquid crystal film is then prepared directly on the surface of the freshly cleaved crystalline substrate.

Patterned Substrates

To control the arrangement of focal conic domains and study confinement effects, I prepared substrates, which possess an anchoring pattern, i. e., the surface of these substrates exhibits in some areas random planar anchoring and in other areas homeotropic anchoring. On such substrates, focal conic domains form only in the planar anchoring areas. The anchoring pattern is generated by the following method: a silicon wafer with a cleaned bare surface, possessing random planar anchoring, was covered by an appropriate mask, through which a thin gold film was evaporated onto the silicon wafer. While a bare gold surface imposes homeotropic anchoring on many liquid crystal compounds, planar anchoring exists only in the masked areas (uncoated, bare silicon areas).

Two types of masks were used, one consists of electron microscopy copper grids (BALTEC, Germany), and the other is a monolayer of polystyrene microbeads (Polysciences Europe).

The gold film was thermally evaporated onto the silicon substrate with a mask, using an Edwards Auto 306 coating system. The thickness of the gold layer on the substrates, determined by AFM measurements, was typically between 40 and 60 nm. With the first type of mask, copper grids, we generated line-, square-, or hexagon-like patterns, in which gold coated areas are separated by 10 to 20 μm wide stripes of uncoated regions (as shown in Figure 2.2).

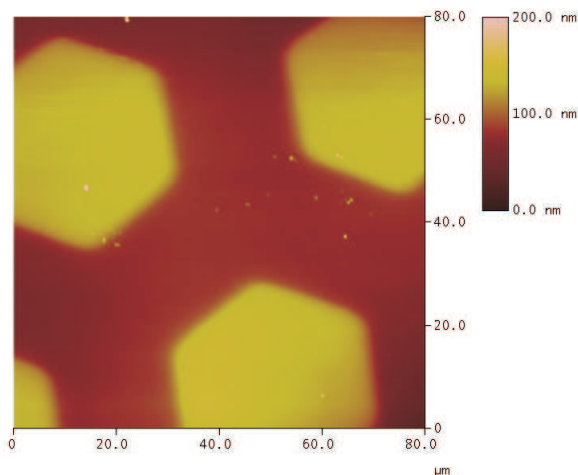


Figure 2.2: AFM image of gold patterned silicon substrate masked by copper grid.

As the second type of mask, we employed monolayers of polystyrene microbeads. The use

of colloid monolayers as versatile lithographic masks has been well demonstrated in [97, 98]. First, a 1×1 cm clean silicon substrate was placed on a glass slide, which was tilted with an angle of $2-3^\circ$. Second, $15-20 \mu\text{l}$ of diluted aqueous colloidal suspension of microbeads (1.2-1.5% by weight) was dropped and completely spread on it. Then cover this system with a Petri dish and keep it at 4°C for 2 or 3 days, so that the solution evaporated slowly, until the microbeads suspension solution was totally dry and formed a monolayer on the substrate.

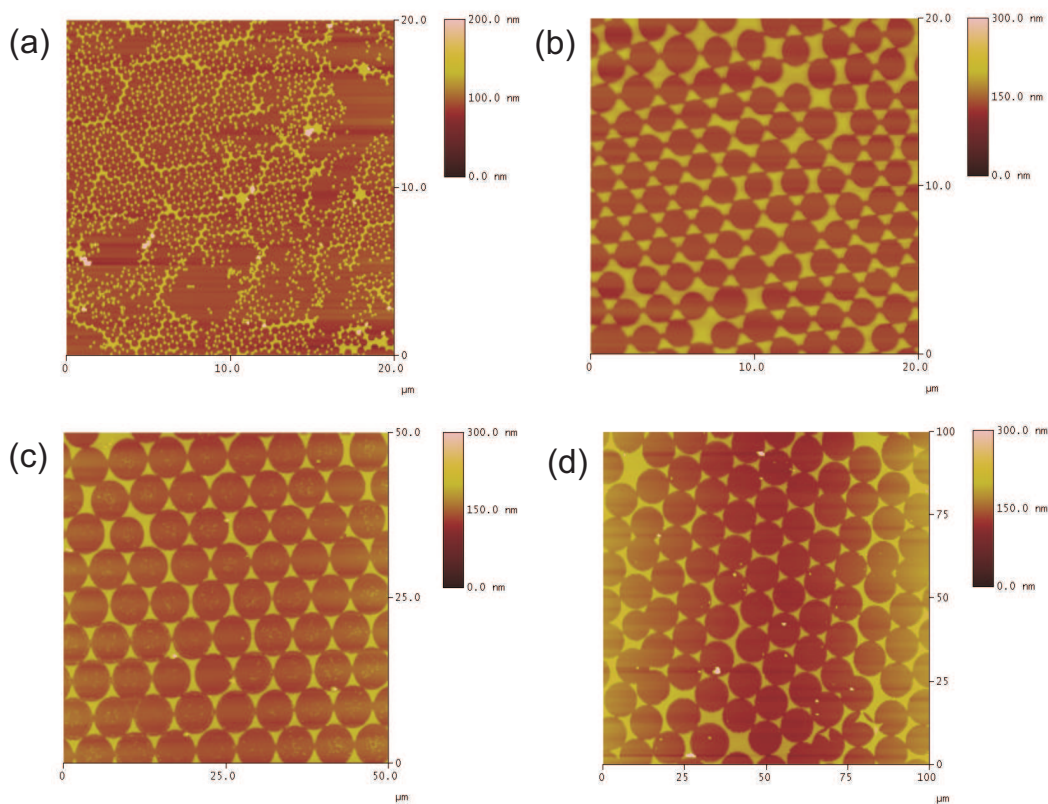


Figure 2.3: AFM images of the gold patterned silicon substrate masked by different size of microbeads. The size of the microbeads used in experiments is (a) 0.5 , (b) 2 , (c) 6 , and (d) $10 \mu\text{m}$, respectively.

After thermally coating the substrate with gold, the microbead monolayer was removed by slowly immersing the substrate into a water reservoir. In this treatment, the microbeads lost the contact with the substrate surface and floated at the water surface, leaving a hexagonal pattern of uncoated circular areas on the substrate [99]. Figure 2.3 shows the gold patterned silicon substrate masked by different size of microbeads. The dimension of these areas is determined by the diameter of the microbeads. We used colloidal suspensions of four differently sized

polystyrene beads with diameters of 0.5, 2, 6, and 10 μm (the further results will be discussed in Chapter 4).

2.2.2 Sample Preparation

In most experiments, liquid crystal films on the substrates were produced by placing a free droplet of liquid crystals on the substrate under optical microscope, and subsequently heating to the temperature range of the nematic phase or isotropic, according to the liquid crystals. In the nematic or isotropic phase, the droplets spread on the surface and reach a quasistatic shape after a few minutes (the nematic phase of *n*CB compounds is known wet silicon substrates completely, but the corresponding time interval is of the order of a few days). And then the samples were slowly cooled back into the smectic phase with a rate 0.1°C/min. On further cooling (within the smectic phase), the appearance of these samples (the location and diameter of the defects and the shape of the droplets) does not change, and the sample can be investigated by AFM for a long time (at least 24 hours).

Liquid crystal films obtained in my experiments are in fact flat droplets, the thickness of which increases from the edge to the center. Table 2.4 gives some examples of contact angles of 8CB and 10CB on different kinds of substrates.

If focal conic microscopy measurements are intended, a small amount ($\sim 0.01\%$ by weight) of the dye *n,n'*-bis(2,5-di-*tert*-butylphenyl)-3,4,9,10-perylenedicarboximide (BTBP) (purchased from Sigma) was doped into liquid crystals [100], followed by stirring for 2-4 hours at its isotropic temperature, in order to mix completely.

The different ratios of mixtures of liquid crystals, used for some experiments, were also stirred for > 1 hour at its isotropic temperature.

Name of Liquid Crystals	Contact Angle on Different Substrates °		
	Bare Silicon	PEI self-assembled Silicon	MAP self-assembled Silicon
8CB	12	8	2.8
10CB	15.3	2.6	6.3

Table 2.4: Contact angles of 8CB and 10CB on bare silicon, PEI and MAP self-assembled silicon substrates.

2.3 Characterization Techniques

Most of my work consists of topographical studies of focal conic domains at the air/liquid crystal interface, performed with AFM. Other devices, e. g., optical microscope, fluorescence confocal microscope, are introduced as complement.

Here is an example, the local thickness of the liquid crystal film on the substrate was determined by two methods: in thin regions near the edge of the film, the thickness was determined from AFM, by measuring the difference of z value between the bare substrate and the measured point area. In thicker regions, beyond the AFM measuring scale, the thickness was determined using fluorescence confocal microscopy, the resolution of which in z direction is 200 nm.

2.3.1 Optical Microscopy

A Leica DM4000C (Leica Microsystems) (shown in Figure 2.4) was used in my experiment. This optical microscope provides all basic transmitted-light and reflected light contrasting methods (bright/dark field, phase, polarization contrast).

A TMS 94 temperature controllers and THMSG600 heater stage (Linkam Scientific Instruments Ltd.) were combined with the optical microscope to control the temperature of the sample. The controlled heating rate is from 0.01°C to $130^{\circ}\text{C}/\text{min}$ and the temperature range is from -196 to 600°C .

The optical microscope in conjunction with the heater stage was used to observe the formation and preparation of liquid crystal films and droplets on the substrates (see subsection 2.2.2), and to determine the phase transition temperatures of the liquid crystal samples. Nematic and smectic phases show characteristic textures which allow to distinguish these phases from the isotropic phase and from each other. Phase transitions are indicated by sudden changes of these textures and the transition temperatures were detected by observing the sample through the microscope, while the temperature was changed with a slow constant rate, typically $0.1^{\circ}\text{C}/\text{min}$. Typical examples for textures of the nematic and the smectic-A phase are shown in Figure 2.5.

2.3.2 Fluorescence Confocal Microscopy

Conceptualized by Marvin Minsky in 1953, the fluorescence confocal microscopy has become a practical technique in biology and biomedical sciences, as well as in materials science [101, 102], in the past 10 years. Fluorescence confocal microscopy detects structures by

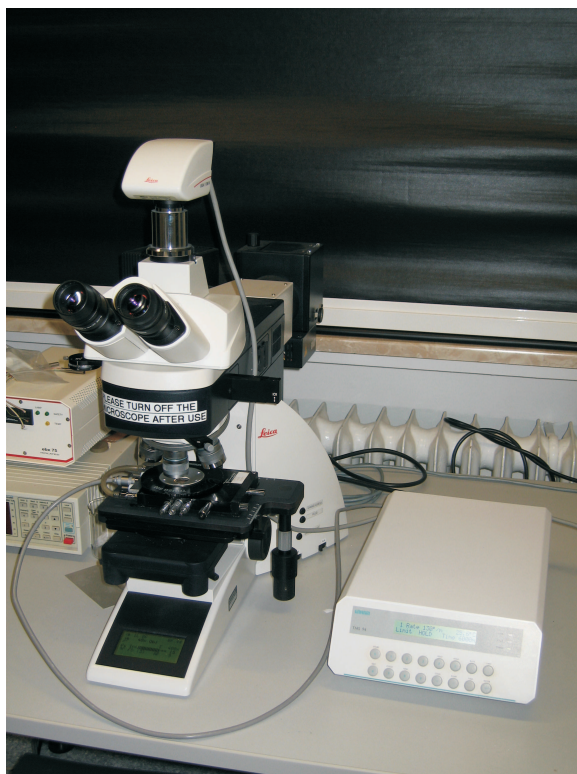


Figure 2.4: Optical microscope Leica DM4000C with TMS 94 temperature controllers and THMSG600 heater stage.

collecting light from a single focal plane of the sample, eliminating light out of focus. The light of a laser source passes through a pinhole aperture situated in a conjugate plane (confocal) with a scanning point on the specimen, and the excited fluorescence from the sample (in the same focal plane) passes a second pinhole aperture positioned in front of the detector (as presented in Figure 2.6). In this configuration, most of the fluorescence emissions above and below the objective focal plane are not collected by the detector. The confocal technique allow the study of the three dimensional (3D) structure of the sample.

A Leica TCS SP2 (Leica Microsystems) fluorescence confocal microscopy (presented in Figure 2.7) is used in my work.

Combined with polarized light, fluorescence confocal microscopy has been used for the study of liquid crystal's 3D structure [100]. According to the intensity of the polarized fluorescence light from the sample, orientational order of liquid crystals can be recognized, and the 3D structure of the liquid crystal director field can be visualized.

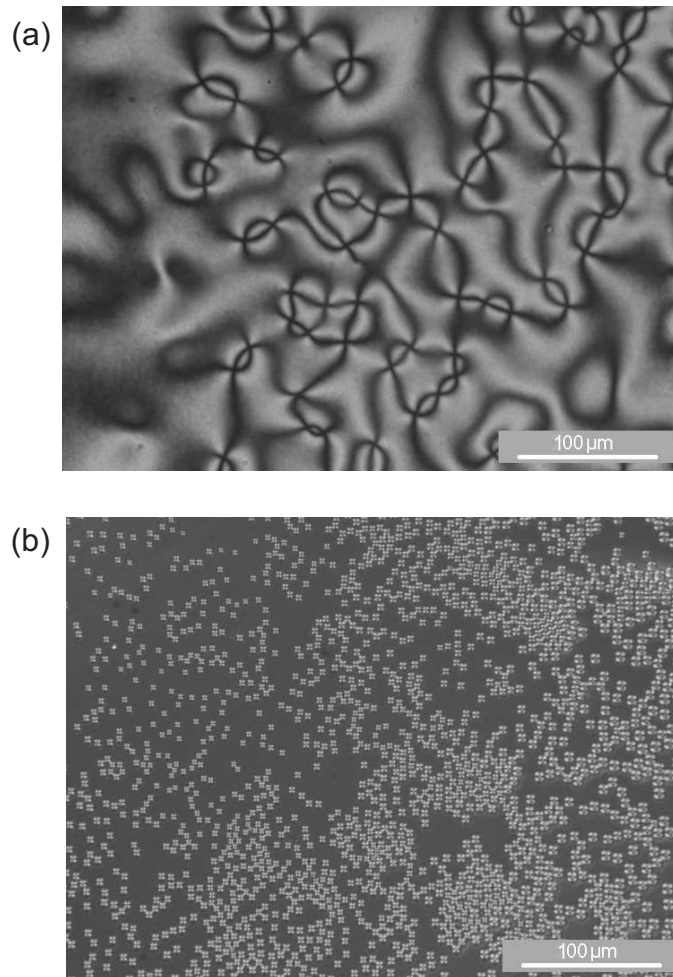


Figure 2.5: Optical microscopy with polarized light of (a) nematic phase and (b) smectic-A phase of 8CB droplet on silicon substrate.

For this purpose, the liquid crystal sample must be doped with a small amount of a fluorescent dye which align parallel to the liquid crystal molecules, i. e., the transition dipole moment of the fluorescence dye is oriented parallel to the liquid crystal director. If linearly polarized light is used to excite the fluorescence, the maximum fluorescence intensity is generated in those regions of the sample where the director is parallel to the polarization direction, and minimum intensity is obtained if the director is perpendicular to the polarization direction (Figure 2.8). In general, the fluorescence intensity I varies as

$$I \propto \cos^4 \phi \quad (2.1)$$

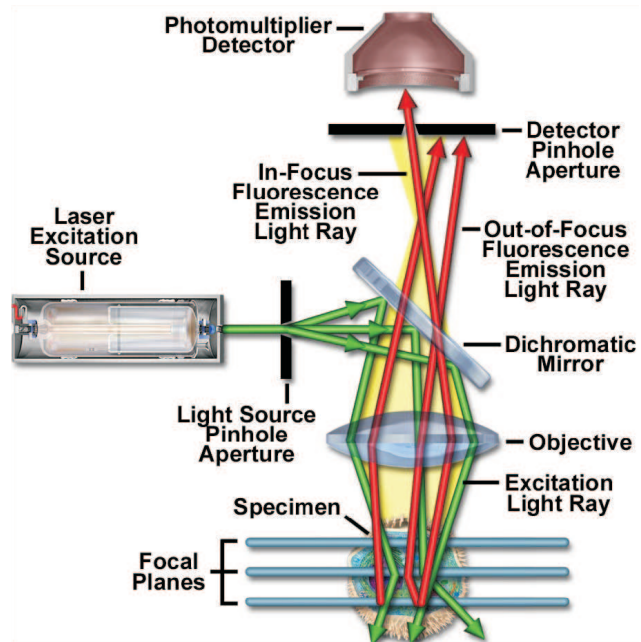


Figure 2.6: Scheme of the work principle of fluorescence confocal microscopy (from <http://www.olympusfluoview.com/>).

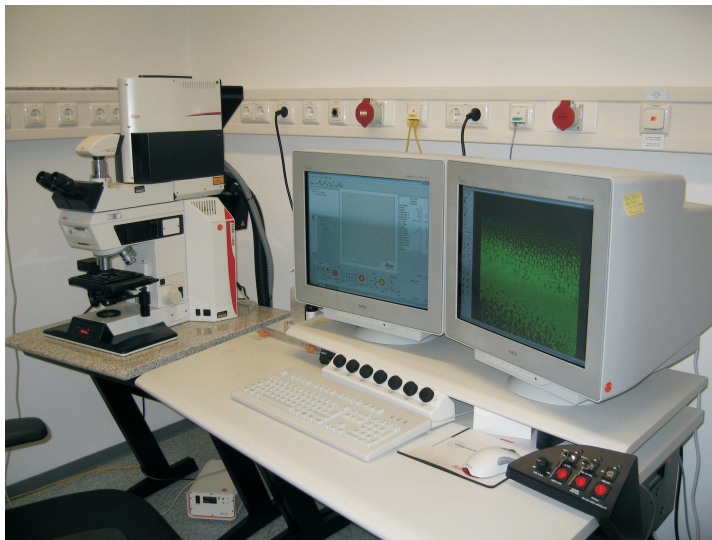


Figure 2.7: Photo of fluorescence confocal microscopy Leica TCS SP2.

where ϕ is the angle between the director (or transition dipole) and the polarization direction.

In my experiment, the fluorescent dye BTBP was used as the indicator to indicate the direction of liquid crystal molecules (director), because BTBP is well oriented along the director in liquid crystals. A tiny amount of BTBP ($\sim 0.01\%$, by weight) is doped in the liquid crystal, below the solubility limits, and stir the mixture under liquid crystal's isotropic temperature for 2-4 hours. The excitation wavelength of BTBP is 488 nm, and the emission wavelength is in a range of 510-550 nm.

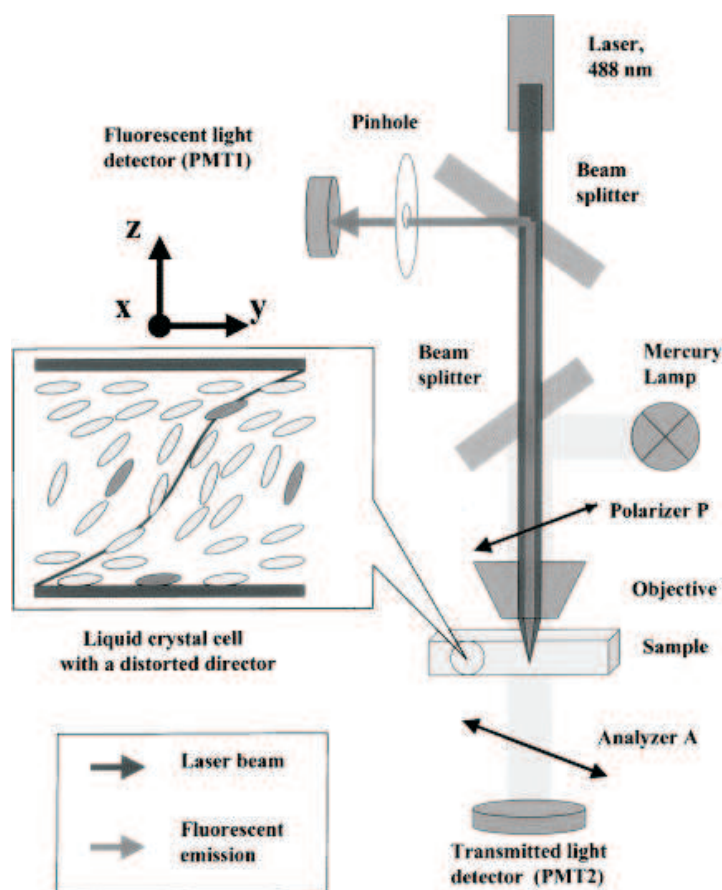


Figure 2.8: Scheme of the work principle of fluorescence confocal microscopy, cf. [100].

2.3.3 Atomic Force Microscopy (AFM)

Atomic force microscopy, invented in 1986 by Gerd Binnig, Calvin F. Quate and Christopher Herber [103], has been widely used to investigate structures and mechanical properties of materials on surfaces. Through measuring the interactive force between a sharp tip and the sample surface, AFM can offer a very high spatial resolution, near-atomic resolution, particularly on flat hard material surfaces in vacuum [104, 105]. Nevertheless, there is an increasing interest in applying AFM on soft materials [106], e. g., biological sample morphologies and polymer physical properties. In my work, AFM is used to characterize the topography of liquid crystals on different substrates, so that we can obtain information about the dimensions of focal conic domains and other structures, which are not possible to be detected by optical microscope.

Principle and Technique

Principle

The principle of the operation of an AFM is schematically shown in Figure 2.9. The key element of an AFM is its microscopic force sensor, cantilever. The cantilever is usually formed by one or more beams of silicon or silicon nitride, 100 to 500 μm long and about 0.5 to 5 μm thick. The force applied to the tip, which is mounted on the end of the cantilever, results in bending of the cantilever. The bending is detected with a laser beam, reflected from the back of the cantilever. Because the deflection of the cantilever results in a displacement of this laser beam on a position-sensitive photodetector (PSPD), it is possible to evaluate the tip-surface interactive force by measuring the cantilever deflection. The PSPD is capable of detecting tip displacements smaller than 1 nm [107]. For small deflections of the cantilever, the displacement of the beam is proportional to the force on the tip, bending the cantilever according to $N = kl$. Here, k is the elastic constant of the cantilever and l is the vertical displacement of the end of the cantilever.

In general, the measured force is contributed by the top few atoms on the tip and sample. The interactive force measured by AFM tip can be qualitatively explained by van der Waals forces [109], given for non-electrical, non-magnetic, and non-contaminated sample. The van der Waals potential energy U between tip and sample, with a distance Z , is approximated by

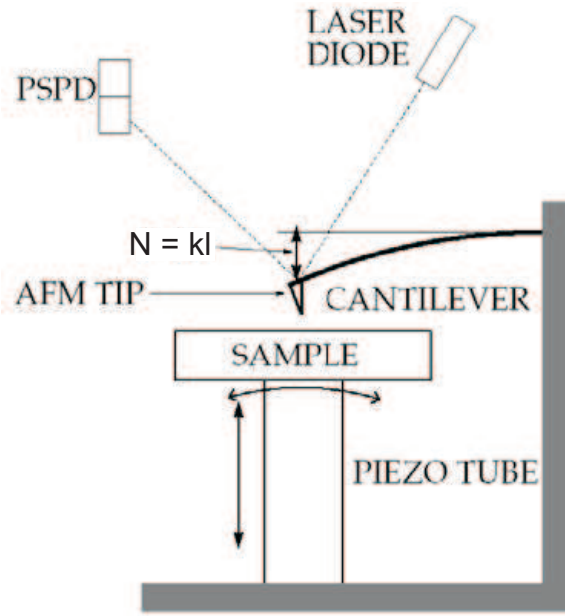


Figure 2.9: Schematic representation of an AFM operation principle. Note that the sizes of the tip and the cantilever are strongly enlarged with respect to other sizes, cf. [108].

the function — Lennard-Jones potential:

$$U(r) = U_0 \left[-2 \left(\frac{Z_0}{Z} \right)^6 + \left(\frac{Z_0}{Z} \right)^{12} \right] \quad (2.2)$$

Z_0 is the equilibrium distance between tip and sample, and U_0 is the energy at Z_0 . The first term of the above equation describes the long distance attraction due to a dipole-dipole interaction, and the second term presents the short range repulsion, resulted from the Pauli exclusion principle. At a certain distance Z_0 , the energy is the minimum (as indicated in Figure 2.10). The force is then given by:

$$N(Z) = -\frac{dU(Z)}{dZ} \quad (2.3)$$

Figure 2.11 shows a normalized plot of the forces between the tip and sample,

According to different kinds of force interactions between the tip and the sample, there are different kinds of microscope, for instance, magnetic force, electric force, and capacitive force microscopy.

From a physical point of view, one can make a distinction between different operating

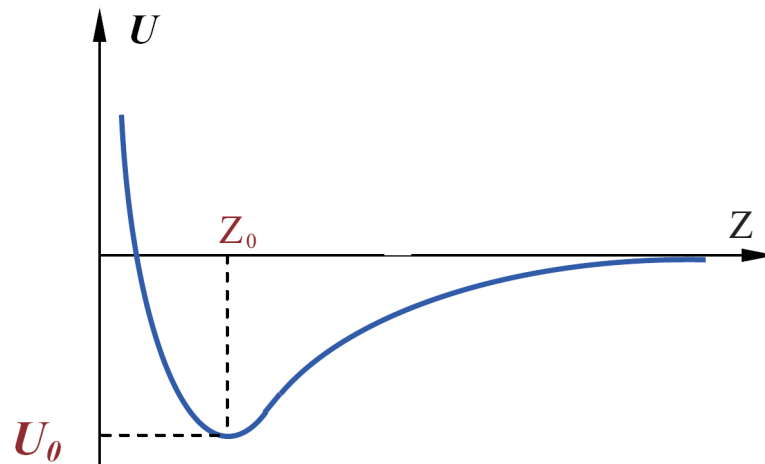


Figure 2.10: Plot of Lennard-Jones potential qualitative form, cf. [110].

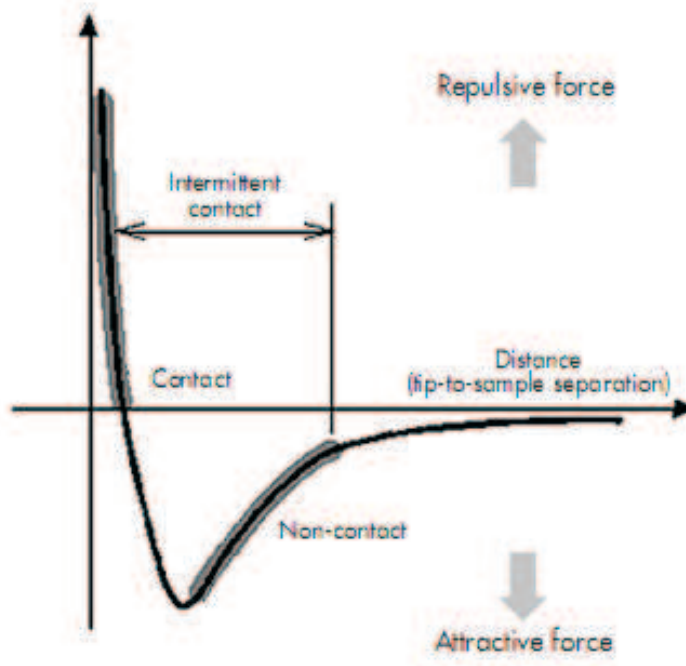


Figure 2.11: Normalized plot of the forces between the tip and sample, highlighted areas are the typical imaging mode ranges (see <http://www.veeco.com/>).

modes depending on the sign of the forces in the interaction between the tip and the sample (shown in Figure 2.11). As the tip is gradually brought close to the sample, they begin to

weakly attract each other, induced by dipole moments. The attractive force increases until the tip and sample are so close each other that a strong repulsive force is felt. This repulsive force is a result of overlapping the electron clouds from the sample and the probe tip. The Pauli exclusion principle prevents the complete overlap of the two electron clouds. This is a strong, short range force (described in the second term of Equation 2.2).

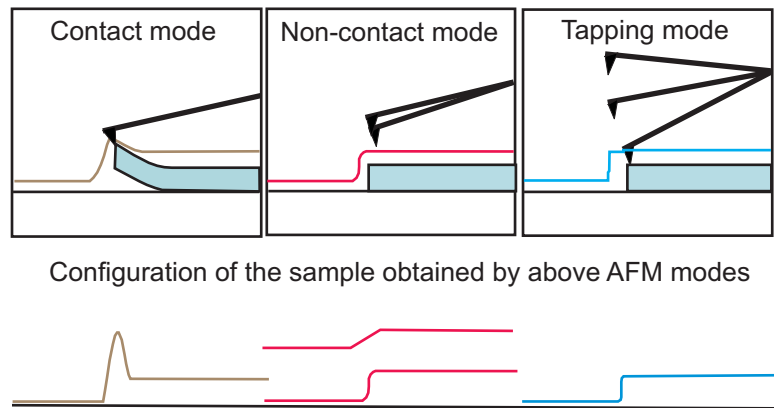


Figure 2.12: The comparison scheme of three kinds of AFM working modes: contact mode, non-contact mode, and TappingTM mode.

In accordance with different working force region, AFM can be primarily split into three groups: the contact mode (quasi-static), non-contact mode, and semi-contact mode (TappingTM mode) [111]. Figure 2.12 gives the comparison of these three AFM modes, and the difference of the configuration of sample obtained by these modes.

Contact mode

The contact mode is a mode in which the tip is brought in hard contact with the surface. In this mode of operation, the repulsive steric force is applied and tip is close to the surface (indicated as left highlight region in Figure 2.11). The static tip deflection is detected as a feedback signal.

The contact mode may be carried out either at constant force or at constant average distance. During scanning in constant force mode, the cantilever deflection, i. e., the interaction force, is kept constant by the feedback loop, and the distance between the tip and sample is detected. In the constant distant mode, scanning at a constant average distance between tip and sample, the force or cantilever deflection signal is collected.

The contact mode can provide a high sensitivity of scanning. However, in contact mode,

the cantilever pushes the tip against the sample, and the cantilever bends to force the tip atoms closer to the sample atoms. Due to this close contact between tip and surface, although cantilevers used in contact mode are relatively soft (~ 0.1 N/m), it still bears the risk of damaging or deforming the sample surface, especially for the soft materials.

Non-Contact mode

Non-contact mode is a oscillating cantilever technique, in which an AFM cantilever is oscillated far from the surface of a sample, with amplitude < 10 nm. Attractive force between the tip and the sample is dominant (indicated as right highlight region in Figure 2.11). In non-contact mode, the system oscillates a stiff cantilever near its resonant frequency. The changes of the cantilever's resonance frequency or oscillation amplitude are detected as feedback signals. Due to the long distance between the tip and sample surface, there is no contact between the tip and sample surface, which eliminate the risk of the damage of the sample surface by tip. Whereas, because the attractive force between tip and sample is typically smaller than the repulsive force of contact mode, and stiff cantilevers must be used in non-contact mode, the detector signal is smaller and the sensitivity of non-contact mode is weaker than contact mode.

Semi-contact mode (TappingTM mode)

To avoid damaging of the soft sample surface (or to do imaging of liquid surface) and improving the scanning resolution, the semi-contact mode (or called TappingTM mode) is employed in my experiments. It is operated as well by detecting the changes of cantilever's resonance frequency or oscillation amplitude.

In this mode, the cantilever is oscillated at or near its resonance frequency with a higher amplitude (typically larger than 20 nm) comparing with non-contact mode, which ensures that the tip does not get stuck in liquid layer. The repulsive force is dominant rather other attractive force (corresponding the region between two highlight region in Figure 2.11). During scanning, the tip oscillates close to the surface, so the tip alternately lightly touches and lifts off the surface. Generally, the oscillating frequency is 75-500 kHz. As the oscillating cantilever taps the surface, the oscillation amplitude and frequency are reduced, due to energy loss during tip contacting the surface. The reduction of oscillation amplitude and frequency can be used to measure the surface features. The tip/sample interaction is weaker than in the contact mode, but stronger than in the non-contact mode. Thus, TappingTM mode is much more effective than non-contact AFM, especially for imaging larger areas on the sample that may include greater variation in topography. Moreover, TappingTM mode can be performed in gases and

non-corrosive liquids.

Similar to the contact mode, the semi-contact mode can be applied in two modes, measuring the surface topography either by maintaining the frequency of oscillation (frequency-modulation mode) or the amplitude of oscillation (amplitude-modulation mode). In my experiment, the amplitude-modulation mode is applied.

In TappingTM mode, a stiff cantilever is required, and the typical value of elastic constants of semi-contact mode cantilevers are in the range from 0.01 N/m to 50 N/m. The resonance frequency of a cantilever is given by:

$$\nu_0 = \frac{1}{2\pi} \sqrt{\frac{k}{m}} \quad (2.4)$$

ν_0 is the resonance frequency of the cantilever, k and m is respectively the spring constant and mass of the cantilever.

The AFM cantilevers are very small and have a small mass. Therefore, a high spring constant cantilever has a high resonance frequency, vice versa. For softer samples, highly flexible cantilevers will less distort the sample, and for harder samples, high spring constant cantilevers are more suitable.

Experimental set up

For the AFM measurements, a Multi Mode IIIa or V (Veeco, USA) has been used, as shown in Figure 2.13. The Multi Mode is assembled with the J-type scanner, which has a scan area range limit of 214 μm^2 and z -limit of 4.65 μm . An optical microscope with a camera, used for locating a desired scanning area, is attached. To control the scanning temperature, a high temperature thermal accessory and a controller are attached. In order to stabilize the AFM scanning and reduce the thermal drifting, a water cooling system is equipped to keep the piezo of scanner at room temperature. The thermal system can heat up to 250°C.

In case of liquid crystal study, TappingTM mode AFM is applied. Details of scanning condition will be discussed in the following section. For most experiments, OMCL160TS TappingTM mode cantilevers (Olympus, Japan) were used (shown in Figure 2.14). The OMCL 160TS has a tetrahedral silicon tip on the exact end of the cantilever. Due to the sharp tip and small angle (35°) of tip, a high lateral resolution can be obtained. Furthermore, the Tetra tip is a tilted tip, so substantial tip angle decreases further when it is attached to a chip holder in AFM with a certain tilt angle (probably, 5 to 20°). The tetra tip is effective for observing rugged samples. The spring constant and resonance frequency of the cantilever are approximately 42

N/m and 300 kHz respectively.



Figure 2.13: Atomic force microscope (Multi Mode V) purchased from Veeco Instruments.



Figure 2.14: OMCL160TS TappingTM mode cantilever, Olympus, Japan. The cantilever is 4.6 μm thick, 160 μm long, 50 μm wide. The height of tip is 11 μm and radius is less than 10 nm.

AFM control and the data analysis were executed by the Nanoscope software v5.30r1 or v6.13r1.

Scanning Conditions of Liquid Crystal Samples

Since 1986, AFM has played a crucial role in nano-scale science and technique as a surface topography imaging tool, and has mostly focused on the study of solid substrates, polymer

films and biological molecules, etc. [112–114]. To better understand the alignment of liquid crystals at interface, AFM was successfully carried on the study liquid crystals interface [87, 91]. In order to avoid the influence of the capillary force between the AFM tip and liquid crystal surface, and the deformation of liquid crystal surface, the TappingTM mode is necessary for the AFM measurement of liquid crystals.

Contrary to the AFM imaging on hard solid surfaces, the imaging on liquid crystal is strongly dependent on the imaging parameters. To optimize the scanning conditions and achieve high resolution and stable AFM images, I have studied the the following AFM scanning parameters: set point, driving amplitude, scan rate, and cantilever spring constant.

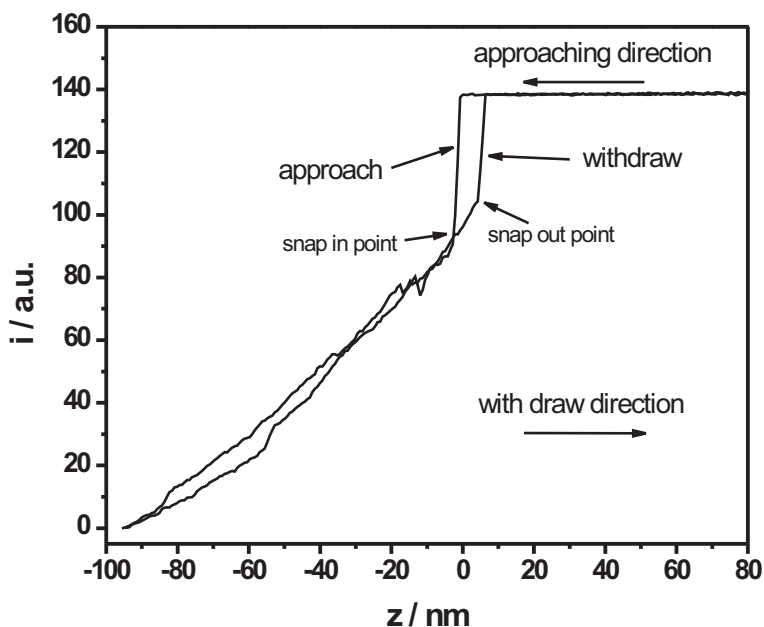


Figure 2.15: The approaching curve presenting the variation of the amplitude of the oscillating tip moving toward and withdrawing from the surface. The driving amplitude is 2 V, and tip spring constant is 66 N/m.

In all experiments, in order to obtain reproducible measurements and stable AFM images, I used ‘wetting tips’, which means that the measurement was executed with a tip that had scanned the sample surface at least 1 hour. For the measurement of droplet profiles, a small amount of 8CB (measured at 30°C) or 10CB (measured at 46°C) was placed on a bare silicon

substrate, while for sweeping experiments, a large scale liquid crystal film was prepared to avoid the lateral movement between liquid crystal and substrate.

Set point

As introduced above, in TappingTM mode AFM, the damping of the amplitude of the oscillating tip is recorded to image the topography of sample.

When a AFM cantilever, oscillating with a small free amplitude (i_0 , could be 1-100 nm) at its resonance frequency (ν_0) approaches to the sample surface, the amplitude of the cantilever will reduce and the frequency will shift, due to the van der Waals force between the tip and sample surface. So the software sets this reduced amplitude as a set point (i_{sp}), and the difference between the i_{sp} and i_0 determines the tip-sample force level, the larger i_{sp} value the weaker force, the smaller i_{sp} the stronger force. And AFM feedback loop is then activated to maintain i_{sp} by adjusting the height of the tip relative to the sample surface.

The Figure 2.15 is an approaching and withdrawing curve, which indicates the variation of the amplitude of the oscillating tip, when the tip moves toward the sample surface (from right to left of x axis) and withdraws from the sample (from left to right of x axis). The amplitude of the oscillating tip remains i_0 until the tip touches the surface and snaps in by the attractive force. Afterwards, due to the repulsive force between the tip and sample surface, the amplitude keeps decreasing until zero, where the tip touches the solid surface. During withdraw, first the amplitude keeps increasing along the approaching line, but continues after the snap-in point, and then snaps out at a certain point far away from the snap-in point. This hysteresis results from the meniscus between the tip and liquid crystal surface. In TappingTM mode, the meniscus can be get rid of easily by the cantilever oscillation with a large amplitude. Hence in order to avoid the stuck by the liquid meniscus and obtain a stable scanning, the amplitude of the oscillation is required to be larger than the meniscus size, which means that i_{sp} value must be bigger than a certain value.

Decreasing i_{sp} decreases the distance between the tip the surface, and increases the lateral and vertical resolution, but also increases the risk of accidental deformation of sample. Here I use the damping ratio γ_{sp} (i_{sp}/i_0) to define the contact extent, which is a crucial parameter for liquid crystals AFM measurements.

Figure 2.16 (a) presents a serial of sweeping curves (resonance frequency ν vs. driving amplitude i) of the tip under a certain γ_{sp} (reduced gradually from top to bottom). With decreasing γ_{sp} , the resonance amplitude firstly decreased with a small value from the free amplitude, corresponding the unstable attractive region between the tip and surface; then the resonance

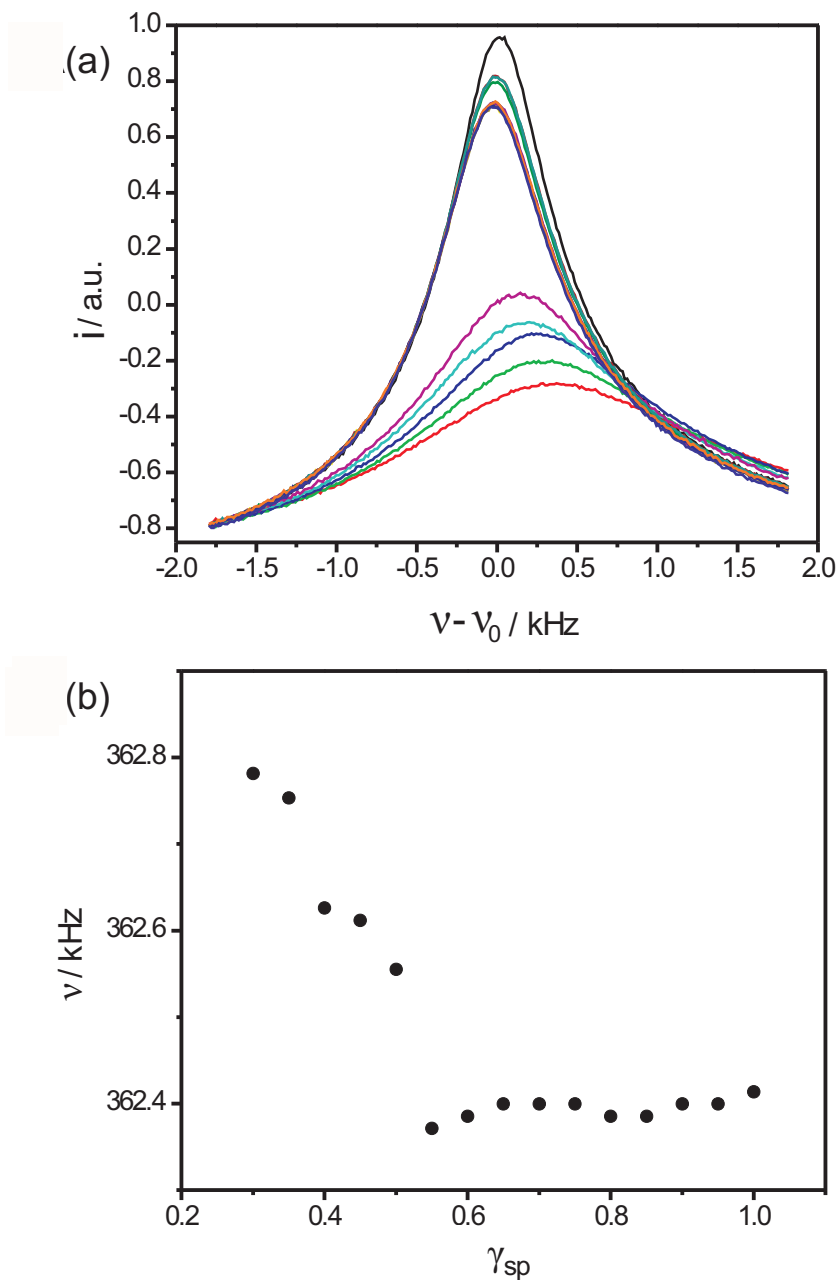


Figure 2.16: (a) A series of sweeping curves (resonance frequency of tip vs. amplitude) of different γ_{sp} values. γ_{sp} reduced gradually from top to bottom. (b) The shifting curve of frequency with different γ_{sp} values. The driving amplitude is 2 V, and tip spring constant is 66 N/m.

amplitude decreased a little further and kept this value until γ_{sp} reduced to 0.65, where the tip stably semi-contacted with the liquid surface; below 0.65, the resonance amplitude decreased rapidly, probably resulting from the damping of tip in liquid crystal. Therefore, the γ_{sp} values at the region of stable semi-contact should be selected as the working values.

Observing the shift of the frequency of the oscillating tip, I can draw the same conclusion. It is obvious that the frequency, shown in Figure 2.16 (b), first shifts to a lower value, where the tip is softly attracted by the sample surface; then as the γ_{sp} decreasing, it was reduced continually, coming from the semi-contact between the tip and sample; at last, below $\gamma_{sp} = 0.65$, the frequency was shifted to a higher value rapidly, probably corresponding to the situation of the damping of tip in liquid crystal.

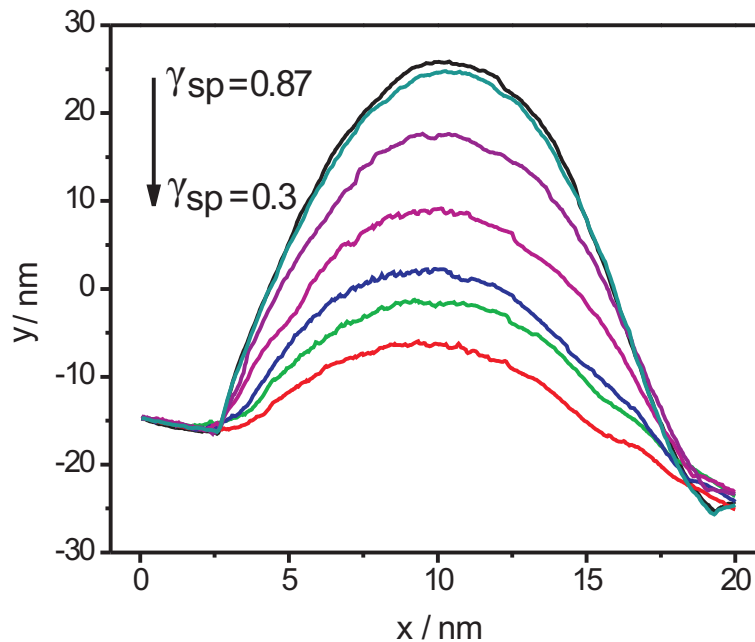


Figure 2.17: The profile of 10CB droplet on bare silicon substrate. The γ_{sp} from top to bottom are 0.87, 0.85, 0.7, 0.5, 0.4, 0.35 and 0.3 respectively. The driving amplitude is 2V, and tip spring constant is 66 N/m, and scan rate is 0.2 Hz.

Figure 2.17 gives an example of a 10CB droplet, scanned with different γ_{sp} . As the γ_{sp} value was decreasing, the droplet profile was damped and deformed after a certain value. The smectic phase sample was also checked in this way and the depth of the defects were measured with different γ_{sp} (shown in Figure 2.18). As γ_{sp} decreasing, first the tip had no contact or unstable contact with the surface, the measured depth decreased slightly, and then there was

a small flat region of measured depth within a small range of $\gamma_{sp} = 0.75-0.8$, followed by the continues decreasing of measured depth. Because of the depression of the tip on the sample surface, the depth of defect became smaller, when the γ_{sp} was decreased. It can be explained by the elastic models. When scanning a softer film, the thickness of the film will decrease as the γ_{sp} decreases [115].

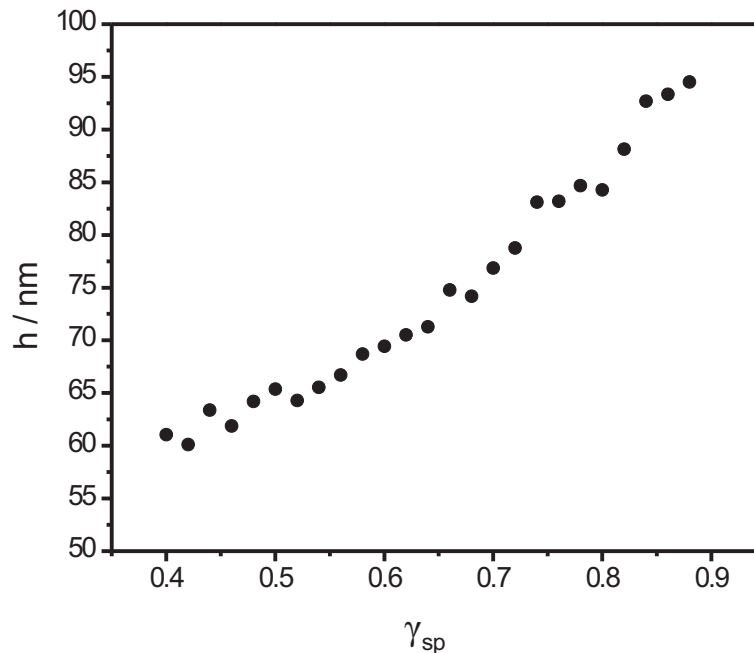


Figure 2.18: The depth of smectic-A defects obtained by AFM measurements scanned with different γ_{sp} .

Therefore, comparing all above investigations, in my experiment the value of γ_{sp} is set between 0.75 and 0.9.

Driving amplitude

Another sensitive parameter of AFM measurement on liquid crystals is the driving amplitude.

The oscillation of the tip with a large driving amplitude is stronger than the one with a small driving amplitude, and the hysteresis of the tip with a large driving amplitude is narrower than the one with a small driving amplitude (as shown in Figure 2.19). Large driving amplitude makes the tip easy to get rid of the meniscus between the tip and sample surface, so that the stable and more sensitive scanning can be performed easily. In the other hand, large driving

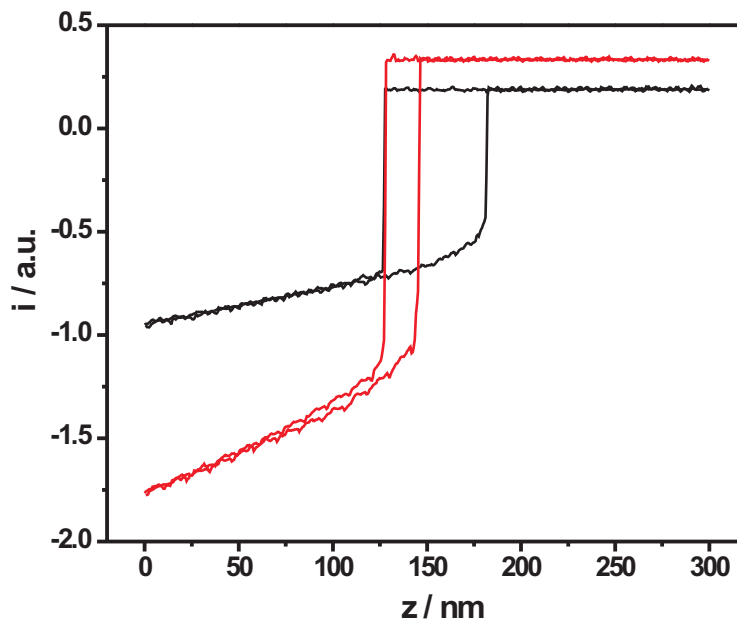


Figure 2.19: The approaching curve of a tip, spring constant 66 N/m, oscillating with driving amplitude 2 V (black) and 4 V (red).

amplitudes will cause the tip to push the liquid crystal surface, which can lead to the tip to penetrate or deform the surface of liquid crystal. From the shifting of frequency under different driving amplitudes (Figure 2.20), it is clearly observed that as the driving amplitude increased, the shifting became more obvious, which means the oscillating tip touched and penetrated the surface of liquid crystal. Besides that, the shifting started at a bigger γ_{sp} , comparable to the shifting under a small driving amplitude. It indicates that when the tip approaches the surface of liquid crystal, the one with a large driving amplitude is easier to reach to the surface than the one with a small driving amplitude, and the tip with large driving amplitude can only work with a larger γ_{sp} value. Therefore, the range of working γ_{sp} value of large driving amplitude is narrower than the one of small driving amplitude. To avoid the artifacts, the driving amplitude should be set as small as possible, but enough to break away from meniscus from liquid crystal.

Figure 2.21 gives AFM images of the profile of droplet scanning with different driving amplitudes under the same γ_{sp} . Scanning at 1 V and 2 V brought no big difference with the profile of droplet, but as the driving amplitude increasing, the profile of droplet deformed, and

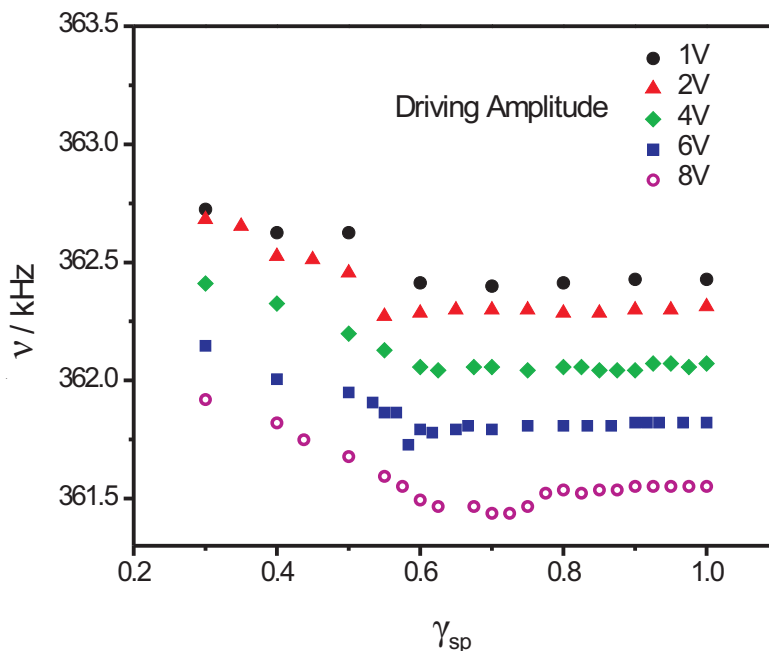


Figure 2.20: The shifting curves of frequency, corresponding to γ_{sp} , of tip drove by different amplitudes. For the sake of observation conveniently, the values of each curve are divided by a factor.

the scanning line became unstable. Here, for the amplitude, 1 V corresponds to 13.6 nm.

In the experiment, I selected the value between 1 V and 2 V as the driving amplitude.

Scanning rate

Here scanning rate per line is used to describe the scanning velocity. Different from the solid surface, the AFM of liquid crystal scanning requires a very low scanning rate. Because imaging with a slower scan rate, the tip is allowed to move over the surface with a lower velocity, which will keep the interactions between the tip and soft liquid crystal surface more stable, and result in less ‘jump’ in amplitude as features on the surface are encountered. Nevertheless, a low scan rate means a long scan time, which consumes the experiment time, as well as a long contact time between the tip and the liquid crystal surface, which could result in the damage of surface or artifacts of scanning. Scanning the 10 droplet with different scanning rates, Figure 2.22 indicates that the difference of the height of droplet from sequential scanning with high scan rate is small, but the difference with low scan rate is big, and can not be neglected for some experiments.

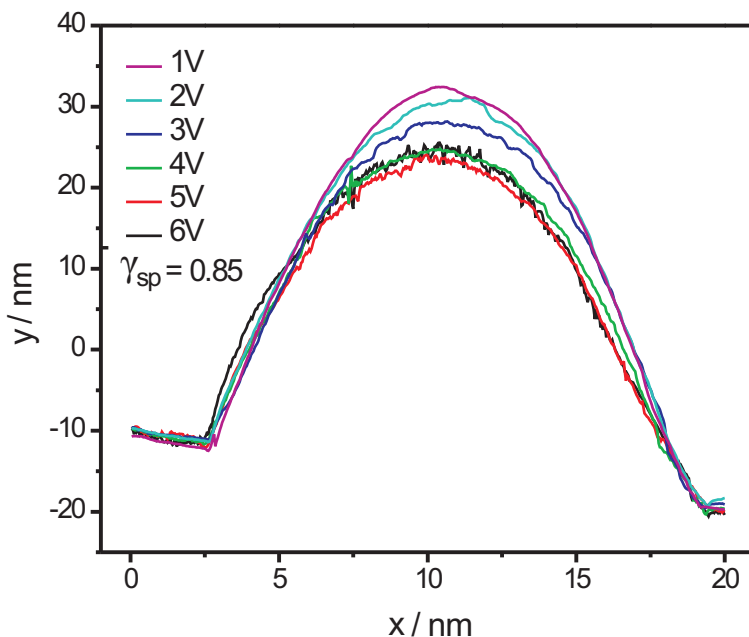


Figure 2.21: The profile of 10CB droplet on bare silicon substrate. The γ_{sp} is 0.85 and the driving amplitudes of tip from top to bottom are 1 V, 2 V, 3 V, 4 V, 5 V and 6 V respectively. The driving tip spring constant is 66 N/m, and scan rate 0.2 Hz.

Considering above two sides, the experiments were performed with the scan rate of 0.2-0.4 Hz

Tip spring constant

Contrary to AFM measurements of polymers or biological materials, liquid crystal AFM measurements can not be done with soft cantilevers. Soft cantilevers will be less sensitive, and more susceptible by liquid crystal surface. As discussed above, the tip, used in liquid crystal AFM, must be strong enough to get rid of meniscus of liquid crystal. A large driving amplitude can help to get rid of the meniscus, but a certain value of the spring constant is also necessary.

The cantilever with $k = 8.753$ N/m and 66.14 N/m were used to study the scanning condition of liquid crystal. Figure 2.23 shows different scanning regions of this two kinds of tips, depending on the parameters — driving amplitude and set point. In the non-contact region, there is no signal; in the ‘unstable’ region jumping signal is observed, which is attributed to the suck of the tip from the meniscus of liquid crystal; and the tip is completely trapped by

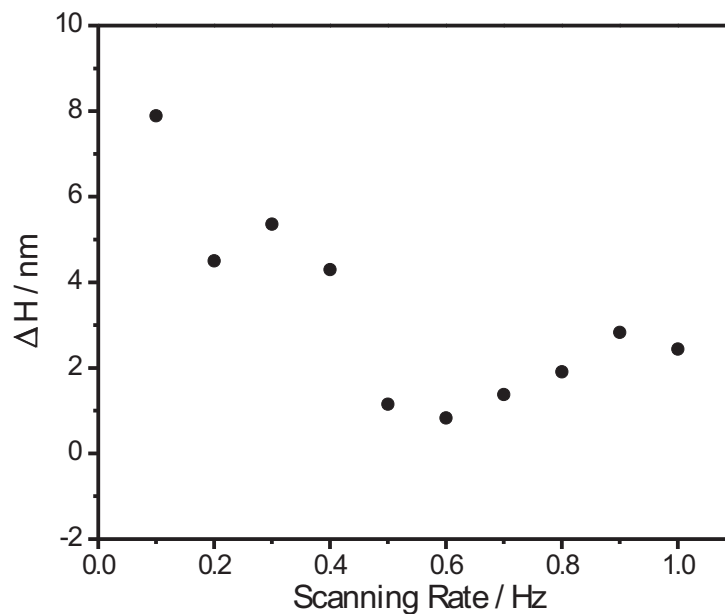


Figure 2.22: The variation of the difference of the thickness of 10CB droplet measured by sequential scanning at different scan rates (spring constant 66.14 N/m).

the liquid crystal in the damping region. In the working region, a stable signal and a sharp shape of the sample can be obtained, and it is possible to scan for hours without any apparent damage. Comparing the two working regions of the tip with $k = 8.753$ N/m and 66.14 N/m, the working region for $k = 8.753$ N/m is much smaller than that for $k = 66.14$ N/m.

Based on the discussion above, the tip with $k = 66.14$ N/m was used in my AFM measurements.

All in all, generally my AFM experiment scanning parameters were set as following: γ_{sp} between 0.75 and 0.9, driving amplitude 1-2 V, scanning rate 0.2-0.4 Hz per line, tip spring constant 50-70 N/m.

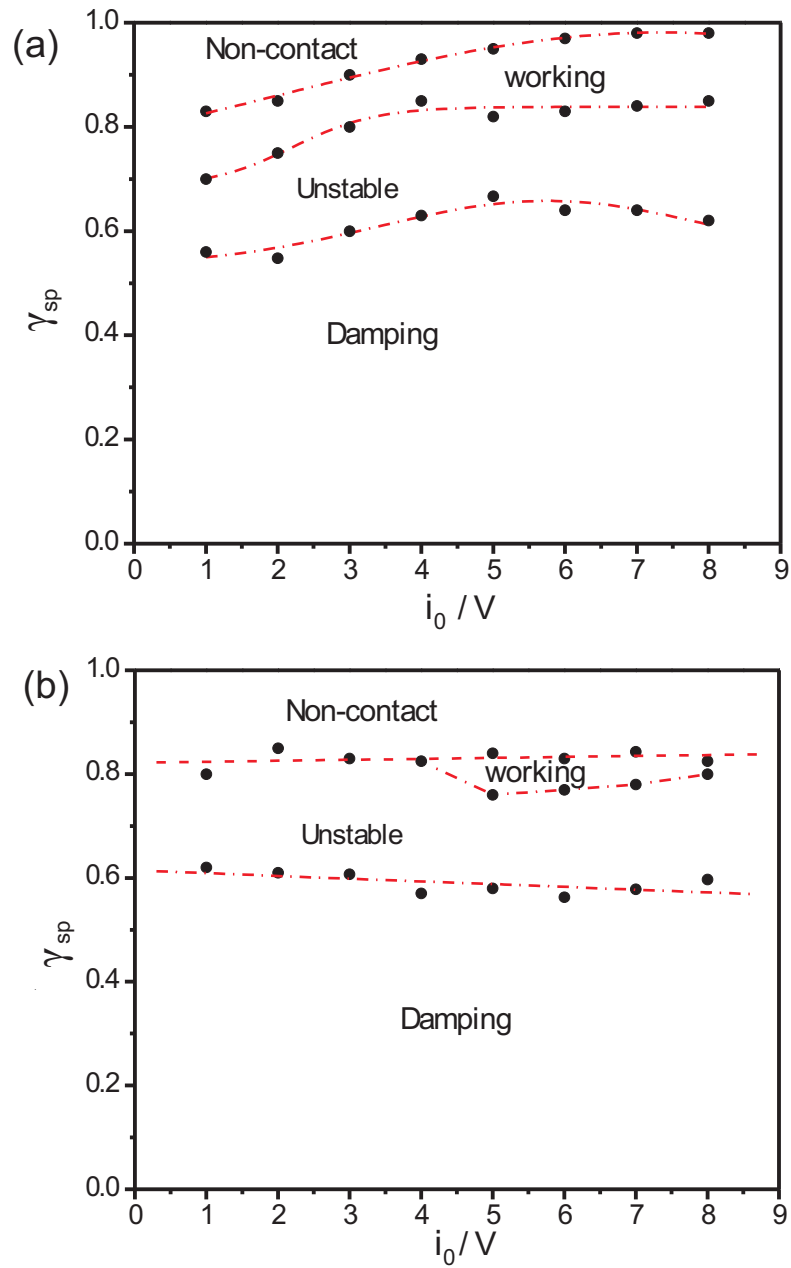


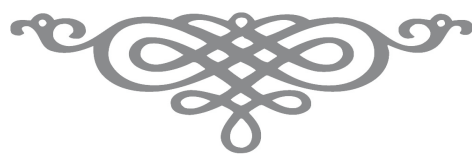
Figure 2.23: The different scanning regions corresponding to the driving amplitude and γ_{sp} with a tip (a) $k = 66.14 \text{ N/m}$ and (b) $k = 8.753 \text{ N/m}$. The lines are used to guide for eye.

The following three chapters describe the results of my thesis. The general goal of my study was an experimental investigation of the fundamental properties of focal conic domains which were generated by antagonistic anchoring conditions in μm -thick liquid crystal films on solid substrates.

Chapter 3 gives the results obtained for films on substrates possessing homogeneous random planar anchoring conditions (for a description of the different liquid crystal anchoring conditions on substrates, see Section 1.4.1, page 16). I describe the relation between film thickness and diameter of focal domains, the influence of the anchoring strength on this relation, and the behaviour at different liquid crystal phase transitions.

In Chapter 4, I introduce a method to fabricate anchoring patterns on the substrates, i. e., the modified substrate surface with homeotropic anchoring regions alternating with planar anchoring regions. This opens a way to control the positional arrangement of focal conic domains in the films and to study confinement effects.

Chapter 5 reports preliminary results obtained on substrates possessing uni/multidirectional planar anchoring conditions. On these substrates (mostly surfaces of layered crystals), linear domains are formed rather than the circular focal conic domains formed on random planar anchoring substrates.



Chapter 3

Focal Conic Domains in Films on Homogenous Substrates

“Imagination is more important than knowledge.”

Albert Einstein (1879 – 1955)

In this Chapter, I describe the behaviour of focal conic domains in films on substrates possessing homogeneous planar anchoring conditions throughout their whole surface area. Corresponding substrates are bare silicon wafers, silicon wafers coated with a thin polyethyleneimine (PEI) layer, and silicon wafers silanated with the compound n-trimethoxysilylpropyl-n,n,n-trimethylammonium chloride (MAP). On these substrates, focal conic domains can be formed in the whole substrate area, as discussed in Chapter 1. In the experiment, I found that they arrange themselves either in a regular two-dimensional hexagonal lattice, or in a less regular arrangement, in which there is a greater polydispersity in size of focal conic domains (these two cases will be discussed below).

Figure 3.1 shows an example of a smectic film with a hexagonal lattice of focal conic domains. Two quantities related to the structure of focal conic domains can be measured directly: the size (lateral diameter) of the domains can be determined by optical microscopy or by AFM measurements, and the depth of surface depressions induced by the domains can be determined by AFM measurements.

In the following Section 3.1, I present results that the size of focal conic domains is determined by the film thickness and the anchoring strength of the planar anchoring on the substrates. In Section 3.2, I study the behaviour of focal conic domains at various liquid crystal

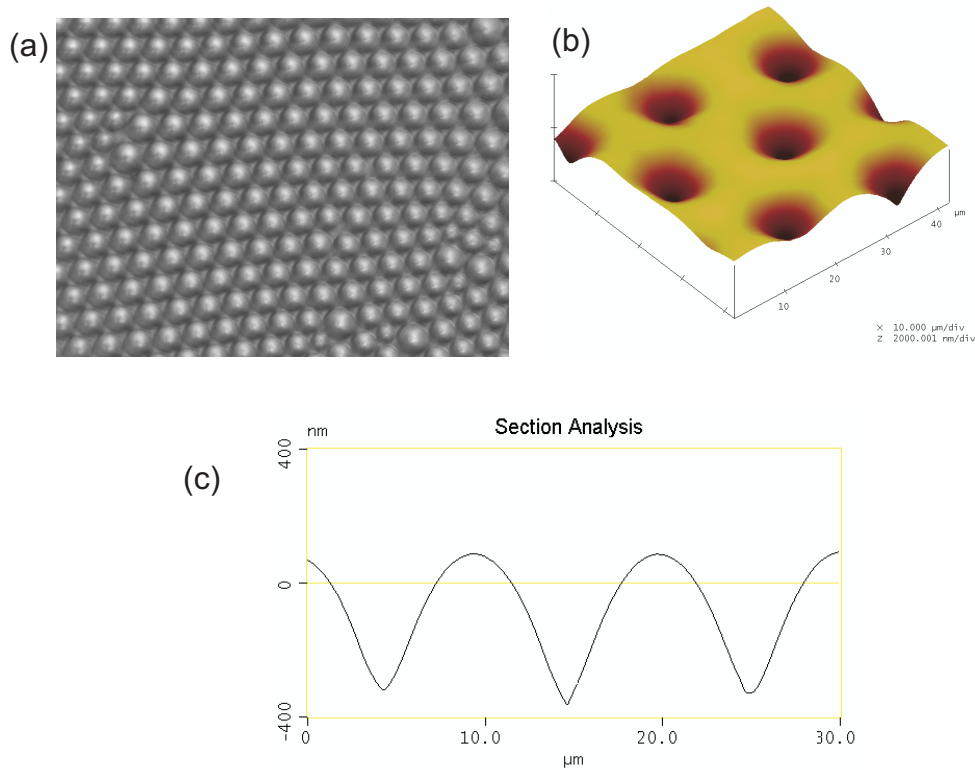


Figure 3.1: (a) Optical micrograph of a smectic film of 10CB in which focal conic domains form a hexagonal lattice. (b) AFM image of the smectic 10CB film with focal conic domains. (c) Cross section of the AFM image, indicating the depressions at the air interface induced by the focal conic domains.

phase transitions (smectic-*A* – isotropic, smectic-*A* – nematic, smectic-*C* – smectic-*A*). These results indicate that the nature of the phase sequence is an essential factor which influences the depth of the surface depressions induced by focal conic domains.

3.1 Influence of Film Thickness and Anchoring Strength

Figure 3.2 shows an optical micrograph of the edge of a flat smectic droplet with focal conic domains. There are two important observations: first, the size of the focal conic domains increases with increasing distance from the droplet edge, i. e., the domain diameter increases with increasing thickness of the smectic film. Second, in the immediate vicinity of the droplet edge focal conic domains are not observed, i. e., there appears to be a critical film thickness H_c ,

below which focal conic domains cannot be generated. Considering the anchoring condition of the air and substrate surface, it is possible to infer that in this thin film region with a thickness $H < H_c$, the strong homeotropic anchoring of the air interface enforces homeotropic anchoring also at the solid substrate interface, resulting in a defect-free film consisting of plane parallel smectic layers (the energy gain of a planar anchoring at the substrate would be smaller than the energy cost of creating focal conic domains) [85].

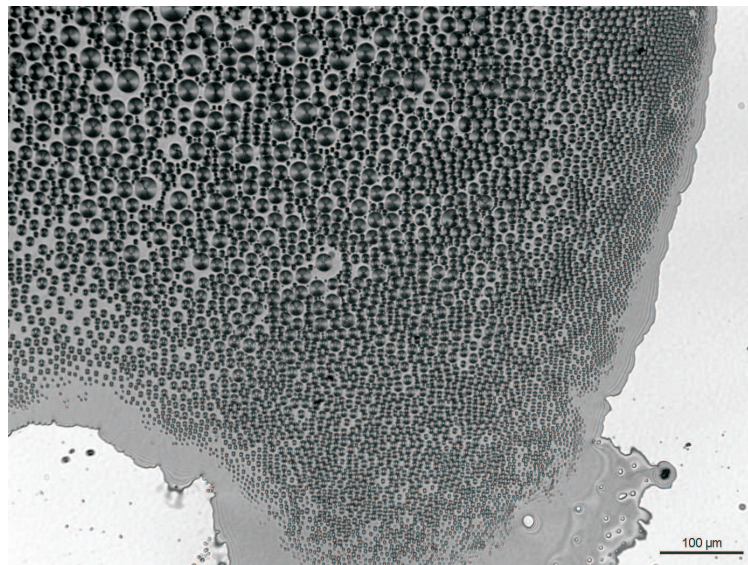


Figure 3.2: Optical microscopy image of a smectic 8CB film on a PEI-coated silicon substrate.

Figure 3.3 shows the diameter $2r$ of focal conic domains as a function of the local film thickness H in smectic films on different substrates possessing random planar anchoring conditions (bare silicon, PEI-coated silicon, MAP-coated silicon). These results confirm the qualitative observations of Figure 3.2: there is an approximately linear increase of $2r$ with H and there is a minimum value H_c below which focal conic domains are not formed. The value of H_c depends on the substrate. There may be also small differences between the slopes of the linear increase of $2r$ with H for the different substrates, but this is difficult to recognize for the data shown in Figure 3.3. Before presenting more detailed experimental results concerning this point, let us check whether the observations described above can be explained by existing theoretical models of focal conic domains in thin films.

As discussed in Chapter 1, the energy F of a focal conic domain can be written according

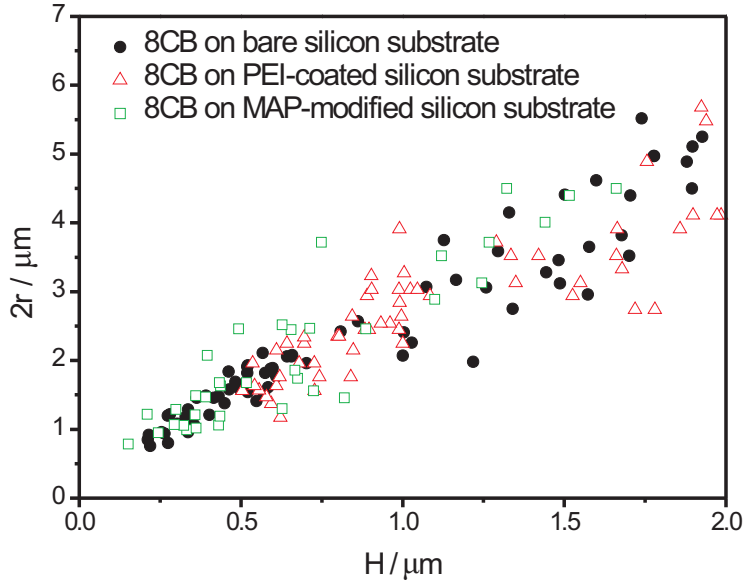


Figure 3.3: Dependence of diameter $2r$ of focal conic domains on the local film thickness H in films on three different substrates (bare silicon, PEI-coated silicon, MAP-coated silicon).

to Fournier et al. [85] as

$$F = 2\pi\beta KH + 2\pi\alpha Kr - \pi r^2 \Delta\sigma_{sub} + \frac{\pi\sigma_{air}}{12H^2} r^4 \quad (3.1)$$

Here, α and β are dimensionless unknown constants, K is a mean elastic constant, H the film thickness, r the domain radius, $\Delta\sigma_{sub}$ is the difference between smectic- A /substrate interface tensions for homeotropic and planar anchoring, and σ_{air} is the smectic- A /air surface tension. The first two terms take the energy of the two singular lines and the related curvature energy into account, the third term gives the energy decrease obtained by changing the orientation from homeotropic to planar on substrate, and the last term describes the energy cost of the increased surface area due to the deformation of the air interface induced by the underlying focal conic domain. Equation 3.1 predicts a minimum of F with respect to r , provided that r is larger than a critical value $r_c = 3\alpha K / (2\Delta\sigma_{sub})$. From $\partial F / \partial r = 0$, the following relationship between film thickness H and radius r is obtained:

$$H = \left[\frac{\sigma_{air} r^3}{6\Delta\sigma_{sub} \left(r - \frac{\alpha K}{\Delta\sigma_{sub}} \right)} \right]^{1/2} \quad (3.2)$$

Using Equation 3.2 to calculate $H_c = H(r_c)$, we obtain:

$$H_c = \left[\frac{\sigma_{air}}{2\Delta\sigma_{sub}} \right]^{1/2} \frac{3\alpha K}{2\Delta\sigma_{sub}} \quad (3.3)$$

In accordance with the experimental observations, the model of Fournier et al. predicts minimal values of film thickness and domain radius, H_c and r_c , for the generation of focal conic domains. Also the linear relation between film thickness and domain size is obtained: for $r \gg \alpha K/(\Delta\sigma_{sub})$, Equation 3.2 can be rewritten as

$$r = \left(\frac{6\Delta\sigma_{sub}}{\sigma_{air}} \right)^{1/2} H \quad (3.4)$$

Thus, the value of H_c should be proportional to $(\Delta\sigma_{sub})^{-3/2}$ and the slope of the linear part of the r vs. H curves should be proportional to $(\Delta\sigma_{sub})^{1/2}$. These results explain qualitatively the experimental observations shown in Figure 3.3, where the differences in the H_c values on different substrates are more distinct than the differences in the slopes of the $2r$ vs. H curves.

The quantity $\Delta\sigma_{sub} = \sigma_{\parallel} - \sigma_{\perp}$ is a property of the substrate, and describes the surface energy difference between planar and homeotropic anchoring of the smectic phase at the surface; the magnitude of $\Delta\sigma_{sub}$ can be regarded as the strength of the planar anchoring on the substrate. In the following, I describe a method for a systematic variation of the anchoring strength, and present further experimental results on the relation between anchoring strength and structure of focal conic domains.

The systematic variation of the anchoring strength is achieved by employing a second silane compound, octadecyldimethyl(3-trimethoxysilylpropyl)ammonium chloride (DMOAP), in addition to MAP. Whereas coating a silicon substrate with MAP imposes a random planar anchoring, coating with DMOAP leads to a homeotropic anchoring, due to a hydrocarbon side chain extending away from the substrate [80]. Coating silicon substrates with solutions of different mixtures of MAP and DMOAP generates a series of surfaces with different anchoring properties. With increasing concentration of DMOAP in the solution, the planar anchoring strength of the substrate is reduced until it becomes zero, and a transition to homeotropic anchoring takes place. By this method, the planar anchoring strength of the substrate can be continuously varied between zero and the value obtained with a pure MAP solution.

The preparation of the substrates with a series of anchoring strengths is described in Chapter 2. The mol fraction x_{DMOAP} in the solutions used for the coating ranges from 0 (pure MAP) to 10^{-3} (this small content of DMOAP is sufficient to generate a homeotropic anchoring).

More than 10 different substrates are produced and on each substrate (i. e., for each magnitude of the anchoring strength) the relation between the diameter of focal conic domains and the thickness of the smectic film is determined. Figure 3.4 shows two examples of films of the compound 8CB on two substrates coated with silane layers possessing different values of the planar anchoring strength. Again, a certain film thickness value H_c is observed, below which focal conic domains are not formed. As expected, the smaller the value of x_{DMOAP} in the substrate coating (corresponding to a larger planar anchoring strength of the substrate), the smaller the value of H_c . Above H_c , a linear relation (with the exception of the immediate vicinity of H_c) between the diameter $2r$ of the domains and the local thickness H of the liquid crystal film is observed. The slope of this linear part decreases with increasing x_{DMOAP} , (i. e., decreasing planar anchoring strength of the substrate). These results are similar to those presented in Figure 3.3, but the influence of the anchoring strength is now more distinct.

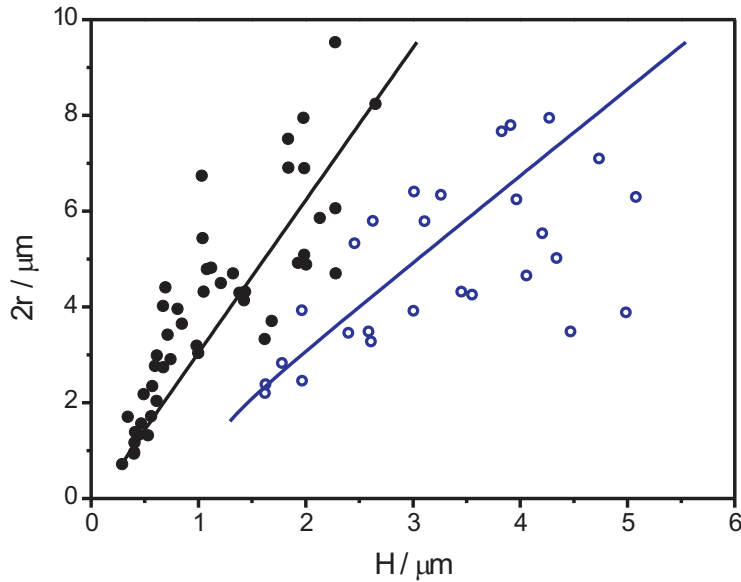


Figure 3.4: Dependence of focal conic domain diameter $2r$ on the local thickness H of 8CB smectic films on two substrates coated with different mixtures of MAP and DMOAP. Small dots: $x_{DMOAP} = 0.7 \times 10^{-4}$. Open symbols: $x_{DMOAP} = 4.0 \times 10^{-4}$ (the values of x_{DMOAP} refer to the mole fraction of DMOAP in MAP). Solid lines are fits according to Equation 3.2.

The solid lines in Figure 3.4 are fitted according to Equation 3.2 using αK and $\Delta\sigma_{sub}$ as fitting parameters. With the value $\sigma_{air} = 30$ mN/m which has been determined for 8CB [116], and under the constraint that αK should be same for both data sets (since it is a material property of 8CB), $\alpha K = 1.7 \times 10^{-9}$ N, and $\Delta\sigma_{sub} = 12.5$ mN/m ($x_{DMOAP}=0.7 \times 10^{-4}$) and

$\Delta\sigma_{sub} = 4.5 \text{ mN/m}$ ($x_{DMOAP} = 4.0 \times 10^{-4}$) for each sample are obtained. The same measurement and data evaluation is carried for all substrates prepared with different MAP/DMOAP coatings. In Figure 3.5, the obtained values of the anchoring strength $\Delta\sigma_{sub}$ are plotted as a function of the mol fraction x_{DMOAP} in the substrate coating. In addition to the compound 8CB, these measurements were also carried out for 9CB and a 3:1 mixture of 8CB and 6CB (corresponding to a hypothetical chain length of 7.5CB).

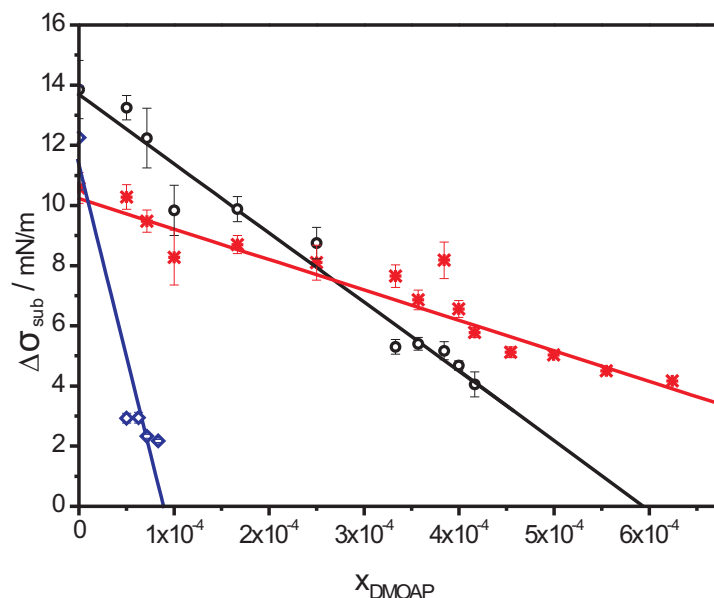


Figure 3.5: Dependence of planar anchoring strength $\Delta\sigma_{sub}$ on the mol fraction of DMOAP in the substrate coating for the LC compounds 8CB (○), 9CB (*), and a 6CB/8CB mixture corresponding to 7.5CB (◇).

The three liquid crystals behave qualitatively similar, but there are clear quantitative differences: for the mixture corresponding to 7.5CB, $\Delta\sigma_{sub}$ decreases rapidly even for very small amounts of DMOAP in the silane mixture, and it is difficult to make a definite conclusion on the $\Delta\sigma_{sub}$ vs. x_{DMOAP} relation. For 8CB and 9CB, however, a linear decrease of $\Delta\sigma_{sub}$ with increasing x_{DMOAP} is observed. Assuming a linear relation for all three liquid crystals and extrapolating to $\Delta\sigma_{sub} = 0$, we can determine a value x_{DMOAP}^0 corresponding to a neutral substrate favoring neither planar nor homeotropic anchoring; for $x_{DMOAP} > x_{DMOAP}^0$, the substrate would favor a homeotropic anchoring. For these three liquid crystals, the following values of x_{DMOAP}^0 are: 0.8×10^{-4} (7.5CB), 5.8×10^{-4} (8CB), 10.5×10^{-4} (9CB). The data indicate that with increasing alkyl chain length a planar anchoring of the smectic-A phase is inclined to form on

the MAP/DMOAP-coated substrates. This is in contrary to the behaviour of the nematic phase of the nCB compounds on gold substrates coated with self-assembled thiol monolayers. In that case, it was observed that increasing the alkyl chain length favors a homeotropic anchoring of the nematic phase [117]. However, one should note that the two studies are not directly comparable: in [117] the anchoring behaviour at a single interface of thick (several tens of μm) liquid crystal nematic films is probed, whereas the results of the present study are based on a structure formation involving both interfaces (and the complete film) of considerably thinner liquid crystal films.

The values of αK , obtained for the three liquid crystals under investigation, are 1.1×10^{-9} N (7.5CB), 1.7×10^{-9} N (8CB), and 2.4×10^{-9} N (9CB), indicating that the curvature energy of the focal conic domains increases with increasing alkyl chain length of the liquid crystal molecules.

The determination of the relation between domain size and film thickness on a given substrate can also be seen as a new method for the determination of the planar anchoring strength of the smectic phase on the substrate. The values of $\Delta\sigma_{sub}$ determined in the present study are in the range between 2 and 15 mN/m. In previous studies, anchoring strength values obtained vary over a wide range. For smectic-A/liquid interfaces (as liquid phase glycerine/lecithin mixtures, pure glycerin, water, or the isotropic phase of the LC was used), values between 3×10^{-4} and 0.1 mN/m were observed [85, 118–120]. At interfaces of solid substrates (SiO- or lecithin-coated glass) values between 4×10^{-2} and 10 mN/m have been determined [84, 121]. So far the largest values have been obtained for 8CB on MoS_2 , where $\Delta\sigma_{sub}$ amounts between 3.2 and 20 mN/m [94]. The value 15 mN/m, which is determined here for 8CB on a silicon wafer coated with pure MAP, is in the same range with the value of liquid crystals on other solid substrates, and confirms the general tendency that solid substrates may possess somewhat bigger anchoring strength values than liquid interface.

In this section, the relation between the size of focal conic domains and the film thickness was studied. It was shown, that the planar anchoring strength on the substrate is an essential factor for this relation. In general, the diameter $2r$ of focal conic domains increases nearly linearly with increasing film thickness H , provided that the film thickness is larger than a critical value H_c . With increasing anchoring strength, the value of H_c decreases and the slope of the linear $2r$ vs. H curve increases. The anchoring strength of the substrate can be controlled by coating the substrate surface with binary mixtures of silane compounds, which induce in a pure form either planar or homeotropic anchoring.

The major part of the results of this section were obtained for the compound 8CB at room

temperature. Observing focal conic domains with an optical microscope at different temperatures indicates that the domain diameter appears, if at all, only very small changes with temperature. Nevertheless, I have determined the size/thickness relation and the anchoring strength for 8CB at several temperature differences to the smectic-A – nematic transition of 8CB. Figure 3.6 shows the obtained values of $\Delta\sigma_{sub}$ as a function of temperature on a MAP-coated substrate. As expected, $\Delta\sigma_{sub}$ is almost independent of temperature, except for a slight decrease close to the transition temperature.

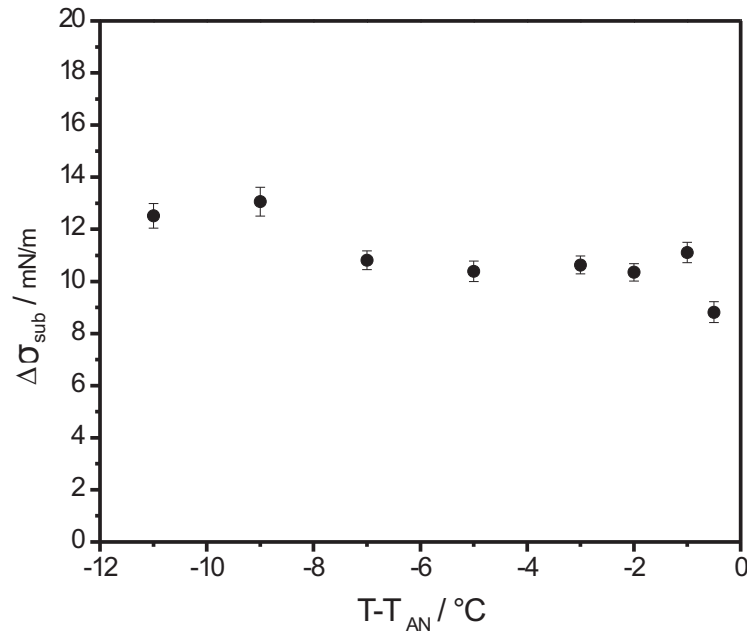


Figure 3.6: Values of $\Delta\sigma_{sub}$ as a function of temperature for 8CB on a MAP-coated silicon substrate. $\Delta\sigma_{sub}$ remains almost constant, except for a slight decrease near the transition point.

Although the size (the lateral diameter) of focal conic domains can be regarded as temperature independent, the results presented in the following section show that another important feature of focal conic domains, namely the depth of the surface depression, which is induced by each domain at the air interface of the film, can show a pronounced variation with temperature.

3.2 Behaviour of Focal Conic Domains at Phase Transitions

In this section, I will present results about the behaviour of focal conic domains at phase transitions and with temperature changing. The main part concerns the magnitude of the depth of the depression at the air interface above each focal conic domain, but first I will describe the formation process of focal conic domains, when the smectic-*A* phase is entered from the high-temperature side.

3.2.1 Formation of Focal Conic Domains at Isotropic to Smectic-*A* and Nematic to Smectic-*A* Transitions

When a liquid crystal compound passes through its phase sequence with decreasing temperature, the smectic-*A* phase is usually the first smectic phase encountered, i. e., focal conic domains are formed either at a nematic to smectic-*A* or an isotropic to smectic-*A* transition. The formation process shows different features for these two cases, and is described in the following for two compounds, 10CB and 8CB.

The compound 10CB possesses a direct isotropic to smectic-*A* transition. When a small amount of 10CB is placed on a hot bare silicon substrate, it forms a flat droplet. Cooling down slowly with a rate of $0.1^\circ/\text{min}$, firstly there appears small focal conic domains. The position of these freshly forming domains is not fixed; rather they are able to float, probably because a thin isotropic layer is present between the substrate surface and the smectic domains. As the sample is cooled down further, the size of focal conic domains increases. Their mobility enables the domains to gather into a hexagonal lattice consisting of focal conic domains in nearly equal size as shown in Figure 3.1.

The process of forming focal conic domains was recorded by fluorescence confocal microscopy (Figure 3.7). Observed in the side view geometry, the smectic-*A* phase forms initially as a uniform thin layer at the air interface, with the optical axis normal to the air interface. When the smectic film reaches a certain thickness H (depending on the cooling rate), the appearance and floating of focal conic domains near the smectic-*A*/isotropic interface is observed. The size of these focal conic domains increases with increasing smectic film thickness, and focal conic domains drift toward the center of 10CB droplet, until the smectic film reaches the solid silicon substrate. The focal conic domains then stop to flow, the size remains constant and the hexagonal lattice is formed. It should be noted that this process and the dimension of focal conic domains can depend on the cooling rate and the history. Cooling

slowly ($< 0.1^\circ/\text{min}$), the initially formed domains may decay and disappear, and one may obtain a smectic film without any defects. Cooling too rapidly ($> 0.5^\circ/\text{min}$) often prevents the Furthermore, the positions of the focal conic domains are not reproducible in subsequent heating and cooling cycles in which the transition to the isotropic phase is crossed. It is also impossible to study the domains in 10CB by AFM when the temperature is close to the phase transition point because of the mobility of the domains.

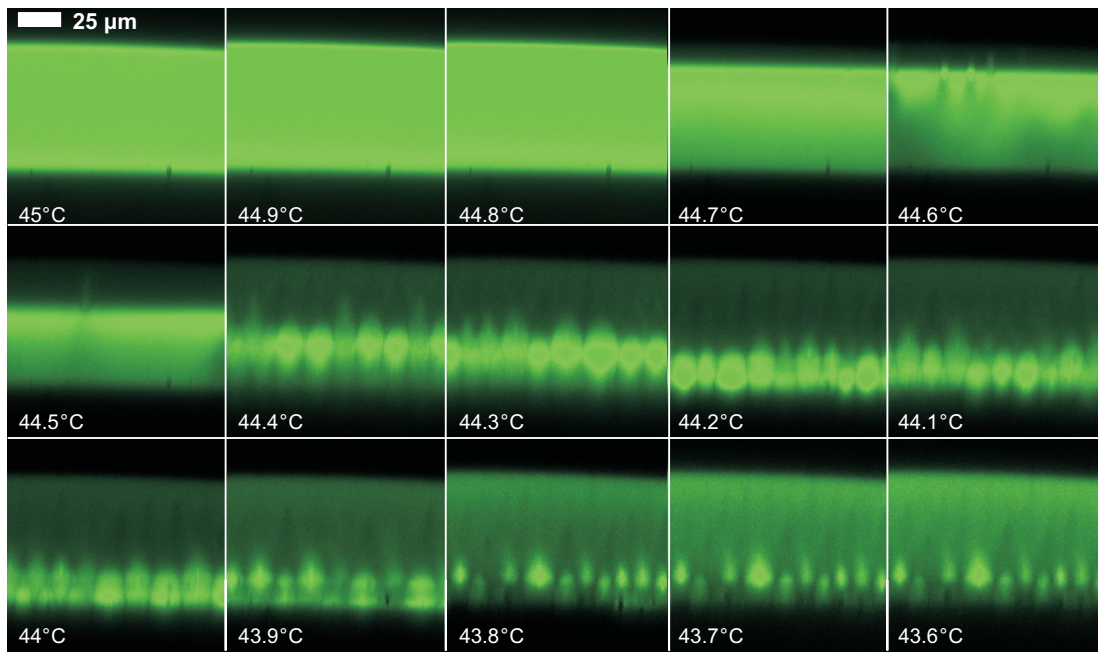


Figure 3.7: Fluorescence confocal microscopy images of the formation of focal conic domains in 10CB smectic film on bare silicon substrate around smectic-A – isotropic phase transition temperature 44°C .

The mobility of the focal conic domains at the smectic-A – isotropic transition results also in the formation of a relatively broad domain-free region at the edge of the 10CB droplets: domains possessing initially a certain size tend to drift either to the edge of film where they disappear, or join the lattice in the central region of the droplet, thereby converging into the common size of the others. This results in the presence of domains only in those regions of the droplet which are thicker than about $10\ \mu\text{m}$. As shown in Figure 3.8, in thicker films, the diameter $2r$ of focal conic domains increases with increasing film thickness H of the smectic 10CB film in a linear relation as described in the previous section.

I now turn to the case of the nematic to smectic-A transition and describe the formation of

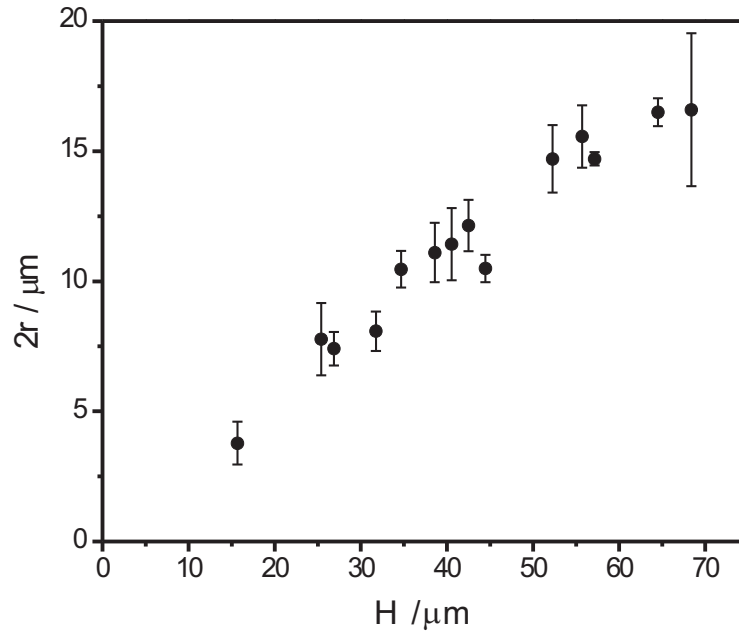


Figure 3.8: Thickness dependence of the size of focal conic domains in smectic 10CB films on bare silicon substrates. The diameter $2r$ was measured by AFM and the thickness was determined by fluorescence confocal microscopy.

focal conic domains for the compound 8CB. A small amount of nematic 8CB is placed on a bare silicon substrate where it forms a flat droplet. The temperature is cooled down with a rate of $0.1^\circ/\text{min}$ till the smectic-A phase is reached. At the smectic-A – nematic phase transition temperature point, focal conic domains are formed except close to the edge of the droplet where the local film thickness is smaller than about 200 nm.

In contrast to the case of the isotropic to smectic-A transition, there is no floating state and the appearance and the position of the domains do not change with the temperature. Even when the sample is heated up and cooled down for several cycles, the focal conic domains always appear at the same position and with the same geometry. Probably the anchoring directions on the substrate are established in the moment when the sample is placed on the substrate in the isotropic or nematic phase and do not change when the smectic-A – nematic transition is crossed several times.

Contrary to the case of 10CB, the immobility of the domains prevents the formation of a regular lattice. Rather, a less regular pattern of diverse sized focal conic domains is obtained, as shown in Figure 3.9. For instance, at a given film thickness the size of the focal conic domains varies between $3 \mu\text{m}$ and $15 \mu\text{m}$. Also incomplete and overlapping domains can be

observed. As described in Chapter 2, the contact angle of 8CB on bare silicon substrates is about 12° . Near the edge of 8CB droplets, the shape of the domains is not perfectly circular, but shows a smaller diameter at the thinner film side and a larger diameter at the thicker film side, due to the larger thickness gradient at the droplet edge. On the other hand, the size distribution for individual domains near the edge is narrower than in the center where the film thickness is larger.

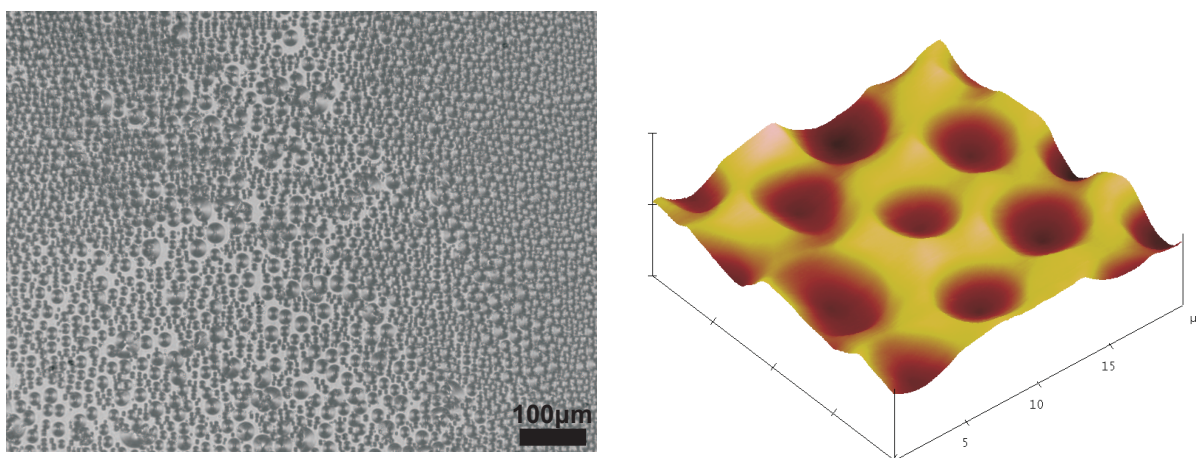


Figure 3.9: Optical microscopy image and AFM image of smectic 8CB film on a bare silicon substrate, demonstrating the size distribution of focal conic domains when formed at a nematic to smectic-*A* transition.

Based on the reasons described above, it is difficult to determine the exact relation between domain size and film thickness at least for thicker films. Nevertheless, using mean values for the domain diameter, it is obvious that the domain size increases monotonically with the thickness of the smectic film, as shown in Figure 3.10. At larger film thicknesses, however, a kind of saturation seems to exist, i. e., it is difficult to obtain very large domains in thick films of 8CB.

AFM measurements of focal conic domains in 8CB (Figure 3.11) reveal the expected convex shape of the surface depressions in thicker films. The cross section of Figure 3.11 (a) exhibits a smooth profile and a sharp minimum along the vertical axis. However, at a thickness less than $2 \sim 3 \mu\text{m}$ (Figure 3.11 (b)), the shape of the depression at the air interface appears less regular compared to thicker films. In the following subsection, I concentrate on the magnitude of the depth of the surface depression induced by focal conic domains in thicker films.

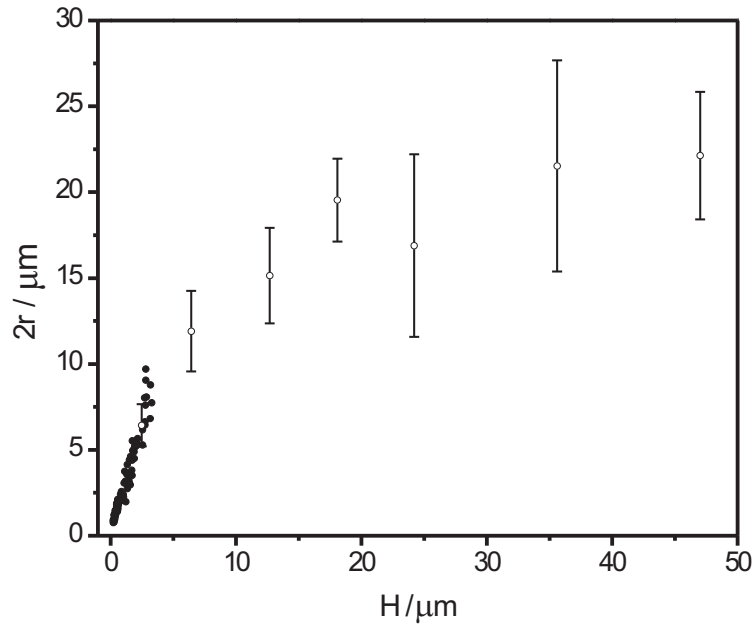


Figure 3.10: Diameter $2r$ of focal conic domains as function of film thickness H of smectic 8CB films on a bare silicon substrate with random planar anchoring. The small dots are data taken from AFM measurements, and data with bars at larger H values are from optical microscopy reflection measurements (the bars indicate approximately the size distribution of the focal conic domains).

3.2.2 Behaviour of The Depth of The Domain-Induced Depressions in The Free Surface

As shown by the AFM images in Figures 3.1, 3.9, and 3.11, each focal conic domain induces a depression at the air interface of the smectic film. In some cases, when the depth of the depression is large enough, the depressions can be also visualized by fluorescence confocal microscopy (Figure 3.12).

Which factors determine the magnitude of the depth of these depressions induced by the focal conic domains? The simplest model is based on completely incompressible layers; a cross section through the center of a focal conic domain then would appear as shown in Figure 3.13.

In the geometric model of Figure 3.13, the depth h of the depression at the smectic/air

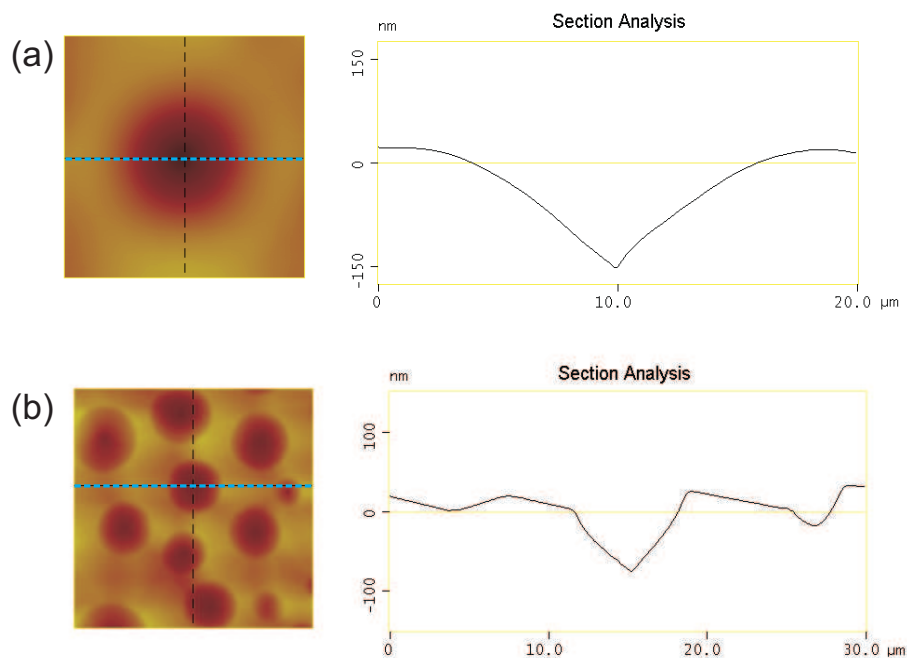


Figure 3.11: AFM images and the cross section of the focal conic domain of a smectic 8CB film on a bare silicon substrate. Figure (a) shows a focal conic domain formed at a larger thickness with $H > 5 \mu\text{m}$. Figure (b) shows a focal conic domain at a smaller local thickness ($H < 2 \mu\text{m}$).

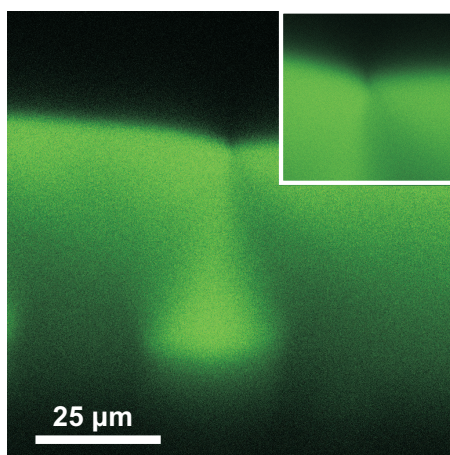


Figure 3.12: Fluorescence confocal microscopy image of a single focal conic domain in a smectic 10CB film on a bare silicon substrate. The small image in the right top corner is a magnified image of the depression induced by the focal conic domain at air interface.

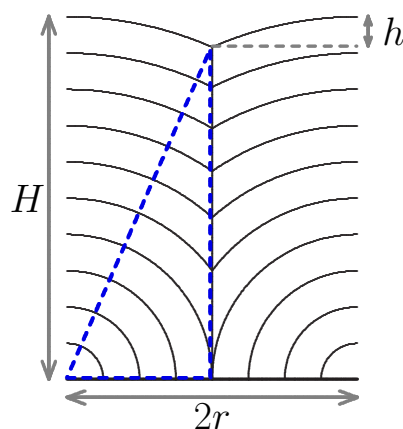


Figure 3.13: Schematic cross section through a toric focal conic domain with diameter $2r$ in a smectic film of thickness H . The bend deformation of the smectic layers leads to a depression at the film/air interface with depth h . If the cross sections of the layer planes form concentric circles, the value of h is easily calculated according to the Pythagorean theorem (triangle indicated by the dashed lines).

interface is obtained by simple geometric arguments as

$$h = H - \sqrt{H^2 - r^2}, \quad (3.5)$$

where h would depend only on the film thickness H and the domain radius r . However, measurements of h as a function of temperature show immediately that the experimental behaviour can be more complex. Figures 3.14 show the temperature dependence of h in smectic films of the compounds 10CB and 8CB. For 10CB, h does not appear to depend on temperature (as expected from Equation 3.5), but for 8CB, h decreases strongly with increasing temperature and approaches zero near the smectic-A – nematic transition (although the diameter of the focal conic domains does not change with temperature). As will be discussed at the end of this section, the temperature dependence of h is probably a result of the second-order nature of the smectic-A – nematic transition and the related vanishing of the elastic modulus, which controls the compression or dilation of the smectic layers.

The depth h of the domain-induced surface depressions can also show large changes at phase transitions between different smectic phases. Figure 3.15 shows the temperature dependence of h in films of the compounds Pyp8O8 and Pyp9O7 which show a smectic-C phase below their smectic-A phase. In both compounds, h shows a pronounced decrease at the transi-

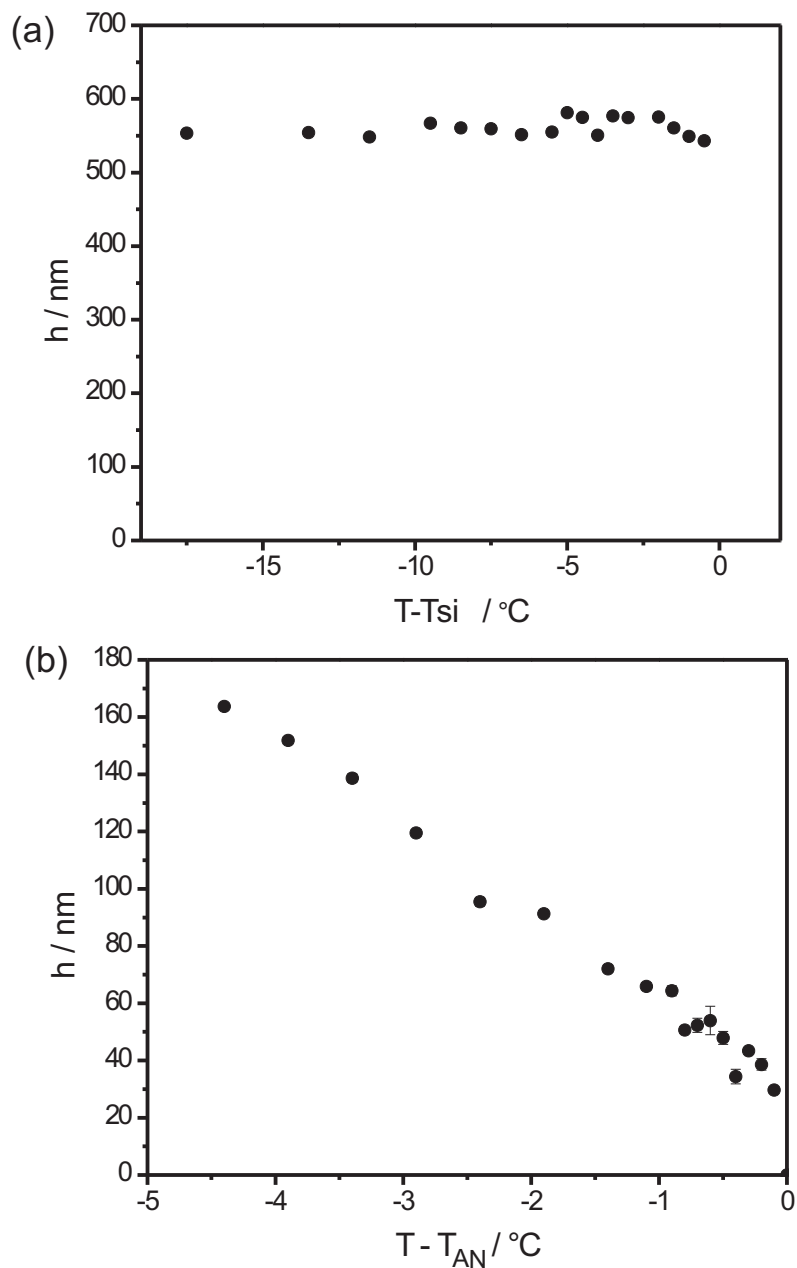


Figure 3.14: Temperature dependence of the depth h of the domain-induced depressions at the air interface of (a) a 10CB film on a PEI-coated silicon substrate; (b) a 8CB film on a PEI-coated silicon substrate, where h decreases continually and probably vanishes at the transition to the nematic phase.

tion from the smectic-A phase to the smectic-C phase. Also, the different behaviour of h in the smectic-C phase of smectic-A – nematic and smectic-A – isotropic compounds is confirmed.

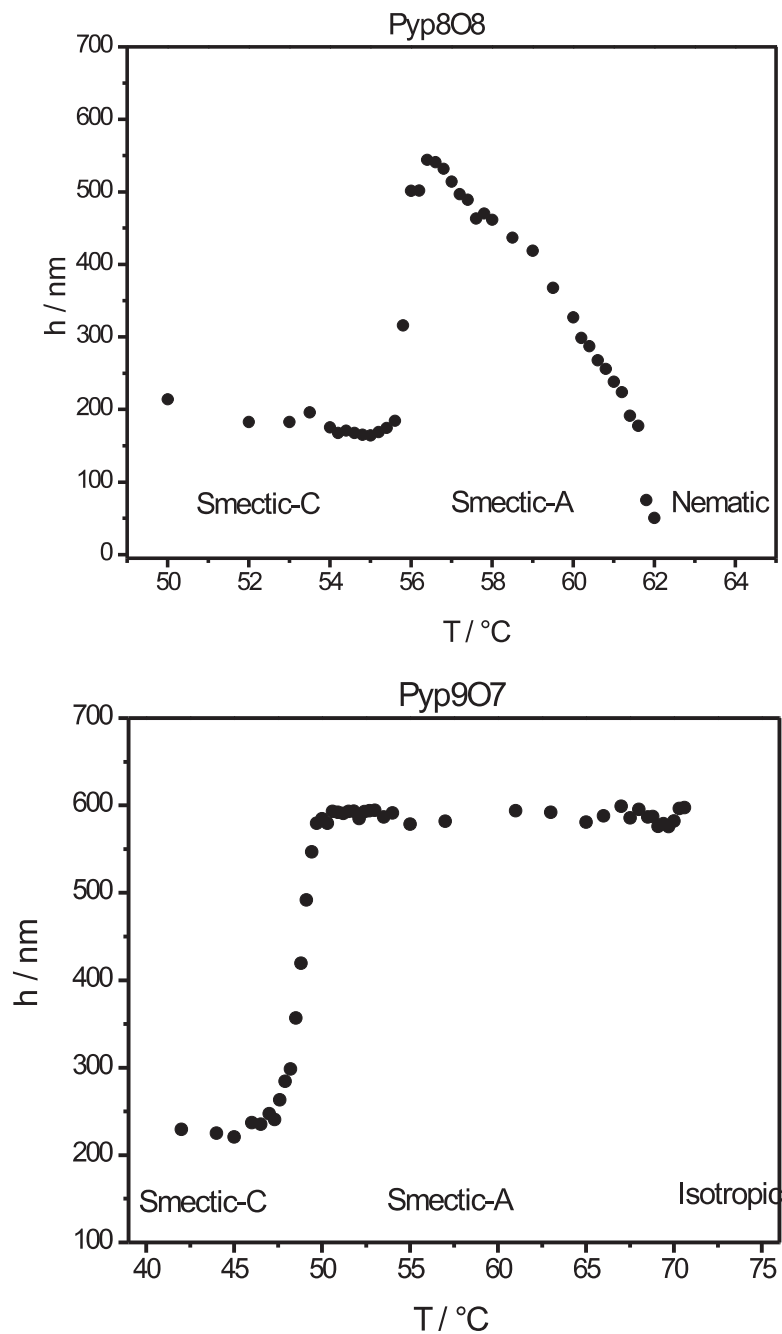


Figure 3.15: Temperature dependence of h of focal conic domains of Pyp907, and Pyp808 on bare silicon substrates.

The above described results demonstrate that the depth h of the domain-induced surface depressions can show a variety of behaviours. Therefore, I have conducted more detailed measurements for selected samples in which h was determined together with the values of film thickness H and domain diameter $2r$. Because of the dependence of the domain diameter on the film thickness (see Section 3.1), I intended to compare the different liquid crystal compounds in samples with a similar thickness value. Thus, all liquid crystal films or droplets were prepared with a thickness in the range from 40 to 45 μm , which was determined by the interface reflection measured by confocal microscopy. All AFM measurements of h were carried out in the region, where the local thickness has been previously determined by confocal microscopy. The samples are listed in Table 3.1. Besides six pure compounds, in which smectic-A – isotropic, smectic-A – nematic, and smectic-C – smectic-A transitions occur, I have also studied binary mixtures of 8CB and 10CB. As I shall explain below, in this binary system, the nature of the smectic-A – nematic transition changes from second-order to first-order with increasing mol fraction of 10CB.

In the following, I designate h_0 as the value of the depth of the surface depression that has been calculated with Equation 3.5 using the measured values of H and r (see also Figure 3.13). The experimental behaviour is then described by means of the ratio h/h_0 (h being the measured value of the depth) which can be regarded as a scale of deviation from the idealized structure shown in Figure 3.13, for which $h/h_0 = 1$. Table 3.1 gives the values of film thickness H , domain diameter $2r$, and calculated depth of the surface depression h_0 for each sample.

Figure 3.16 shows the temperature dependence of h/h_0 in the smectic-A phase for the six one-component samples listed in Table 3.1. It seems that the liquid crystal compounds can be divided into two groups. In the four compounds possessing a direct smectic-A – isotropic transition, h is not or only weakly dependent on temperature, and the values of h/h_0 are in the range from 0.8 to 1. In contrast, the two compounds possessing a smectic-A – nematic transition exhibit a pronounced temperature dependence of h and considerably smaller values of h/h_0 in the range from 0 to 0.5. The different thermal behaviour of smectic-A – isotropic (e. g., 10CB) and smectic-A – nematic (e. g., 8CB) compounds has been already described above. The values of h/h_0 close to 1 obtained here for the compounds possessing a smectic-A – isotropic transition indicate that in these compounds the structure of focal conic domains is close the idealized scheme shown in Figure 3.13.

In order to explore in more detail, the different behaviours of compounds possessing smectic-A – isotropic and smectic-A – nematic transitions, binary mixtures of 8CB and 10CB were studied. Figure 3.17 shows the temperature dependence of h/h_0 for three 8CB/10CB

Sample	H (μm)	$2r$ (μm)	h_0 (μm)
A7	44	19	1.03
C7	43	16	0.75
12CB	42	10	0.31
10CB	41	11	0.35
8CB/10CB=1:3	43	12	0.42
8CB/10CB=1:1	42	13	0.52
8CB/10CB=3:1	45	14	0.56
8CB	45	18	0.91
$\bar{8}$.S.5	46	19	0.99

Table 3.1: Film thickness H , domain diameter $2r$ and depth h_0 of the domain-induced surface depression as calculated by Equation 3.5 for the six one-component samples and three binary mixtures under investigation.

mixtures with a mol fraction of 10CB, $x_{10\text{CB}}$, equal to 0.25, 0.5, and 0.75. In the mixture with $x_{10\text{CB}} = 0.25$, the smectic- A – nematic transition is still second-order but close to a tricritical point (located at $x_{10\text{CB}} \approx 0.33$ see Section 1.5). Compared to pure 8CB, the values of h/h_0 are considerably larger and the temperature dependence near the transition is less pronounced. The mixture with $x_{10\text{CB}} = 0.5$ possesses a first order smectic- A – nematic transition; the values of h/h_0 , however, differ only slightly from those of the $x_{10\text{CB}} = 0.25$ mixture. Finally, the mixture with $x_{10\text{CB}} = 0.75$ possesses, as pure 10CB, a direct smectic- A – isotropic transition; the values of h/h_0 are lower than in pure 10CB and the temperature dependence close to the transition is more pronounced than in 10CB. These measurements on the binary 8CB/10CB mixtures show that it can be difficult to conclude from the values of h/h_0 and their temperature dependence on the nature of the smectic- A – nematic transition or even to distinguish between smectic- A – nematic and smectic- A – isotropic transitions.

In addition, I also studied another smectic phase transition – smectic- C – smectic- A phase transition. Three of the compounds, $\bar{8}$.S.5, C7, and A7, listed in Table 3.1 show a smectic- C phase below their smectic- A phase and the values of h/h_0 have been measured at and below the smectic- C – smectic- A transition. The results are shown in Figure 3.18. For the compound $\bar{8}$.S.5, a similar behaviour as described above for the compounds Pyp8O8 and Pyp9O7 is observed: there is a remarkable decrease of the h/h_0 values near the transition temperature, and the values remain essentially constant in the smectic- C phase. The compounds C7 and

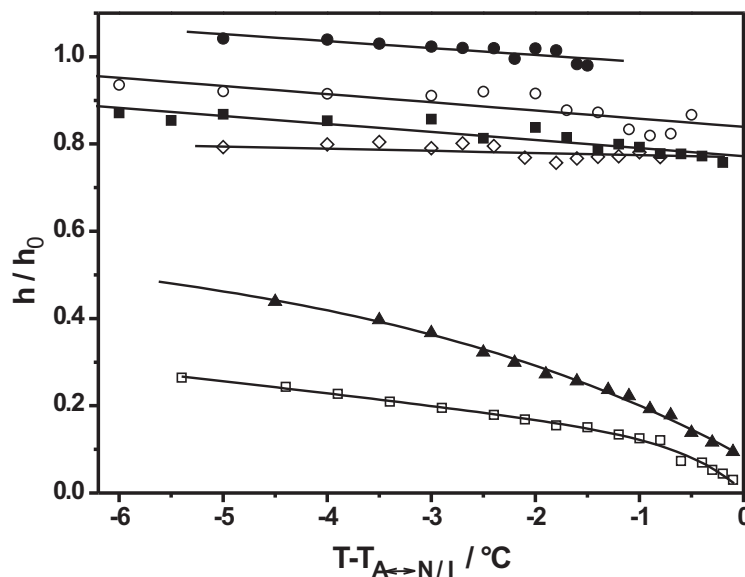


Figure 3.16: Temperature dependence of the ratio h/h_0 (h : measured depth of the domain-induced surface depressions, h_0 : calculated values using Equation 3.5) in $\approx 40 \mu\text{m}$ thick films of the compounds 12CB (\bullet), A7 (\circ), C7 (\blacksquare), 10CB (\diamond), $\bar{8}.S.5$ (\blacktriangle), and 8CB (\square). $T_{A \leftrightarrow N/I}$ designates the smectic-A – nematic or smectic-A – isotropic transition temperature.

A7 behave completely different: C7 shows a small but sharp decrease of h/h_0 at the transition from the smectic-A to the smectic-C phase, then the values increase in the smectic-C phase with decreasing temperature until values close to 1. For the compound A7, the magnitude of h/h_0 does not appear to change at the smectic-C – smectic-A transition; within the smectic-C phase, there is a slight increase to $h/h_0 \approx 1$ with decreasing temperature. The compounds C7 and A7 differ from the compound $\bar{8}.S.5$ by the fact that they possess a higher ordered phase, probably crystal-G, below their smectic-C phase.

In general, the experimental behaviour of the depth h of the domain-induced surface depressions can be summarized as follows: the values of h can vary in wide range from values close to h_0 (the value expected by geometric arguments for incompressible layers, see Equation 3.5) down to values considerably smaller than h_0 . In the smectic-A phase of compounds showing a smectic-A – isotropic transition, h amounts to values relatively close to h_0 , i. e., $h/h_0 \approx 0.8$ to 1. The compounds possessing a second-order smectic-A – nematic transition

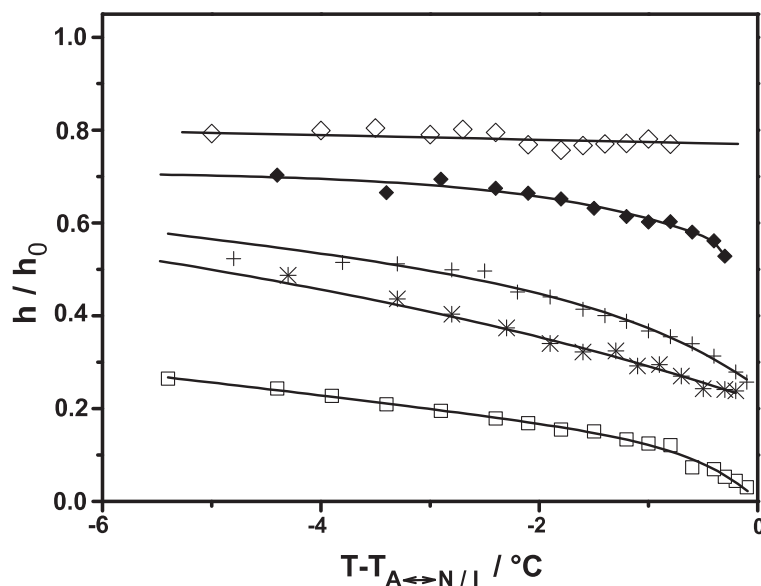


Figure 3.17: Temperature dependence of the ratio h/h_0 (h : measured depth of the domain-induced surface depressions, h_0 : calculated values using Equation 3.5) in $\approx 40 \mu\text{m}$ thick films of the compounds 10CB (\diamond), 8CB (\square), and three 8CB/10CB mixtures with x_{10CB} equal to 0.25 (*), 0.5 (+), and 0.75 (\blacklozenge). $T_{A \leftrightarrow N/I}$ designates the smectic-A – nematic or smectic-A – isotropic transition temperature.

show in their smectic-A phase considerably smaller values of h/h_0 and a pronounced temperature dependence with h/h_0 ranging from 0.5 far below the transition to the nematic phase down to 0.05 near the transition.

There is, however, no sharp boundary between these two groups of compounds: the study of a binary system of 8CB and 10CB shows that h/h_0 varies smoothly as one proceeding from second-order smectic-A – nematic over first-order smectic-A – nematic to smectic-A – isotropic systems. In the smectic-C phase, the behaviour seems to depend on the phase sequence below the smectic-C phase: compounds which possess a less ordered phase below their smectic-C phase show a pronounced decrease of h at the smectic-A to smectic-C transition. In compounds possessing a more ordered phase below their smectic-C phase, the value of h is essentially not affected by the smectic-A – smectic-C transition, and h increases slightly with decreasing temperature within the smectic-C phase. Three of the compounds under investigation show a smectic-C phase below their smectic-A phase. In $\bar{8}.S.5$, h/h_0 decreases considerably at and below the transition to the smectic-C phase. In the following subsection, I show that most of the experimental observations can be at least qualitatively explained by the

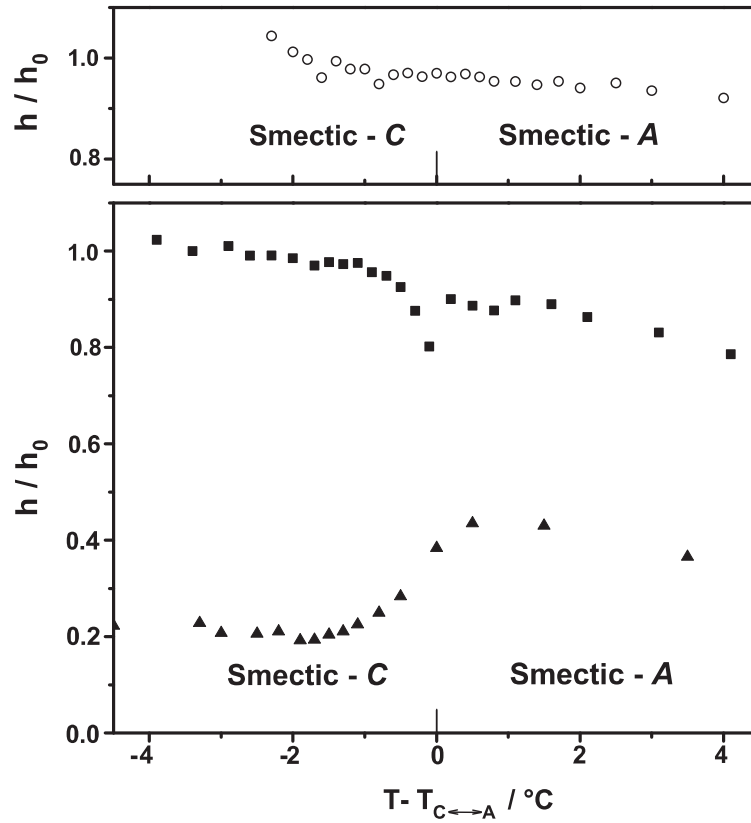


Figure 3.18: Temperature dependence of the ratio h/h_0 (h : measured depth of the domain-induced surface depressions, h_0 : calculated values using Equation 3.5) in $\approx 40 \mu\text{m}$ thick films of the compounds A7 (\circ), C7 (\blacksquare), and 8.S.5 (\blacktriangle). $T_{C\leftrightarrow A}$ designates the smectic-C – smectic-A transition temperature.

elastic properties controlling the compression or dilation of the smectic layers.

3.2.3 Relation to The Layer Elastic Modulus B

The presence of the depressions induced by focal conic domains increases the area of the film/air interface compared to a completely flat interface. In a focal conic domain, the smectic film is thus subjected to a dilative stress, which could result in a thickness increase, corresponding to a decrease of h , of the smectic film in the central region of the focal conic domains. The reduction of the depth h of the depressions produced by this dilation would result in an energy gain $\sigma_{air}\Delta A$, where σ_{air} is the film/air interface tension and ΔA is the corresponding change of the interface area. In my experiment, it was observed in several cases that the value

of h/h_0 is smaller than 1, indicating that the film thickness in the central region of the focal conic domains is larger than in the idealized structure shown in Figure 3.13. Two possible mechanisms could lead to the increase of the local film thickness in the central region of the toric focal conic domains: the creation of new smectic layers, i. e., the generation of edge dislocations around the straight singular line of the focal conic domains, or a dilation of the smectic layers in this region.

The compounds 8CB and $\bar{8}.S.5$ show a pronounced temperature dependence of h/h_0 , which increases with decreasing temperature with a value of ≈ 0.05 close to the smectic-A – nematic phase transition and a value of 0.2 (8CB) or 0.5 ($\bar{8}.S.5$) at the temperature of 5°C below the transition. This process is reversible with respect to the heat and cooling cycle, only with a slight hysteresis effect observed (cf. Figure 3.19). If the creation of edge dislocations would be responsible for the temperature dependence of h , edge dislocations have to be continuously and reversibly generated and annihilated with increasing or decreasing temperature, respectively. This is an unlikely scenario since the spontaneous generation of edge dislocation is associated with an energy considerably larger than $k_B T$ [122]. Therefore, the temperature dependence of h and the deviation of h/h_0 from 1 are probably a result of the elastic properties controlling the compression or dilation of the smectic layers.

As described in Section 1.5, the compression or dilation of smectic layers is controlled by the elastic modulus B and the related energy density f is written as

$$f = \frac{1}{2} B e^2 \quad (3.6)$$

with $e = (d - d_0)/d_0$ describing the deviation of the actual smectic layer thickness d from its equilibrium value d_0 . Typical values of B are of the order of 10^7 N/m², which means that under normal conditions the smectic layers can be regarded as nearly incompressible. However, a number of studies has shown that B becomes small when a second-order smectic-A – nematic transition is approached from a temperature below the transition temperature (see Section 1.5). A small value of B allows for a dilation of the smectic layers in the central region of the focal conic domains, and leads to small values of h/h_0 as observed for 8CB and $\bar{8}.S.5$ on approaching the nematic phase transition. For both compounds, measurements of the absolute value of B have been carried out [37–39]. At a given temperature different to the smectic-A – nematic transition, the magnitude of B in $\bar{8}.S.5$ is approximately four times larger than in 8CB. Accordingly, the values of h/h_0 in $\bar{8}.S.5$ should be bigger, i. e., closer to 1, than in 8CB, as is indeed the case (cf. Figure 3.16): the h/h_0 values in $\bar{8}.S.5$ are approximately two times

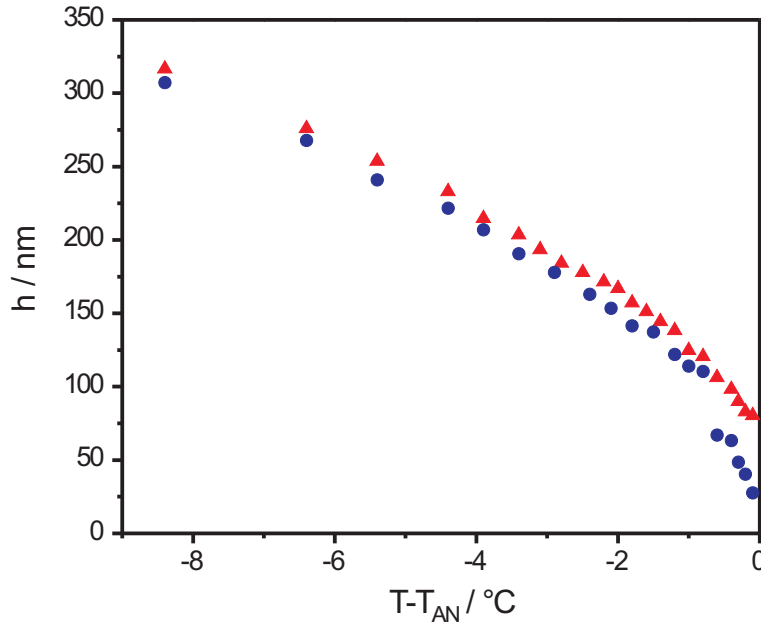


Figure 3.19: Temperature dependence of the depth h of the domain-induced surface depressions in a smectic 8CB film with a thickness of $\approx 42 \mu\text{m}$ on a MAP-coated substrate. The heating (red \blacktriangle) and cooling (blue \bullet) cycle shows a slight hysteresis.

larger than in 8CB. Unfortunately, we did not find any measurements of B for 10CB or 12CB (or any compound with a direct smectic- A – isotropic transition). The h/h_0 values of these compounds are close to 1 and we would expect considerably larger B values than in 8CB.

The behaviour of B at smectic- A – smectic- C transitions has been studied for a number of compounds but not for $\bar{8}.S.5$, A7, or C7. In [49, 50], a minimum of B at the transition temperature has been observed, which is followed by an increase of B with decreasing temperature within the smectic- C phase. For $\bar{8}.S.5$, we find that h/h_0 values decrease as approaching to the smectic- C phase transition, but within the smectic- C phase, the values stay at a low constant level. For the compounds A7 and C7, we observe, if at all, only a minor effect of the transition to the smectic- C phase on the values of h/h_0 . Although the values of h/h_0 in these compounds are already close to 1, they increase slightly with decreasing temperature in the smectic- C phase. A pronounced increase of B in a smectic- C phase has been observed near a smectic- C – hexatic- I critical point [123]. The increase of h/h_0 in the smectic- C phase of A7 and C7 might also result from the development of hexatic order, since these compounds show, in contrast to $\bar{8}.S.5$, a more ordered phase below their smectic- C phase.

In addition to the qualitative arguments described above, I tried a more quantitative test of

the relation between h/h_0 and B by comparing the energy Δw_{surf} gained by a decrease of the surface area (by a decrease of h) and the energy Δw_{dil} paid for an increase of the film thickness (by a dilation of the smectic layers). If the shape of the focal conic domains-induced surface depression is approximated by a right circular cone with axis length h and base diameter $2r$, Δw_{surf} is given by

$$\Delta w_{surf} = \sigma_{air} \pi r \left(\sqrt{r^2 + h_0^2} - \sqrt{r^2 + h^2} \right) \quad (3.7)$$

In order to estimate the magnitude of Δw_{dil} , the focal conic domain is treated in a rough approximation as a smectic cylinder with height H , diameter $2r$, and elastic modulus B ; the curved arrangement of the smectic layers is ignored, instead it is assumed that the layers form a simple stack with the layer normal being everywhere parallel to the cylinder axis. Δw_{dil} is then given by integrating Equation 3.6 over the volume V of the cylinder:

$$\Delta w_{dil} = \int_V \frac{1}{2} B e^2 dV \quad (3.8)$$

The dilation e is assumed to decrease linearly with radial distance ρ from the center of the focal conic domain, i. e., at the center of the domain ($\rho = 0$), $e = (h_0 - h)/H$, and at the perimeter ($\rho = r$), $e = 0$:

$$e = \frac{h_0 - h}{H} \left(1 - \frac{\rho}{r} \right) \quad (3.9)$$

The integration in Equation 3.8 then gives

$$\Delta w_{dil} = \frac{\pi B (h_0 - h)^2 r^2}{12H} \quad (3.10)$$

From the equilibrium condition $\Delta w_{surf} + \Delta w_{dil} = 0$, the value of h/h_0 as a function of B is calculated numerically for given values of r , H , and σ_{air} . Figure 3.20 shows two examples obtained with $\sigma_{air} = 0.03$ N/m, $H = 45$ μm , and $r = 5$ μm or $r = 10$ μm , respectively. The positions of the experimental data for the two compounds $\bar{8}$.S.5 and 8CB, for which both B and h/h_0 are available, are also indicated in Figure 3.20. It is obvious that there is a large discrepancy. According to the my model, 8CB and $\bar{8}$.S.5 either have considerably larger measured values of h/h_0 , or possess values of B one or two orders of magnitude smaller than reported. One reason for this discrepancy is certainly the simplicity of the model which neglects the curved smectic layer structure in a focal conic domain. For instance, it was shown that the smectic layers in a focal conic domain show an intrinsic dilation near the two singular

lines [124]. The magnitude Δh_i of the resulting change of h has been estimated as [91]:

$$\Delta h_i = -\lambda \log \frac{H}{\lambda} \quad (3.11)$$

with $\lambda = \sqrt{K_1/B}$. However, taking this intrinsic dilation into account in the model (setting the splay elastic constant K_1 to a typical value of 10^{-11} N) results only in a minor modification of the predicted relation between h/h_0 and B (cf. dashed lines in Figure 3.20).

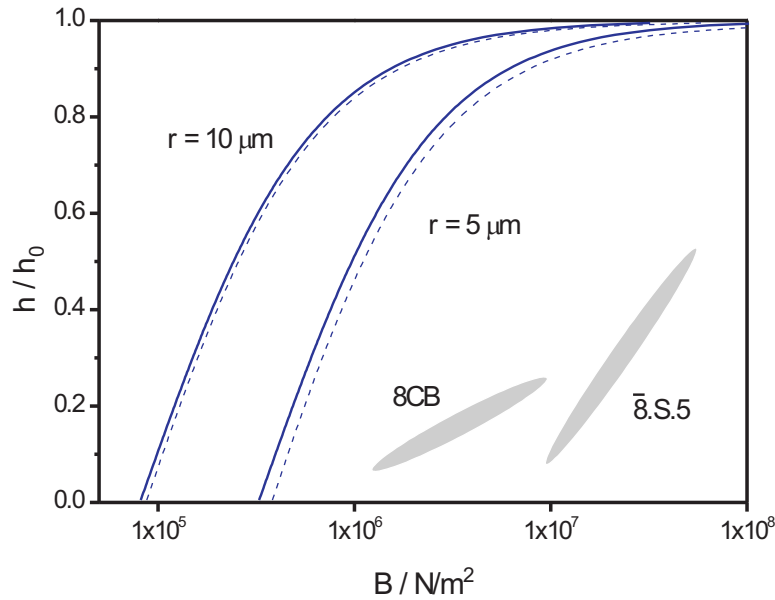


Figure 3.20: Solid lines: values of h/h_0 as function of modulus B , calculated using Equations 3.7 and 3.10 with $\sigma_{air} = 0.03$ N/m, $H = 45$ μm , and $r = 5$ μm or $r = 10$ μm . For the dashed lines, the intrinsic dilation sheath (see text) of the focal conic domains was additionally taken into account. Grey areas: experimental values of h/h_0 (this study) and B (determined with second sound measurements, from [38]) for the compounds 8CB and $\bar{8}.S.5$.

For most measurements of the absolute magnitude of B , the second sound technique [40] was used, which is based on a propagation mode supported by the smectic layers. These measurements are carried out in the kHz range, whereas our determination of h/h_0 is a purely static experiment. The frequency dependence of B at low frequencies has been studied in [41], where a pronounced decrease of B with decreasing frequency in the range from 10 Hz to 1 Hz was observed. Furthermore, it was shown that the dilation stress induced by a step-like strain relaxes almost completely with a time constant of ≈ 50 ms [42]. Thus, the static value of the modulus B could be orders of magnitude smaller than the values obtained from second

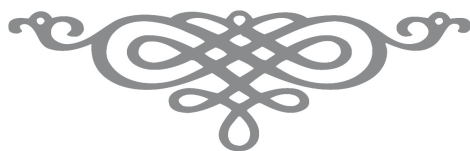
sound measurements. This might be the main reason for the discrepancy between the small B values resulting from my simple model and the larger values determined by second sound measurements.

In this chapter, the morphology and thermal behaviour of smectic liquid crystals on homogenous substrates were discussed. On such substrates as bare silicon wafers, and MAP coated silicon substrates, random planar anchoring at solid surface leads to circle focal conic domains with a straight line and an ellipse defect lines located in two planes perpendicular to each other. The diameter $2r$ of focal conic domains increases linearly with increasing the thickness H of smectic film. Moreover, the formation of focal conic domains are influenced by the strength of the planar anchoring of substrates. Through systematically varying anchoring strength by coating different silane layers consisting of the two silane compounds MAP and DMOAP, it was found that the slope of the $2r$ vs. H curve is depend on the anchoring strength of the substrate, and the magnitude of $\Delta\sigma_{sub}$ decreased linearly with increasing amount of DMOAP in the substrate coating. With quantitatively discussion, the planar anchoring strength of a smectic- A phase on a solid substrate can be determined.

Furthermore, the temperature dependence of h was studied. Close to the phase transition temperature, for the liquid crystal (e. g., 10CB) with smectic- A – isotropic transition, h exhibits a first-order transition, while for the liquid crystal (e. g., 8CB) with smectic- A – nematic transition, h appears a second-order transition. The ratio h/h_0 was used to how close an experimental depression (h) of a focal conic domain to the idealized incompressible depression (h_0). It is found that for compounds with a smectic- A – isotropic transition (10CB, 12CB, A7, and C7), h amounts to values relatively close to h_0 ; the compounds possessing a second-order smectic- A – nematic transition (8CB and $\bar{8}.S.5$) show considerably smaller values of h/h_0 . There is, however, no sharp boundary between these two groups of compounds. The study of a binary system of 8CB and 10CB shows that h/h_0 varies smoothly as one proceeds from second-order smectic- A – nematic transition over first-order smectic- A – nematic transition to smectic- A – isotropic systems. Above experimental observations may relate to the layer compressibility modulus B . A small value of B would allow for a dilation of the smectic layers in the central region of the focal conic domains, and thus result in a decrease of the value of h . This mechanism would qualitatively explain the decrease of h/h_0 on approaching a second-order smectic- A – nematic transition, and also the smaller values of h/h_0 in 8CB compared to the values of $\bar{8}.S.5$.

Through the investigation of absolute values of B of 8CB and $\bar{8}.S.5$, we found that the static value of B controlling the layer dilation in a focal conic domain is considerably smaller than the dynamic value.

Three of the compounds ($\bar{8}.S.5$, A7, and C7) with a smectic- C phase below their smectic- A phase were also investigated. In $\bar{8}.S.5$, h/h_0 decreases considerably at and below the transition to the smectic- C phase. In the other two compounds, A7 and C7, h/h_0 increases to ≈ 1 with decreasing temperature in the smectic- C phase. A reason for the different behaviours in the smectic- C phase might consist in the development of hexatic order, which was shown to increase the value of B considerably.



Chapter 4

Focal Conic Domains in Films on Patterned Substrates

“The only way of finding the limits of the possible is by going beyond them into the impossible.”

Arthur Charles Clarke (1917 – 2008): The Lost Worlds of 2001

In the previous chapter, I described smectic films on homogeneous substrates, i. e., the entire surface of the substrate possesses the same random planar anchoring condition. On these substrates, circular focal conic domains form either in a hexagonal two-dimensional lattice, or in a less regular order, in which a certain polydispersity in size presents.

A long-term goal of my study is to use focal conic domains to design new self-organizing micro- or nanosystems. For this purpose, it is critical to control the size and the arrangement of the focal conic domains on the substrate.

In this chapter, I will describe a method to fabricate almost arbitrary two-dimensional arrangements of focal conic domains in smectic films.

As discussed in Chapter 1, focal conic domains in smectic films are induced by antagonistic anchoring conditions at the interfaces, while no defects form if the film interfaces possess the same anchoring conditions. Since the liquid crystal/air interface always exhibits a strong homeotropic anchoring, the liquid crystal/substrate interface must possess a random planar anchoring condition in order to generate focal conic domains. Thus, a pattern of focal conic domains can be produced by a heterogeneous solid substrate with a pattern of homeotropic and planar anchoring conditions, i. e., some regions of the substrate surface should possess homeotropic anchoring conditions, while other regions exhibit planar anchoring conditions.

A possibility to create such an anchoring pattern is to coat some surface regions of a silicon wafer, which initially possesses random planar anchoring conditions on its entire surface, with a thin gold layer, which is known to induce homeotropic anchoring. The anchoring pattern of such heterogenous substrate may be used to control the position and the size of focal conic domains in smectic films.

The experimental procedures of the thermal evaporation of gold onto silicon substrates were described in Chapter 2. In order to fabricate different dimensions and arrangements of focal conic domains, two types of masks were used during the evaporation. The first consisted of small copper grids, with which line-, square-, or hexagon-like linear patterns were generated. The second type of mask is a monolayer of polystyrene microbeads, which generates circular patterns.

Smectic films of 8CB, 9CB, 10CB, 12CB and other liquid crystals were attempted on these patterned substrates. It was found that the method described above only worked for those compounds which possess a nematic phase above their smectic-*A* phase; i. e., for these compounds, such as 8CB and 9CB, the focal conic domains were confined in the patterns. However, for 10CB, 12CB, and other compounds, which transform directly from the isotropic to the smectic-*A* phase, a random planar anchoring was observed also in the gold-coated areas, and focal conic domains formed on the entire substrate surface. This may result from the mobility of focal conic domains formed at smectic-*A* – isotropic phase transition (discussed in Chapter 3). For this reason, in the following sections, I focus mainly on the behaviour of 8CB films on patterned substrates.

4.1 Behavior on Linearly Patterned Substrates

The linearly patterned substrates were prepared by evaporating gold onto a silicon substrate masked by a TEM grid. Dependent on the geometry of the grids, gold-coated square or hexagonal patterns were fabricated, which are separated by bare silicon stripes. The stripes are 10-60 μm in width (shown in Figure 4.1). As discussed above, the focal conic domains are expected to be restricted in the stripe areas, due to the different anchoring properties of gold and bare silicon regions. Figure 4.1 presents the optical pictures of the grids I used in the experiments, and corresponding AFM images of the silicon substrates patterned with gold. The dimension of the grid masks is listed in Table 4.1.

Figure 4.2 shows an optical micrography image, demonstrating that the arrays of focal

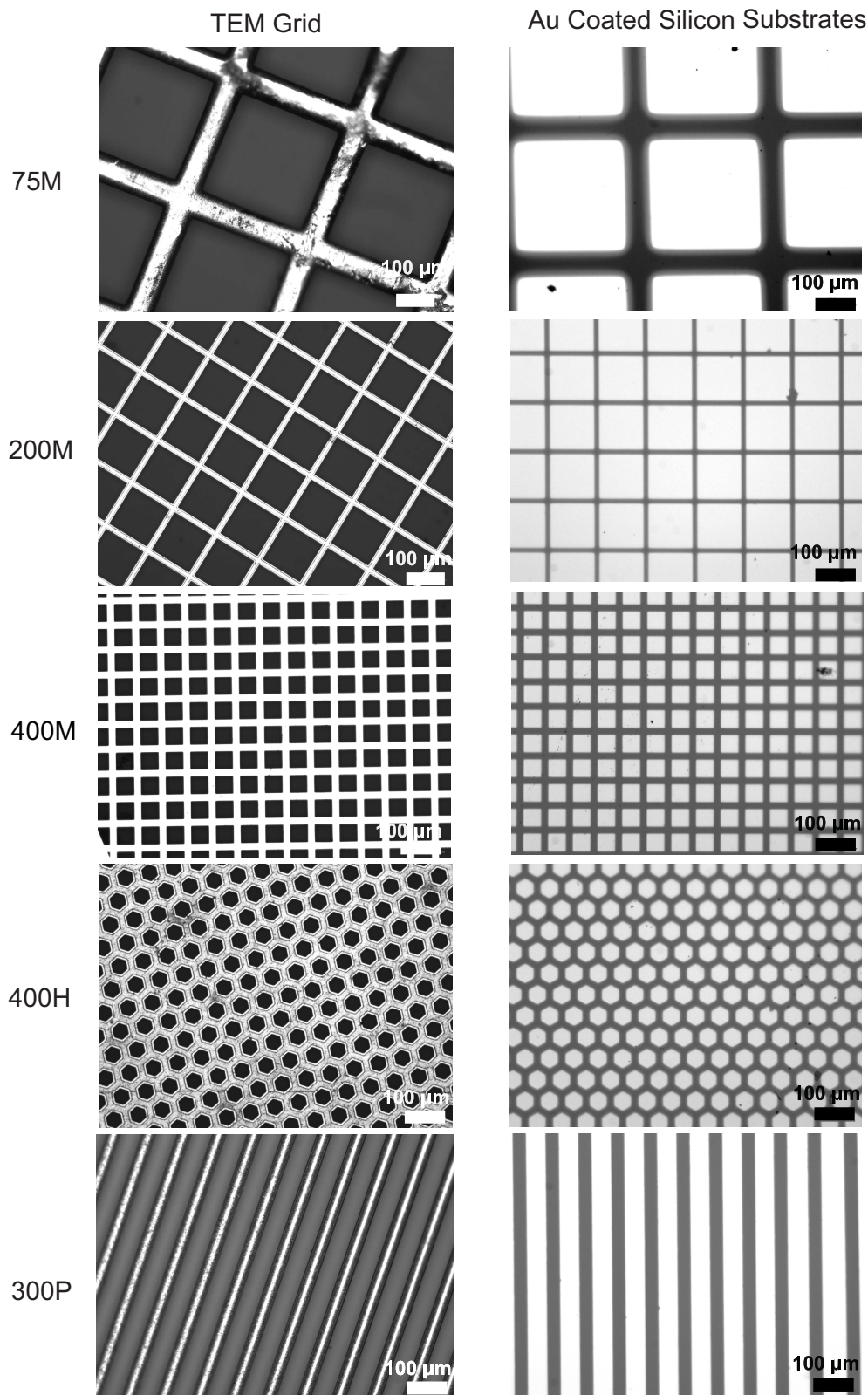


Figure 4.1: Optical microscopy images of grid masks (left) and corresponding gold coated silicon substrates (right).

Grid	Pattern	Width μm
75M	square	65
200M	square	14
400M	square	16
400H	hexagon	20
300P	linear	33

Table 4.1: The dimension of grid masks used in the experiments. The column ‘width’ refers to the width of the masked stripes.

conic domains follow the linear grid, even along the curved shape of the anchoring pattern, which was produced by a deformation of the grid mask.

Figure 4.3 presents AFM images of 8CB smectic films on the gold coated substrates patterned by different types of TEM grids listed in Table 4.1. Linear, square, and hexagonal arrays of focal conic domains were obtained.

Figure 4.4 shows the AFM image of a smectic 8CB film on a linearly patterned substrate, which possesses a square pattern with $12 \mu\text{m}$ wide stripes. It is obvious that the circular depressions are in a linearly array along the pattern, and each depression corresponds to a complete focal conic domain. The diameter of each focal conic domain is identified, and equal to the width of the stripe, except for the focal conic domain located at the center of the crossing, the diameter of which is larger and determined by the diagonal of the crossing, a factor of $\sqrt{2}$ larger than the stripe width. In Figure 4.4, the diameter of the focal conic domain at the center of the crossing is almost two times larger than that of the ones in the stripes. This is probably a result of the blunt edges of the gold coated patterns, so that the effective length of the diagonal of the crossing is larger than expected.

As discussed in Section 3.1, the diameter of focal conic domains increases as the thickness of the smectic film is increasing. On patterned substrates, due to the final dimension of the planar anchoring areas in the pattern, the maximum diameter of the focal conic domains depends on the width of the pattern stripes. When the film on a patterned substrate reaches a certain thickness H_0 , the diameter of the focal conic domains confined within the stripes coincides with the width of the stripes. When the film thickness is larger than H_0 , the equilibrium value of the focal conic domain diameter would be larger than the stripe width, but the real diameter of the focal conic domains on the patterned substrate is enforced to the value of the stripe width. Here, the term ‘equilibrium’ refers to the diameter of focal conic domains of a

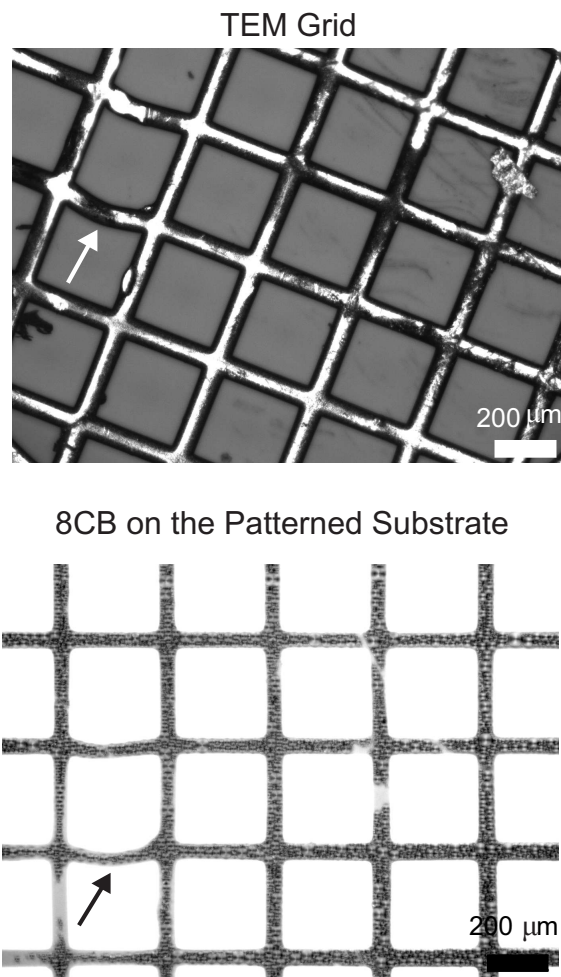


Figure 4.2: Top: the optical microscopy image of the TEM grid used to fabricate the pattern in the bottom image. Bottom: the optical microscopy image of 8CB focal conic domains on a patterned substrate produced by the top TEM grid. The arrows shown in top and bottom images indicate the same deformed curve in the produced pattern as in the grid. Focal conic domains are arrayed along this curve.

smectic 8CB film on a bare silicon substrate without any anchoring patterns.

In thinner films, where the equilibrium diameter of focal conic domains is smaller than the width of the stripes, multiple-row arrays of focal conic domains can be found. As shown in Figure 4.5, in $20\ \mu\text{m}$ wide stripes, 3-row, 2-row and 1-row arrays of focal conic domains were observed as the thickness of the film increased, and the multiple-row focal conic domains are arranged in a hexagonal pattern. Note that there are some tiny focal conic domains surround the big focal conic domains, as shown by blue arrows in Figure 4.5. In the thinnest film

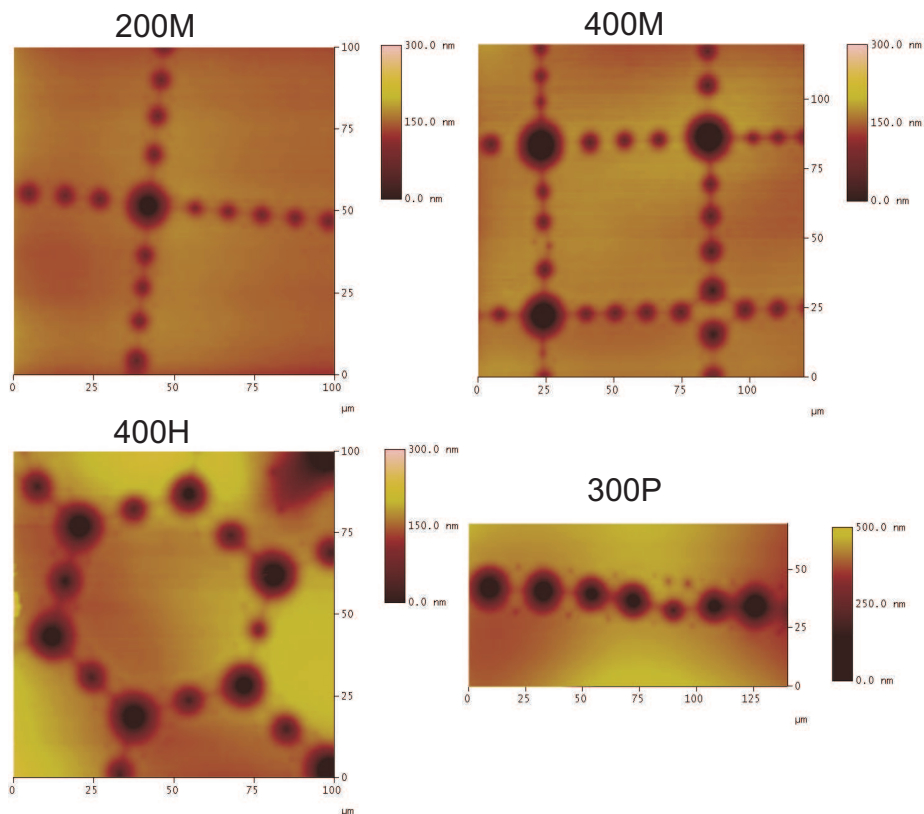


Figure 4.3: AFM image of a smectic 8CB film on patterned substrates with squares, hexagons or linear arrays of focal conic domains.

(in Figure 4.5, top), the shape of the surface depressions deviates clearly from the expected convex shape (comparable to the shape in the middle and bottom image), which also exists in very thin films of 8CB on bare silicon substrates without anchoring pattern.

The arrays of focal conic domains on the linear pattern are also clearly seen under the optical microscope and the fluorescence confocal microscope (Figure 4.6).

The arrangement of focal conic domains on patterned substrates is similar to the arrays produced by microchannels (see Chapter 1. The width of the microchannel plays a role similar to the width of the stripes on the patterned substrates. But in the case of microchannels, the anchoring of the wall of the channel also effects the arrangement of focal conic domains, which may impose incompletely focal conic domains.

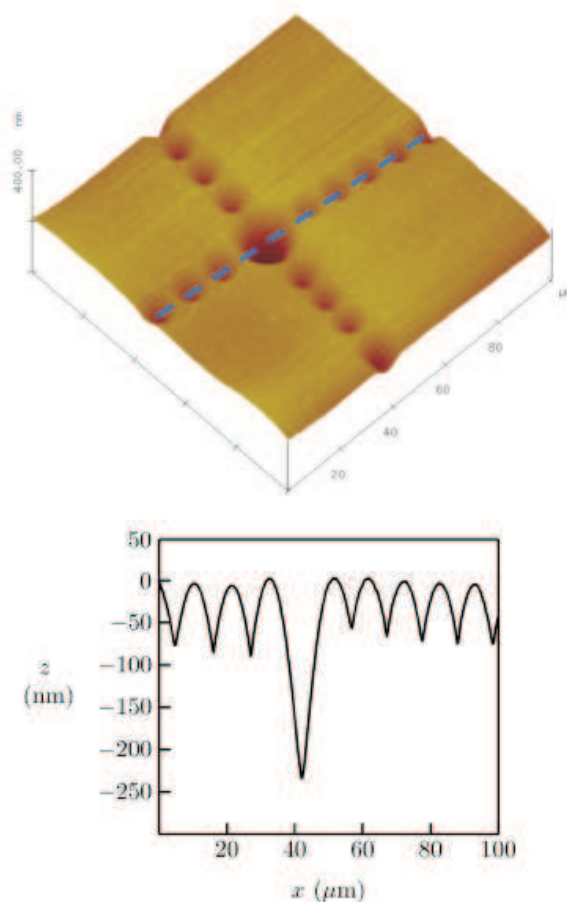


Figure 4.4: Top: AFM image of a smectic 8CB film on a silicon substrate patterned with gold-coated squares. The coated areas are separated by $12 \mu\text{m}$ wide bare silicon stripes. The image shows two stripes crossing. Bottom: cross section along the dashed blue line in the AFM image. Each depression at the interface is induced by an underlying focal conic domain.

4.2 Behavior on Circularly Patterned Substrates

Due to the dimensional limit of grid masks, the smallest confinement of focal conic domains created by grid patterns is of the order of $10 \mu\text{m}$. In order to apply smaller confinements to focal conic domains, the microbead masks were applied, consisting of a $0.5 \mu\text{m}$, $2 \mu\text{m}$, $6 \mu\text{m}$, or $10 \mu\text{m}$ diameter polystyrene microbead monolayer self-assembled on a silicon substrate. In the experiment, a large scale monolayer of microbeads can be fabricated by evaporating the microbead aqueous solvent under a low temperature. After thermally coating the masked substrate with gold, the microbead monolayer was transferred into water by floating the substrate

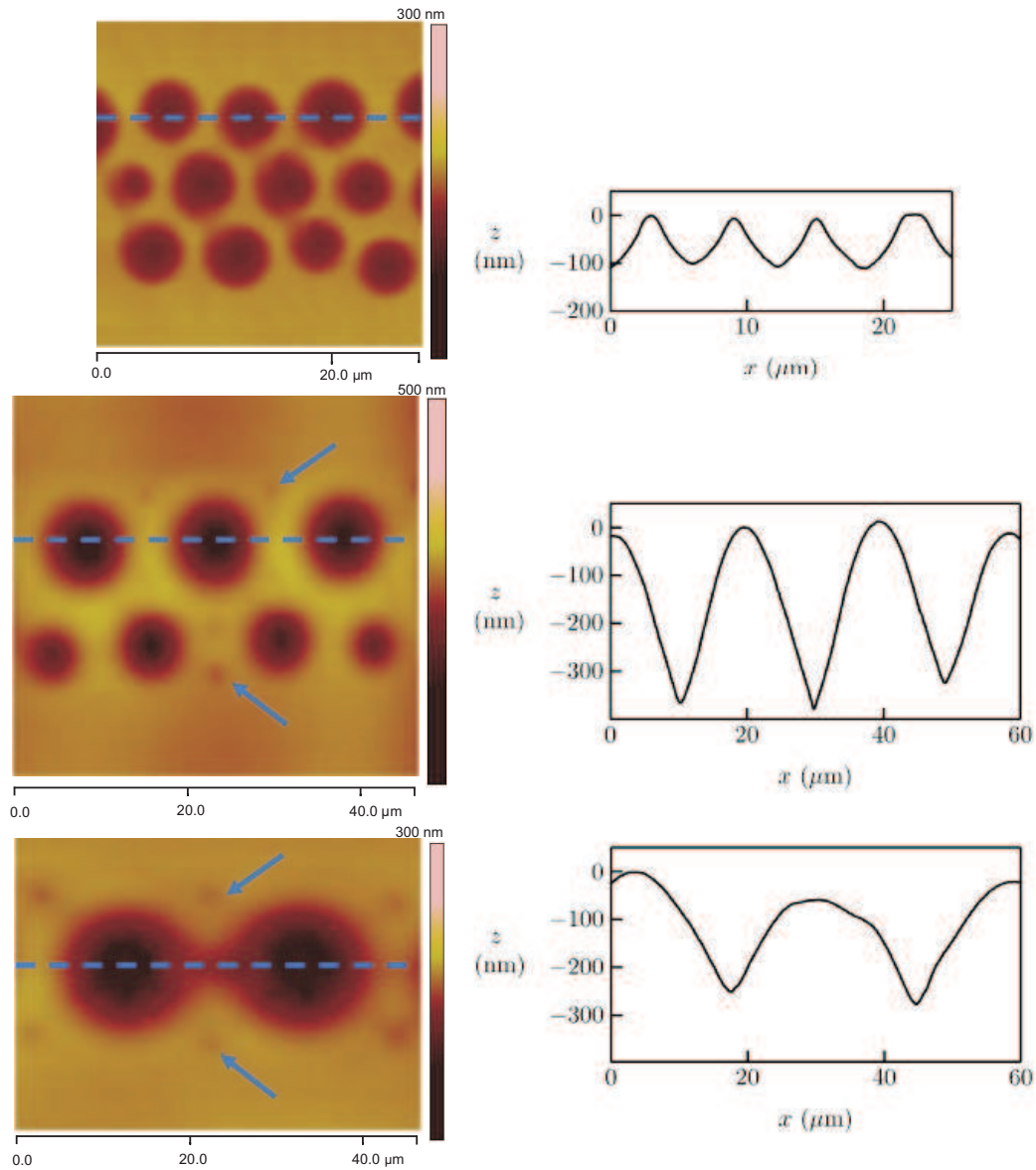


Figure 4.5: Left: AFM images of smectic 8CB films on gold coated silicon substrate with $20\ \mu\text{m}$ wide stripes of the bare silicon surface; The film thickness increases from $3\ \mu\text{m}$ (top) over $5\ \mu\text{m}$ (middle) to $15\ \mu\text{m}$ (bottom); the corresponding increase of the diameter of the focal conic domains results in the formation of 3-row, 2-row, and single-row arrays of focal conic domains. Note that free space in the stripe areas is sometimes filled with tiny satellite focal conic domains (middle and bottom image, indicated by the blue arrows). Right: cross sections along the dashed blue lines in each AFM image.

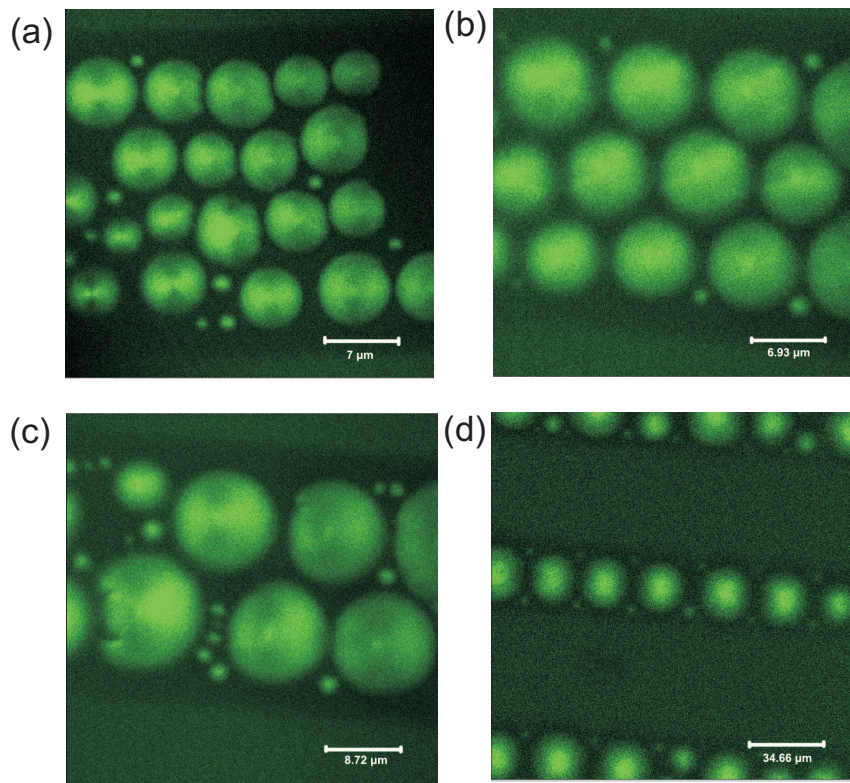


Figure 4.6: Fluorescence confocal microscopy images of smectic 8CB films on TEM patterned gold coated substrates. The thickness of the film is (a) $< 1 \mu\text{m}$, (b) $2 \mu\text{m}$, (c) $3 \mu\text{m}$, and (d) $> 18 \mu\text{m}$, and focal conic domains formed 4-row, 3-row, 2-row, and single-row arrays, respectively.

in a water reservoir. The patterns produced by different size microbead masks are shown in Figure 4.7 (left), in which the circular bare silicon areas arrange in a hexagonal lattice. The thickness of the gold film is about 60 nm. Figure 4.7 (right) presents the AFM images of 8CB smectic films on the patterned substrates corresponding to the left images. The thickness of the films was in a range where the equilibrium diameter of the focal conic domains was larger than the diameter of the circular patterns on the substrate. As shown in Figure 4.7, the actual diameter of the focal conic domains is the same as that of the circular patterns, i.e., the focal conic domains are confined by the substrate pattern. An exception is the pattern produced with the smallest ($0.5 \mu\text{m}$) microbeads, on which considerably larger focal conic domains were observed. A reason for this observation could be the poor quality of the patterns on the substrate, which contains many larger non-coated areas and open patterns with a bare silicon surface (probably caused by the presence of close-packed microbeads during the evaporation of gold).

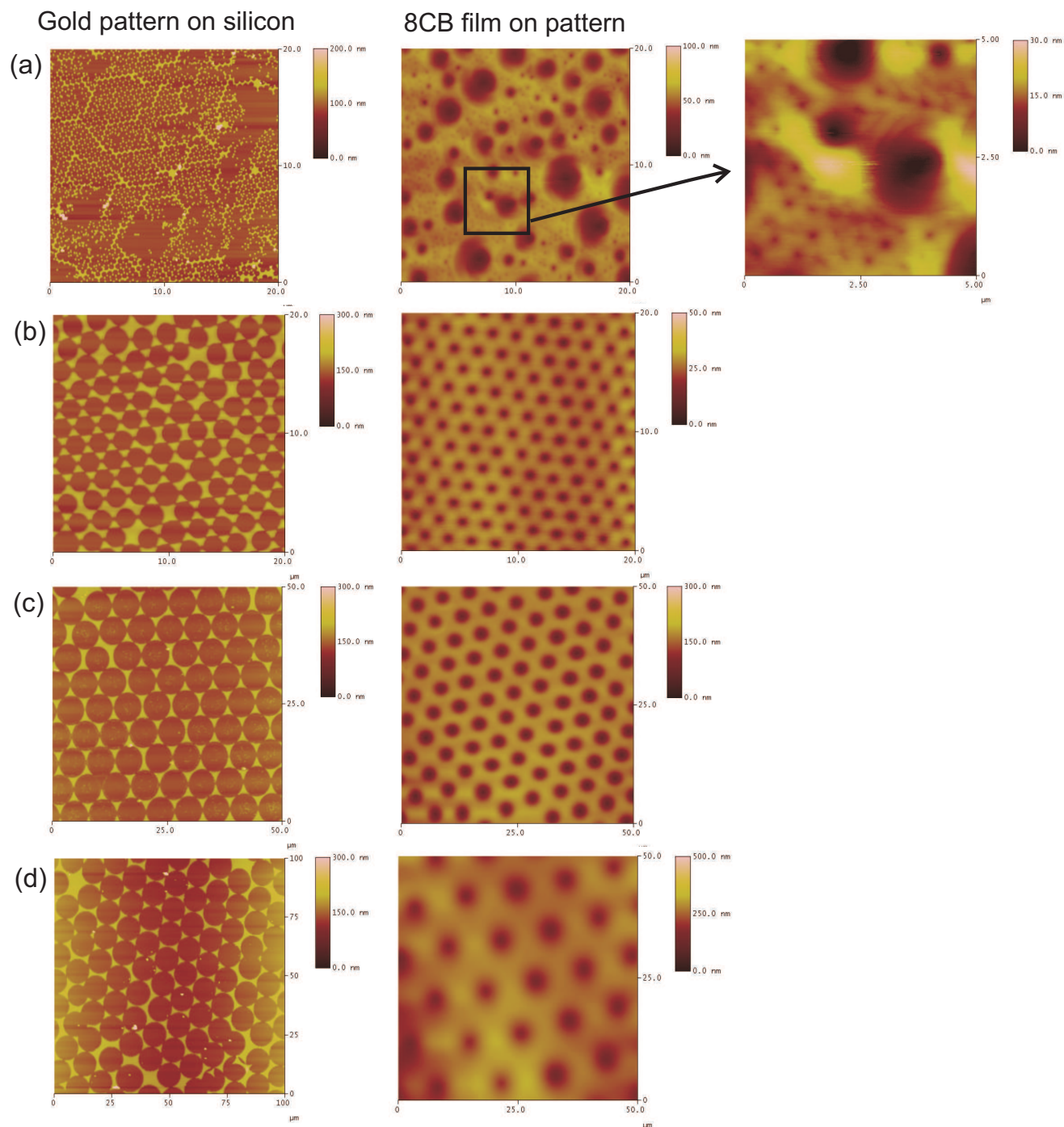


Figure 4.7: AFM images of gold patterns on silicon fabricated by microbead masks and 8CB film on such patterns. The size of microbeads used as masks is (a) 0.5, (b) 2, (c) 6, and (d) 10 μm . With the exception of the 0.5 μm case, the diameter of the focal conic domains is equal to the diameter of each circular pattern.

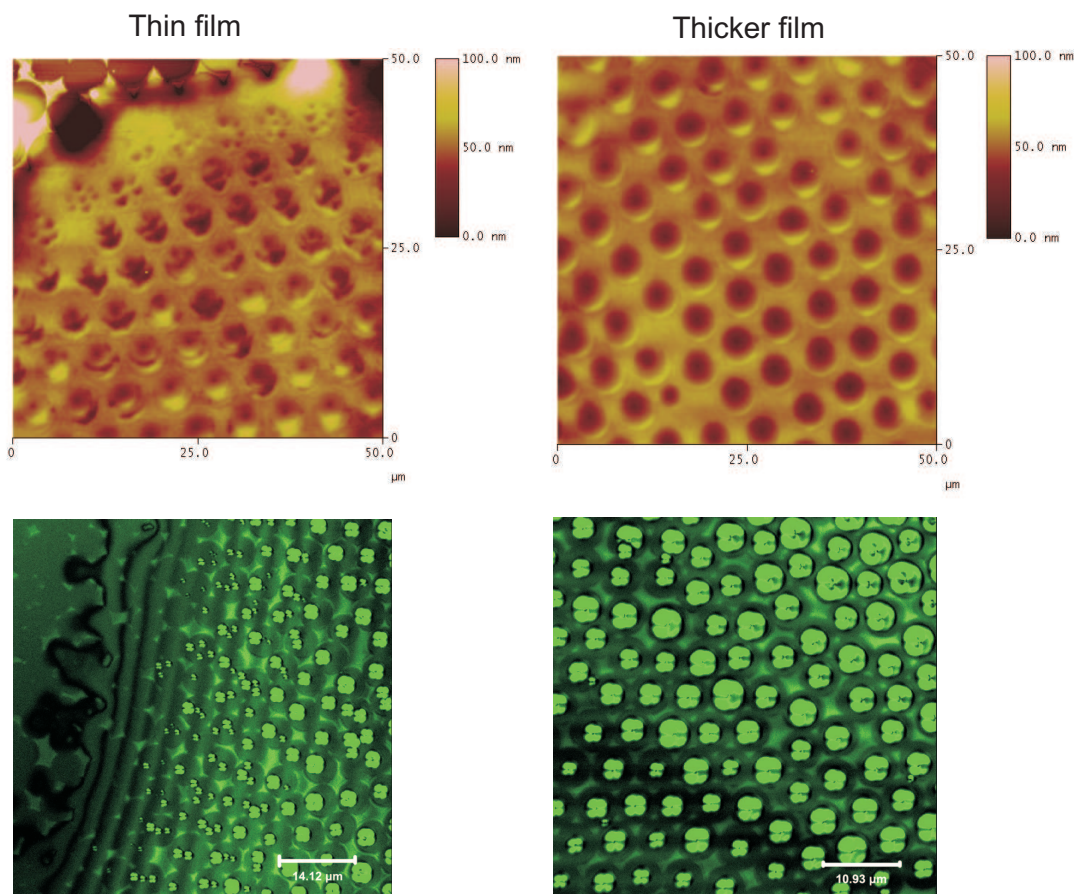


Figure 4.8: AFM images (top) and reflection confocal microscopy images (bottom) of 8CB smectic film on the patterned substrate fabricated by $6\ \mu\text{m}$ microbeads. The left image shows the region close to the film edge with the bare silicon at the left top corner. The right image shows a slightly thicker region of the same film. In thin film, several focal conic domains are restricted in one circular pattern. In the thicker film, one focal conic domain occupies one circular pattern, and the diameter remain as large as the circular pattern.

In thinner films, where the equilibrium diameter of focal conic domains is smaller than that of the pattern, several focal conic domains appear to fit into one circular pattern. Figure 4.8 shows an example of a 8CB smectic film on a patterned substrate with $6\ \mu\text{m}$ circular patterns. With increasing film thickness, seven, four, or two focal conic domains can form in one circle pattern, until the equilibrium diameter of the focal conic domain is large enough to hinder the formation of a second domain. In the thicker parts of the film, each focal conic domain occupies one circle pattern, and the diameter keeps a value of $6\ \mu\text{m}$, even when the thickness of the film amounts to $150\ \mu\text{m}$, for which the equilibrium diameter would be approximately

one order of magnitude larger than $6 \mu\text{m}$. This behaviour is illustrated in Figure 4.9.

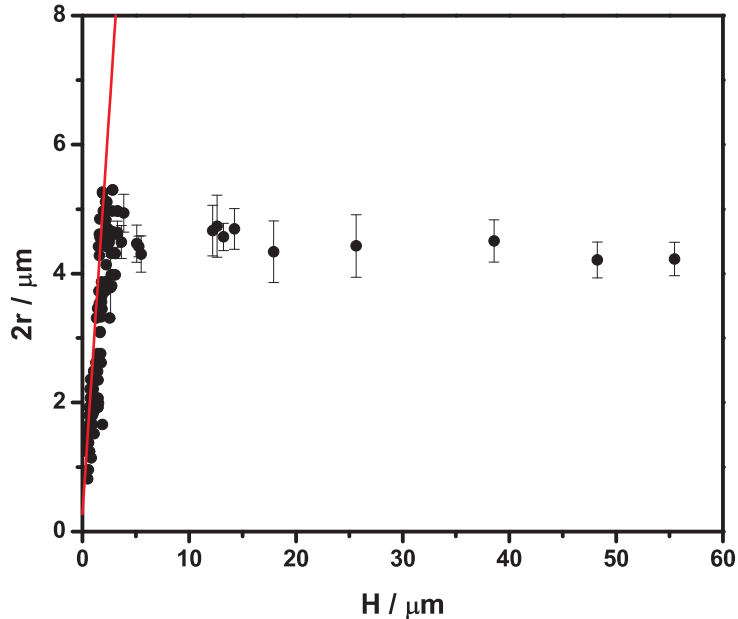


Figure 4.9: Diameter $2r$ of focal conic domains as function of film thickness H for 8CB films on the patterned substrate fabricated by $6 \mu\text{m}$ microbeads. The small dots are data taken from AFM measurements, data with bars at larger H values are from optical microscopy, the red line indicates the position of the data of 8CB on bare silicon substrates without anchoring pattern (see Figure 3.10).

On homogeneous substrates without anchoring pattern, the diameter of focal conic domains grows nearly linearly with the thickness of the smectic film (see Figure 3.10). However, on patterned substrates, the diameter $2r$ grows linearly only in the small film thickness region, but stays constant with increasing thickness when the domain diameter becomes comparable to the diameter of the circular bare silicon regions.

Reflection confocal microscopy verified this result. In Figure 4.8 (bottom), several focal conic domains were observed in one circular pattern in the thin film, while in the thicker film, only one focal conic domain occupied each circular pattern, and in very thick films the focal conic domains were still confined in the circular patterns.

Similar results were also found on the $2 \mu\text{m}$ and $10 \mu\text{m}$ microbead patterned substrates.

Fluorescence confocal microscopy provided images of the cross sections of focal conic domains on patterned substrates. In Figure 4.10, the focal conic domains are arranged in a hexagonal pattern, and the x - z cross sections of single focal conic domains, which fully

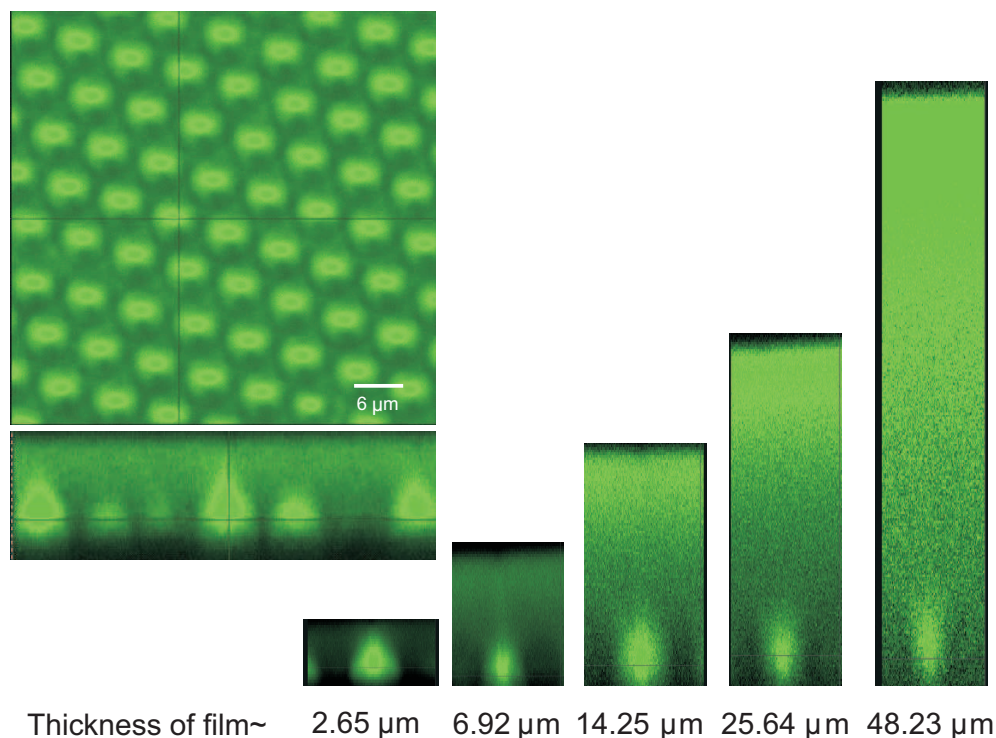


Figure 4.10: Fluorescence confocal microscopy image of 8CB smectic film on the patterned substrate fabricated by $6\ \mu\text{m}$ microbeads. The left top image presents a hexagonal array of focal conic domains. And a series images at the right bottom shows the cross section of a single focal conic domain in films with different thickness.

occupied one circular pattern, at different thickness were recorded. The fluorescence confocal microscopy images indicate that the structure of the focal conic domains near the substrate does not change with the thickness of the film, implying that the increase of the thickness simply results in the addition of smectic layers near the air interface without influencing the layer's arrangement near the solid substrate.

Circularly patterned substrates offer thus a simple way to fabricate a uniform, controllable, and large scale hexagonal arrangements of focal conic domains regardless of the film thickness.

4.3 Behavior of The Surface Depressions in Thick Films on Patterned Substrates

The results presented in the preceding sections show that on patterned substrates, as long as the thickness of smectic film exceeds a certain value, the size of focal conic domains is determined by the dimension of the pattern, i. e., by the width of the stripes or the diameter of the circular patterns. Therefore, the diameter of focal conic domains remains constant even if the film thickness increases. What is the behaviour of the depth h of the domain-induced surface depressions for such patterned substrates? I assume for the moment, that the structure of focal conic domains corresponds to the idealized geometric scheme shown in Figure 3.13 and recall Equation 3.5 which describes the relation between h , the film thickness H , and the domain radius r :

$$h = H - \sqrt{H^2 - r^2} \quad (4.1)$$

According to the above Equation, h should decrease with increasing thickness H , if r stays constant.

Figure 4.11 shows experimental values of h , measured by AFM, in films with different thickness H , determined by confocal microscopy, on the $6 \mu\text{m}$ microbead patterned substrates. The observed decrease of h with increasing H confirms qualitatively the expected behaviour. Quantitatively, however, the values predicted by Equation 4.1 (which are indicated by the black line in Figure 4.11), are considerably larger than measured h values. This behaviour corresponds to the results observed on homogeneous substrates (see Section 3.2.2). For 8CB at room temperature, the measured value of h amounts to only $\approx 1/3$ of value calculated by Equation 4.1. The probable reason of this behaviour is a dilation of the smectic layers in the central region of the focal conic domains leading to a decrease of h .

I have applied the same simple model used in Section 3.2.2 to the data shown in Figure 4.11. In this model, the energy Δw_{dil} , which is to be paid for the dilation of the smectic layers, is balanced against the energy Δw_{surf} , which is gained by the decrease of the area of the free surface above the focal conic domain. Recalling Equations 3.7 and 3.10, these two energies are given by

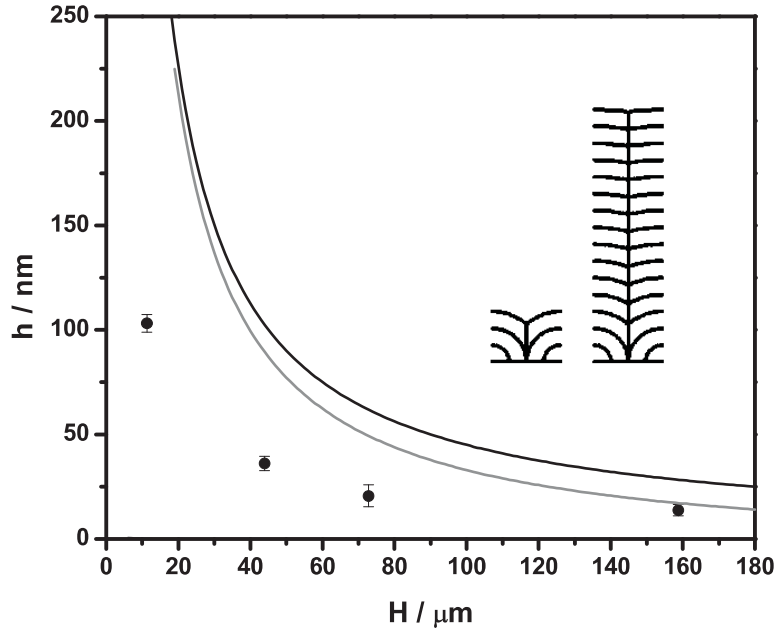


Figure 4.11: Depth h of the surface depressions induced by focal conic domains as a function of thickness H of films on a circularly patterned substrate prepared with $6 \mu\text{m}$ polystyrene microbead monolayer. Solid dots: experimental values determined by AFM; black line: calculated values according to Equation 4.1 with $r = 3 \mu\text{m}$; grey line: calculated values according to Equations 4.2 and 4.3 with $r = 3 \mu\text{m}$, $\sigma_{air} = 30 \text{ mN/m}$, $B = 1.3 \times 10^7 \text{ N/m}^2$, and $h_0 = H - \sqrt{H^2 - r^2}$.

$$\Delta w_{surf} = \sigma_{air} \pi r \left(\sqrt{r^2 + h^2} - \sqrt{r^2 + h_0^2} \right) \quad (4.2)$$

$$\Delta w_{dil} = \frac{\pi B (h_0 - h)^2 r^2}{12H}. \quad (4.3)$$

Here, h_0 is the depth of the surface depression calculated by Equation 4.1, h is the real depth, r the domain radius, H the film thickness, and B the smectic layer compression/dilation modulus. For 8CB, the value of B at room temperature amounts to $1.3 \times 10^7 \text{ N/m}^2$. If one calculates h as a function of H using this B value and the above equations, the grey line in Figure 4.11 is obtained which is only a minor improvement compared to the pure geometric model (Equation 4.1). As discussed in Section 3.2.2, this result indicates that the model given by Equations 4.2 and (4.3) is too simple for an adequate description of the experimental behaviour. However, the results presented in this section demonstrate that on circularly pat-

terned substrates the depth of the domain-induced surface depressions can be controlled by the variation of the film thickness.

I have also studied the temperature dependence of h in films on patterned substrates. For 8CB films on homogeneous substrates, h decreases continuously to zero when the second-order transition to the nematic phase temperature is approached (see Section 3.2.2). A similar behaviour is also observed on circularly patterned substrates, provided that the diameter of the focal conic domains on the patterned substrates is smaller than, or equal to that of the circular pattern. However, in thick films, where there is a large difference between the equilibrium diameter corresponding to the film thickness and the experimental diameter, h behaves almost independent of temperature (Figure 4.12). There is no obvious reason for this thickness dependence of the thermal behaviour and further experimental studies are needed.

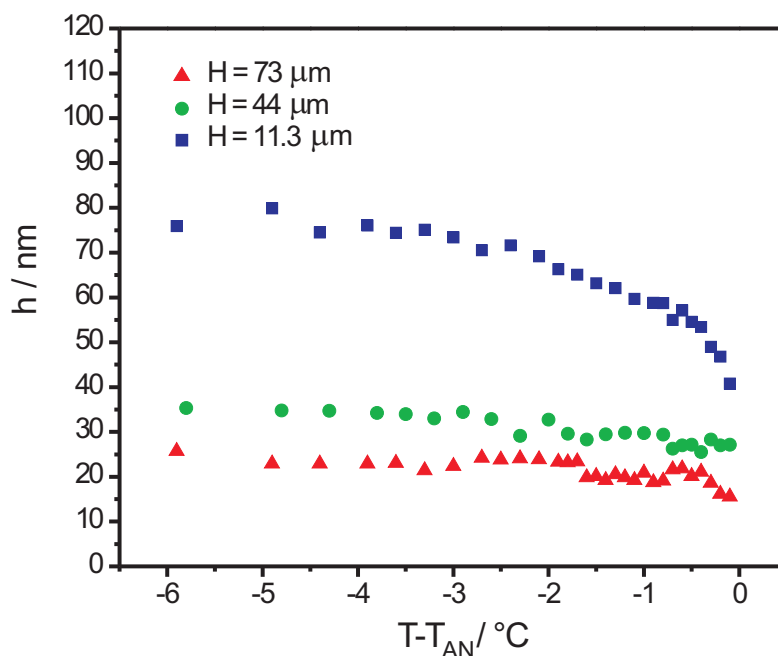
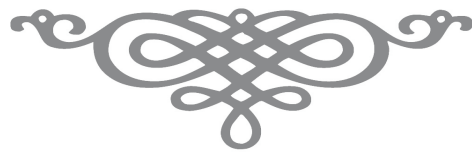


Figure 4.12: Temperature dependence of the depth h of the domain-induced surface depressions in films on substrates with $6 \mu\text{m}$ circular anchoring patterns. The thickness of the films amounts to $11.3 \mu\text{m}$, $44 \mu\text{m}$, and $73 \mu\text{m}$. T_{AN} designates the smectic- A – nematic transition temperature of 8CB.

In this chapter, the behaviour of focal conic domains on substrates with anchoring patterns was discussed. On these substrates, regions possessing random planar anchoring conditions

4.3. Behavior of The Surface Depressions in Thick Films on Patterned Substrates 107

alternate with regions possessing homeotropic anchoring conditions. If smectic films are prepared on such substrates, the formation of focal conic domains is restricted to the regions possessing random planar anchoring conditions. In thin films, the dimension and thermal behaviour of focal conic domains are similar to that on homogeneous substrates (discussed in Chapter 3). In thick films, confinement effects were observed, because the diameter of the focal conic domains cannot grow beyond the dimension of the planar anchoring regions on the substrate. Thus, substrates with anchoring patterns offer a possibility to control both the arrangement and the dimensions of focal conic domains in smectic films.



Chapter 5

Structure Formation in Smectic Films on Crystalline Substrates

“The wealth of the mind is the only true wealth.”

In the previous chapters, the morphology and thermal behaviours of focal conic domains on substrates with random planar anchoring were discussed. On a substrate with random planar anchoring, the liquid crystal molecules prefer to align parallel to the substrate plane, but there is no preferred in-plane direction for the orientation of the long molecular axes. The circular base of the focal conic domains in films on such substrates is a direct consequence of the absence of a preferred in-plane orientation.

In this chapter, I present preliminary results obtained for smectic films prepared on the surface of freshly cleaved layered crystals, mica and MoS₂. Different from the alignment on bare or coated silicon substrates, the crystalline structure of the surface results in the alignment of the liquid crystal molecules along one or several preferred in-plane directions. Instead of circular focal conic domains, linear defect structures are expected on such substrates.

A simple model of these linear structures is shown in Figure 5.1. At the substrate surface, all liquid crystal molecules are aligned parallel to the surface and point into one direction. The smectic layer planes are oriented perpendicular to the surface and perpendicular to the direction of the long molecular axes. However, because of the homeotropic anchoring at the air interface, the layer planes have to bend and form a system of concentric hemicylinders. Along the central axis of these hemicylinders, a straight singular line is running on the substrate surface. If the film thickness is larger than half of the distance between two neighboring singular lines, the outer layers near the air interface cannot form complete hemicylinders be-

cause they end at singular planes separating neighboring structural domains. The air interface on top of these linear structures should exhibit a kind of corrugated shape. As is described in the following, such structures are indeed observed experimentally, at least in the range of smaller film thicknesses.

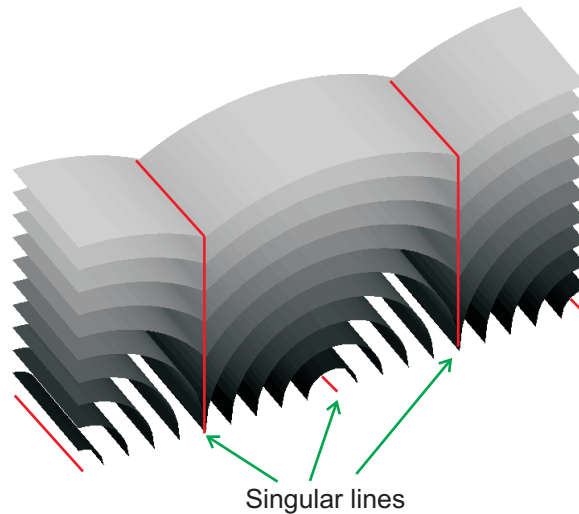


Figure 5.1: Hemicylinder scheme of the linear defect structures in a smectic film on a substrate with unidirectional planar anchoring.

5.1 Smectic Liquid Crystal Films on Mica Substrates

Muscovite mica is a phyllosilicate mineral of aluminium and potassium with a monoclinic structure. Because of its monocrystalline layered structure, it can easily be cleaved to get an atomically smooth surface, which is widely used as a substrate for AFM studies [125], or for binding cells to be characterized by transmission electron microscopy [126], etc..

The crystal structure of mica can be seen as an alternating stack of two different layers, L_α and L_β . When mica is cleaved, two types of surfaces can be obtained, depending on whether the cleavage was done at a α/β or a β/α interface. Both types of interfaces induce a monostable planar anchoring, i. e., there is a single preferred direction of the liquid crystal molecules on the surface. Comparing the orientation of this preferred direction for the two different surfaces (α/β and β/α), one observes an angle of 120° between them [53, 127]. If mica is cleaved

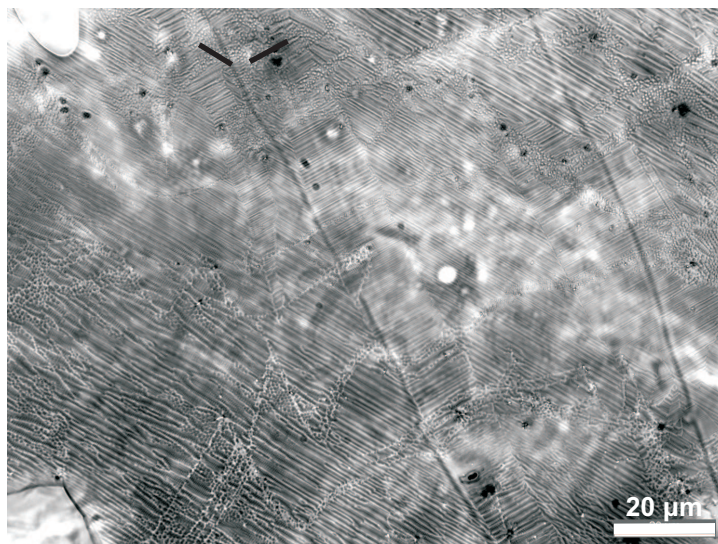


Figure 5.2: Optical microscopy image of a thin 8CB film on mica at room temperature. The black lines indicate the directions of linear defects.

simply by hand, one obtains substrates which usually contain both types of surfaces, separated by monolayer steps. Therefore, when a thin 8CB film is prepared on mica and cooled down to room temperature, two orientations of linear defect structures are observed and the angle between the defect lines amounts to 120° (Figure 5.2).

In thicker films of 8CB, circular focal conic domains are formed, and arrange themselves in a hexagonal lattice. Figure 5.3 shows a droplet of 8CB placed on mica. Near the edge of droplet, where the local film thickness is small, the linear structures are observed, while beyond a certain thickness, circular focal conic domains, similar to those obtained on silicon substrates, are formed. Figure 5.4 shows AFM images presenting the topography of the linear structures and the circular focal conic domains on mica.

In the transition region between the regions with linear structures and circular focal conic domains, more complicated defect structures are observed (shown in Figure 5.5). Between two linear structures, a kind of corrugated pattern appears. With increasing thickness of the liquid crystal film, the distance between the linear defects gets larger and the corrugated pattern becomes more pronounced, and finally ends with the formation of circular conic domains.

However, 8CB shows a large contact angle on mica, and it is difficult to obtain a thin film of 8CB on it. To study the phenomena described above in more details and in order to get a more quantitative relation between the thickness of the liquid crystal film and the defect

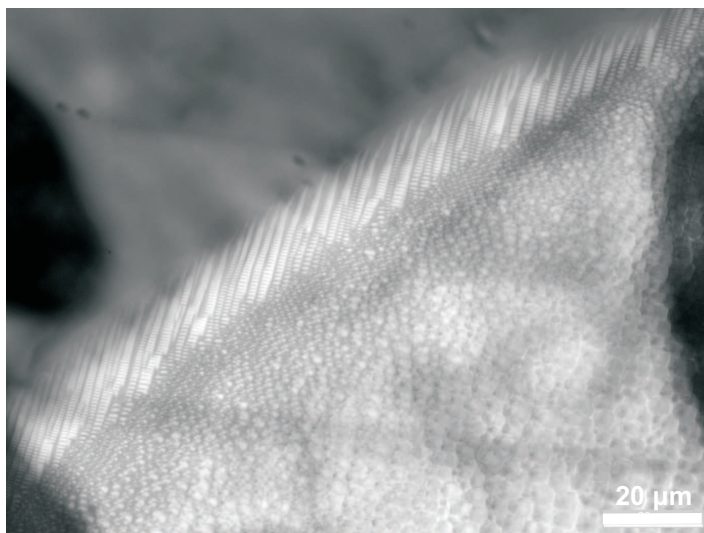


Figure 5.3: Optical microscopy image of a droplet of 8CB on mica at room temperature. Near the edge of the droplet (running from the lower left to the upper right corner) linear structures are present while in the thicker regions circular focal conic domains are forming.

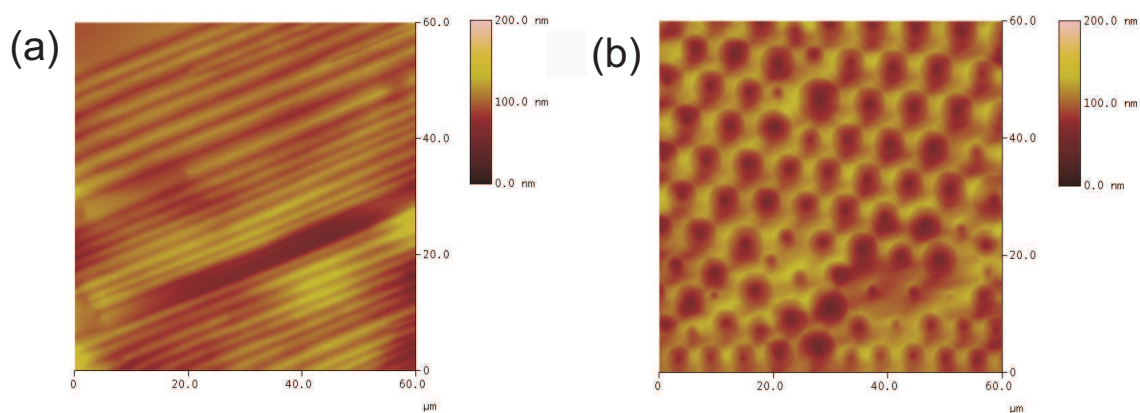


Figure 5.4: AFM images of an 8CB droplet on mica at room temperature (a) near the edge of the droplet, and (b) near the center of the droplet.

structure morphology, I found it more useful to use MoS_2 crystals as substrates, which are wetted completely by alkylnobiphenyl liquid crystals so that thin films can be prepared more easily.

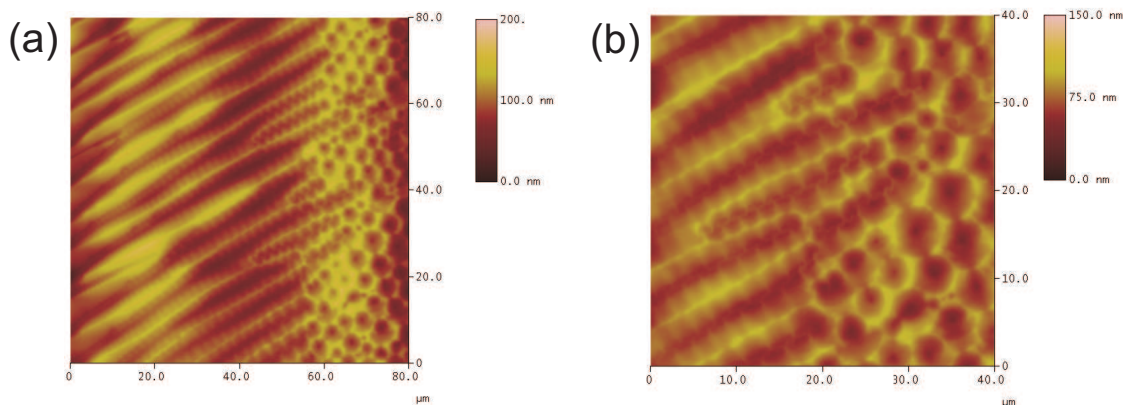


Figure 5.5: AFM images of an 8CB droplet on mica at room temperature. (a) shows the region between linear structures and circular focal conic domains. (b) gives a detail image of (a).

5.2 Smectic Liquid Crystal Films on MoS₂ Substrates

Molybdenum disulfide, MoS₂, is a natural single crystal with a layered structure which can easily be cleaved. One obtains a surface with sulfur atoms on a two-dimensional hexagonal lattice. Alkylcyanobiphenyl liquid crystals show on this surface a planar anchoring with six different preferred in-plane orientations. The angle between these orientations amounts either to 35° or 25° (see Chapter 1.4.1).

In my experiments, 8CB was placed on a freshly cleaved MoS₂ surface, heated up to 42°C, and then cooled down with a rate of 0.1°/min to room temperature, so that a film of 8CB spread on the MoS₂ substrate. Figure 5.6 and Figure 5.7 are the typical optical microscopy and AFM images of 8CB films on MoS₂ substrates. Unlike on mica, a strong multistable planar anchoring is imposed to the smectic-A 8CB phase on MoS₂. The six different in-plane orientations of the linear structures are indicated by the six different color lines in Figure 5.7. The AFM images show, that the different anchoring direction domains are separated by sharp boundaries.

5.2.1 Film Thickness Dependence of The Linear Structures on MoS₂ Substrates

The 8CB films prepared on MoS₂ substrates are very thin (below $\approx 1.5 \mu\text{m}$) so that confocal microscopy measurements cannot be used for the determination of the film thickness. Since

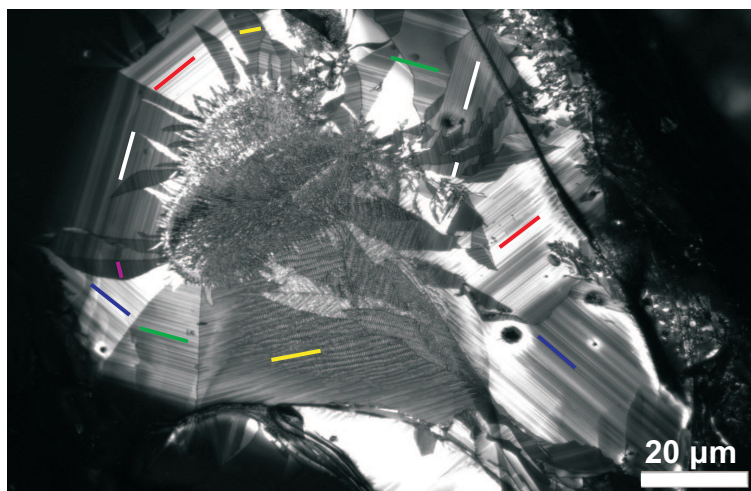


Figure 5.6: Optical microscopy image of a 8CB film on MoS₂ at room temperature. Different color lines represent the six different in-plane orientations of the linear structures.

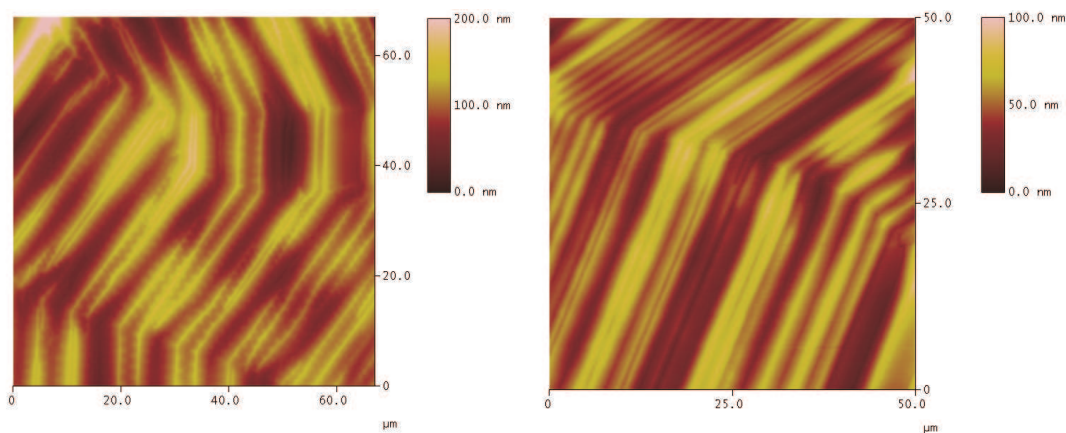


Figure 5.7: AFM images of a 8CB film on MoS₂ at room temperature. The different anchoring direction domains are separated by sharp boundaries.

the films spread over almost the entire substrate surface, the use of AFM measurements for the thickness determination is also not possible. Therefore, I estimated the film thickness with the help of the interference colors which are shown by the samples. This method is established for freely suspended smectic films [128], but here I assume that the film thickness difference corresponding to one color sequence (or one interference order) amounts to ≈ 200 nm. Figure 5.8 shows several AFM images of smectic 8CB films on MoS₂, demonstrating

how the observed linear defect structures change with increasing film thickness.

In very thin films (below 200 nm), a homogeneous film without any defect structures is obtained on MoS₂ (Figure 5.8 (a)). In slightly thicker films (Figure 5.8 (b) and (c)), there appear parallel lines which indicate the presence of the hemicylinder structures shown in Figure 5.1. As the film thickness increases further, additional features appear: the parallel structures are not smooth any longer, since ripples in the perpendicular direction are forming (Figure 5.8 (d)-(g)). These structures will be discussed in the following section. Beyond a certain thickness, circular focal conic domains are found (Figure 5.8 (h)).

The distance between neighboring hemicylinder domains and the depth of linear depressions in the air interface are comparable with the diameter and the surface depression depth of the circular focal conic domains. Similar to the case of the circular focal conic domains, the distance between linear structures, as well as the depth of linear depressions, grow linearly as increasing film thickness (Figure 5.9). This applies also to the thicker film in which the basic hemicylinder structures are patterned with additional structural features (≈ 400 nm to ≈ 1000 nm; at larger film thicknesses, circular focal conic domains are formed).

The temperature dependence of the depth h of the linear surface depressions was also checked. Figure 5.10 shows h as a function of temperature for a smectic 8CB film on MoS₂. Similar to the case of circular focal conic domains of 8CB (or other compounds with a second-order smectic-A – nematic transition), h decreases as the transition to the nematic phase is approached. However, close to the phase transition temperature, the defects become unstable, so that the h of the linear surface depression can not be measured any more.

A more detailed analysis of the relation between the distance of neighboring hemicylinder structures, the depth of the linear surface depressions, and the thickness of the smectic film would require an accurate determination of the film thickness, which is beyond the scope of this thesis.

5.2.2 Fluorescence Confocal Microscopy of Smectic Liquid Crystal Films on MoS₂ Substrates

To gain more insight into the structure of the complex structural patterns which appear in the thickness range between the smooth hemicylinder structures at small thicknesses and the circular focal conic domains at larger thicknesses, polarized fluorescence confocal microscopy studies of smectic 8CB films on MoS₂ substrates were conducted. As described in Chapter 2, the liquid crystal was doped with a tiny amount of the dye BTBP before the film was prepared

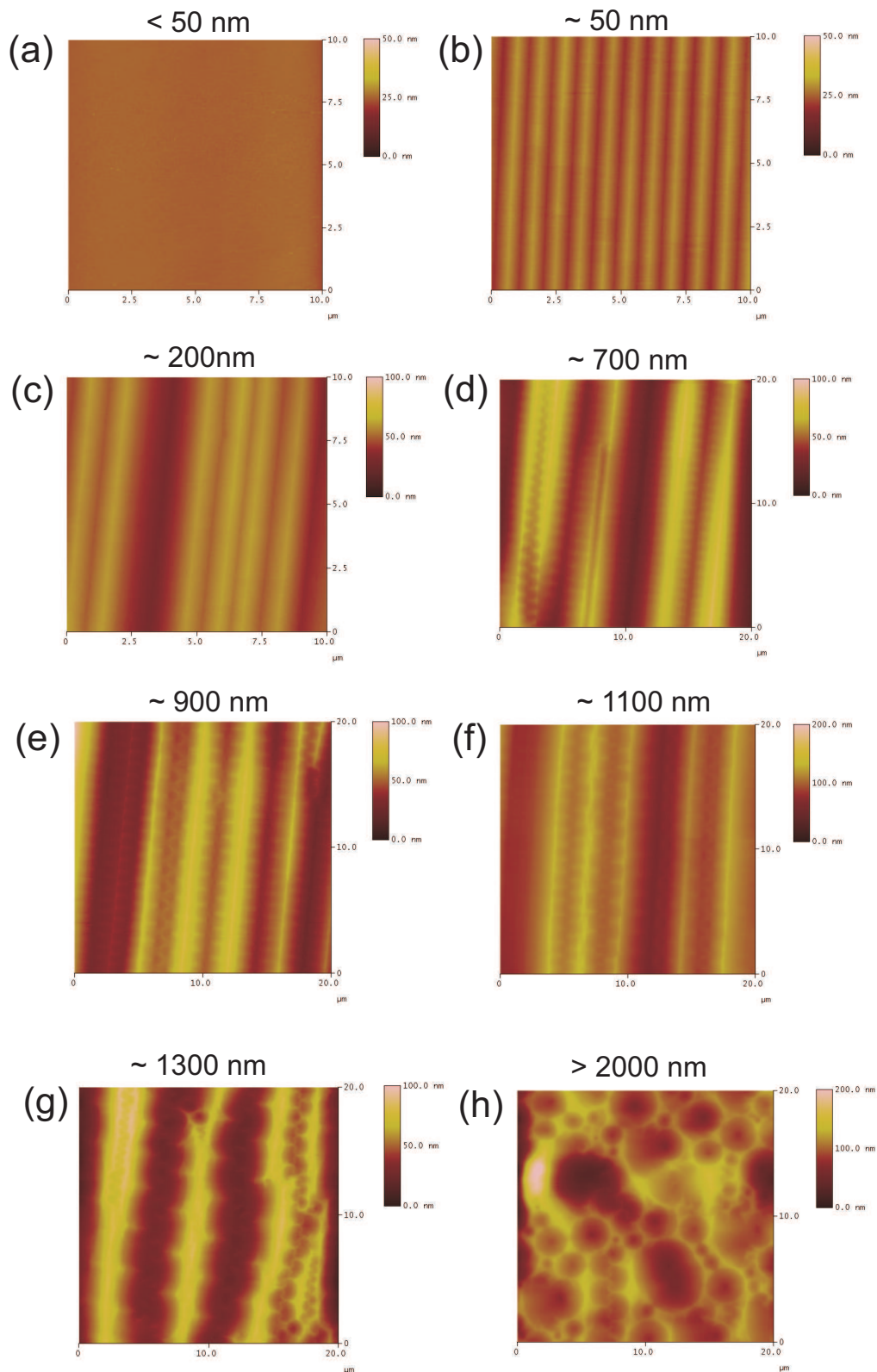


Figure 5.8: AFM images of smectic 8CB films on MoS₂ for different film thicknesses. The thickness, estimated by the interference colors of the scanning areas, are respectively (a) < 50 nm, (b) ~ 50 nm, (c) ~ 200 nm, (d) ~ 700 nm, (e) ~ 900 nm, (f) ~ 1100 nm, (g) ~ 1300 nm, and (h) > 2000 nm.

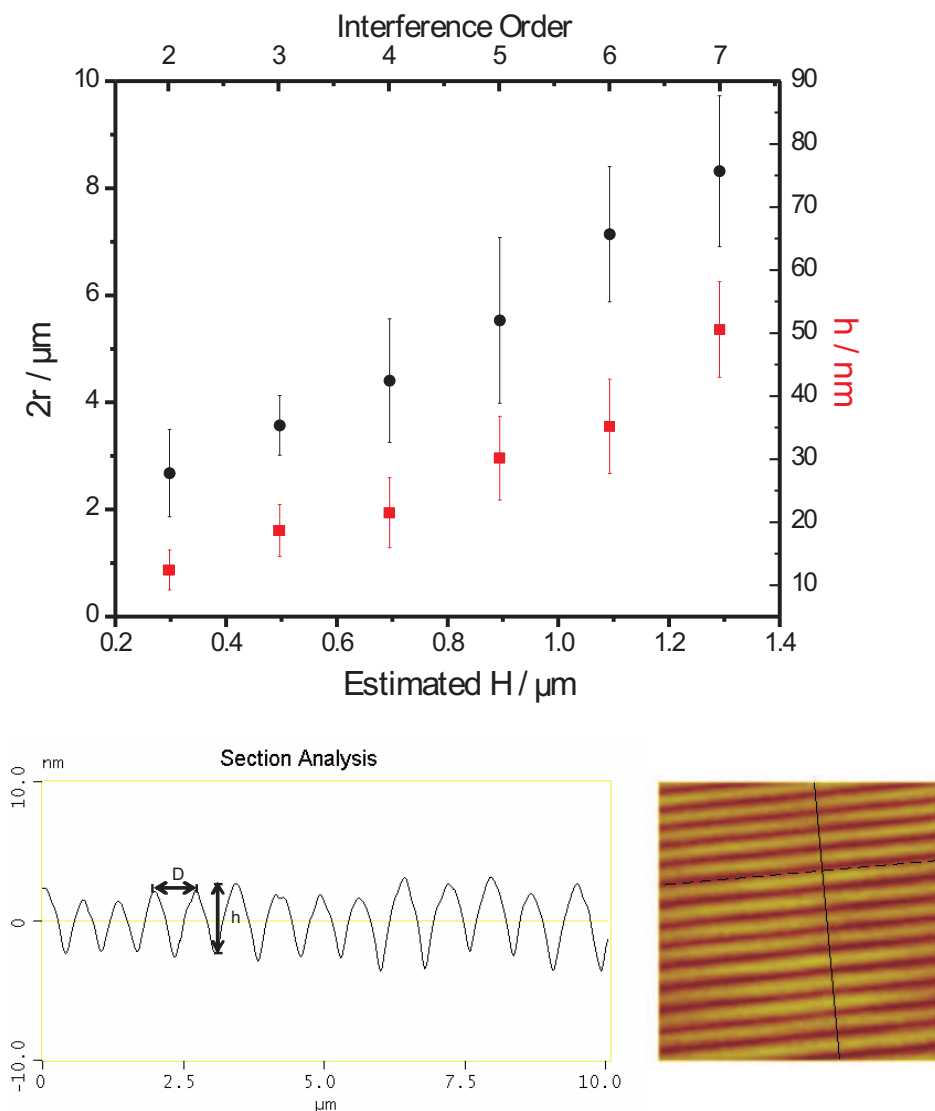


Figure 5.9: Distance between neighboring hemicylinder domains and depth of the linear surface depressions as function the film thickness (8CB at room temperature). The thickness was estimated by the inference color of the film. The bottom AFM image depicts the distance D and depth h of the linear structures.

on the MoS₂ substrate.

Figure 5.11 shows polarized fluorescence confocal microscopy images of different thickness areas and the corresponding AFM images. The fluorescence exciting laser light was linearly polarized in the direction parallel to the horizontal edges of the images. The intensity of the fluorescent light indicates the orientation of the liquid crystal molecules (because the

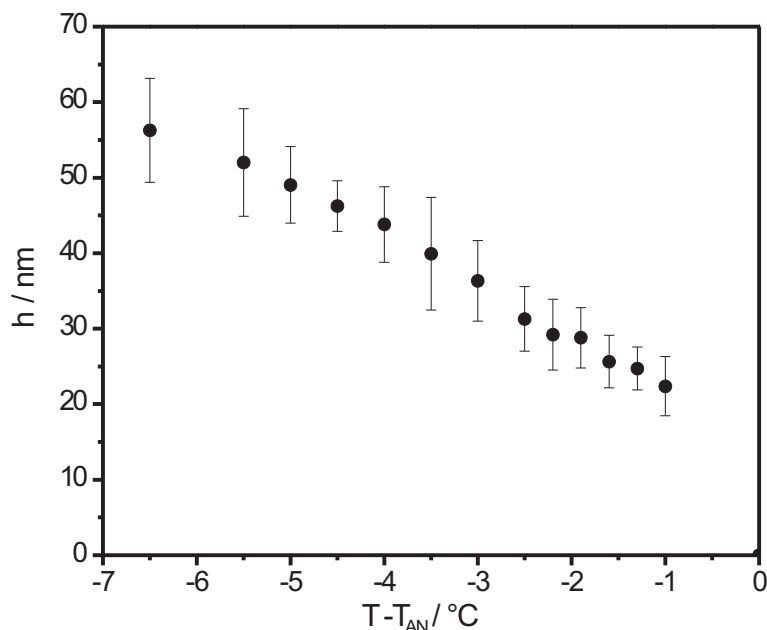


Figure 5.10: Temperature dependence of the depth h of the linear surface depressions of a smectic 8CB film on MoS_2 .

fluorescent dye align parallel to the liquid molecules): the intensity is at a maximum, when the liquid crystal molecules are parallel to the plane of polarization and to the substrate plane. The fluorescence is at a minimum if the liquid crystal molecules are perpendicular to the plane of polarization or perpendicular to the substrate plane. In Figure 5.11 (a), the brightest areas imply that the molecules in these areas are oriented parallel to the upper or lower edge of the image (and perpendicular to the axes of the hemicylinders). Since the dark areas in between remain dark when the plane of polarization is rotated, the molecules in these areas must be oriented perpendicular to the substrate plane. These results correspond exactly to the observations expected for the smooth hemicylinder structures shown in Figure 5.1.

Figure 5.11 (b) and (c) show slightly thicker films. In the confocal microscopy images, one can discern darker structures within the bright stripes. When the plane of polarization is rotated, the fluorescence intensity changes and by a rotation by 90° , the fluorescence intensities of the former brighter or darker regions are swapped. This behaviour, which is illustrated in Figure 5.12, indicates the presence of different in-plane orientations of the liquid crystal molecules. A schematic drawing of these orientations is shown in Figure 5.12 (b). These results could indicate the presence of incomplete or strongly asymmetric focal conic domains.

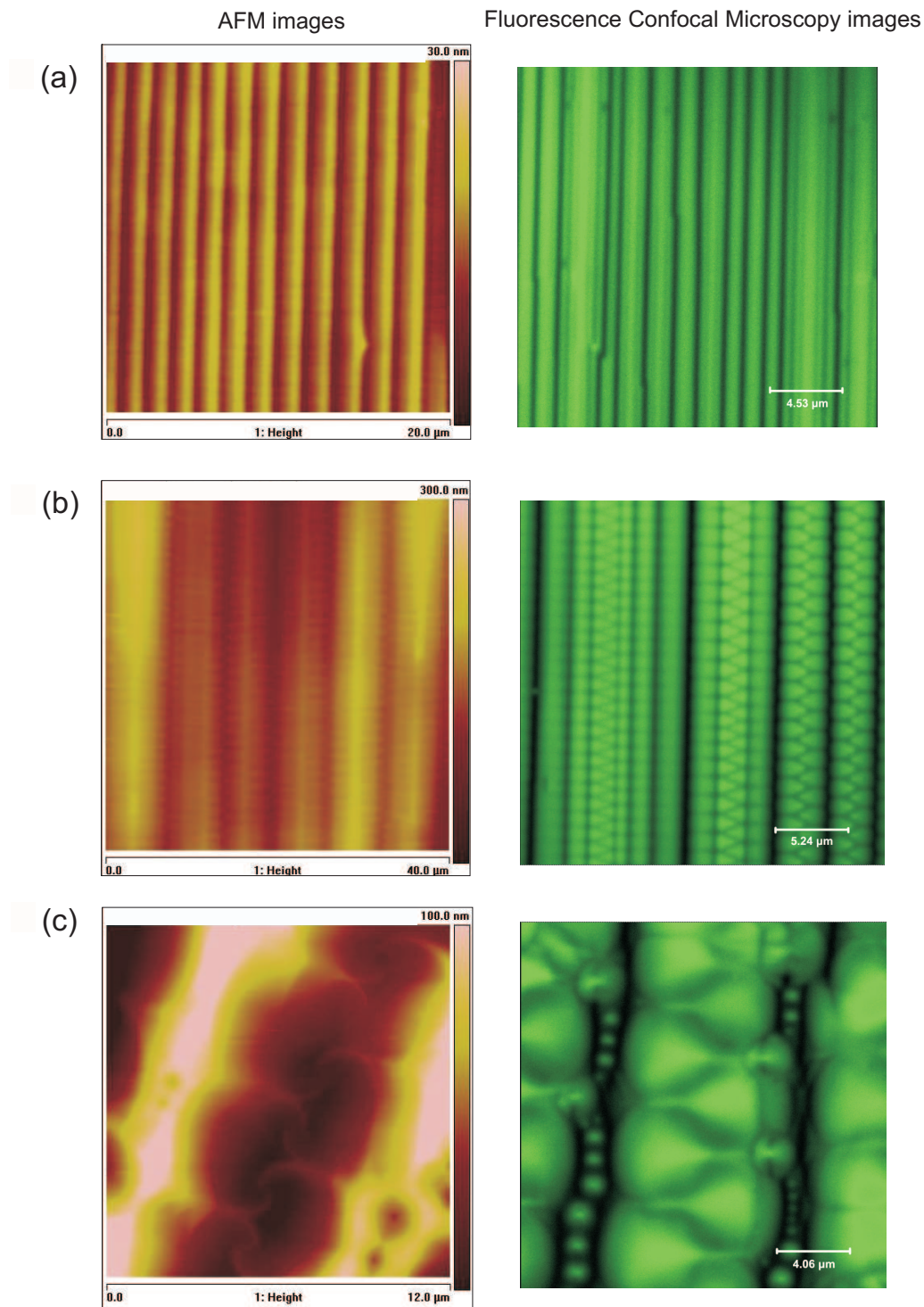


Figure 5.11: AFM and polarized fluorescence confocal microscopy images of smectic 8CB films (doped with the dye BTBP) on MoS₂ substrates. From (a) to (c), the thickness of the film increases, and are approximately 200 nm, 1 μm and 1.5 μm , respectively.

One reason why the smooth hemicylinder structure observed in thin films converts with increasing film thickness into a structure dominated by focal conic domains may consist in the energy that is to be paid for the presence of the singular planes separating neighboring hemicylinder domains. A singular plane costs much more energy than an arrangement of singular lines. With increasing film thickness, the smectic film can form a transition region near the substrate in which the uniaxial planar anchoring at the substrate surface transforms into a multidirectional planar anchoring which can be the base for the formation of focal conic domains. Thus, in thicker films, the singular planes separating the hemicylinder domains can be replaced by the singular lines of focal conic domains. However, more detailed experimental studies are needed on this point.

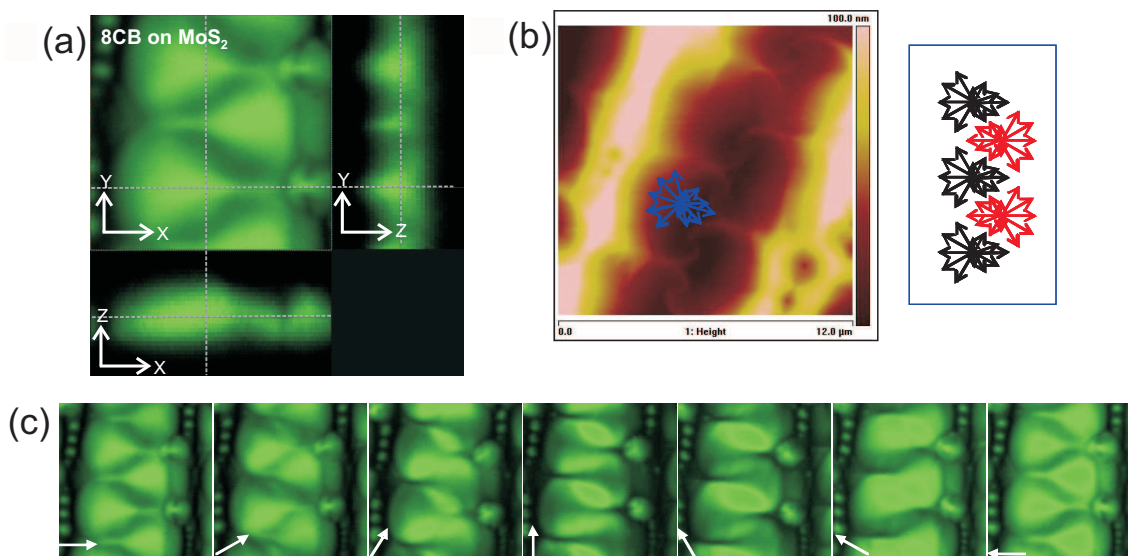
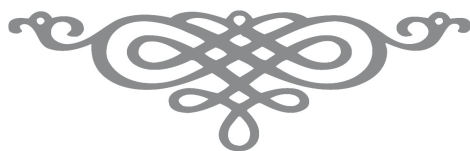


Figure 5.12: (a) and (c) are polarized fluorescence confocal microscopy images of smectic 8CB films on MoS_2 substrates. The bottom and the right side images of (a) are vertical sections, which were obtained from the vertical scan along the grey lines. The white arrows in (c) indicate the orientation of the plane of polarization. (b) is an AFM image of the corresponding area of the confocal microscopy images. The arrows indicate orientations of the liquid crystal molecules near the MoS_2 substrate which could explain the behaviour observed in the confocal microscope on rotation of the plane of polarization.

In this chapter, smectic-A liquid crystal on crystalline substrates were investigated. On such substrates, liquid crystal molecules prefer to align parallel to the surface and point into a

certain direction. in thin film, hemicylinder structure (linear defects) was found, while in thick film, circular focal conic domains presented. Between these two region, corrugated structure formed. Similar to those obtained on silicon substrates, the distance between two neighboring linear defects increase with the increase of film thickness, and the corrugated patterns became more pronounced. Fluorescence confocal microscopy implies the presence of incomplete or strongly asymmetrical focal conic domains at the transition region. It might be attributed to high energy cost of the hemicylinder structure, which induces the degeneration of the uniaxial planer anchoring into multidirectional planar anchoring with the thickness increasing. Thus the singular planes separating the hemicylinder domains can be replaced by the singular lines of focal conic domains.



Chapter 6

Summary and Outlook

"I am not bothered by the fact that I am unknown. I am bothered when I do not know others."

Analects of Confucius

This thesis presents an experimental study of fundamental properties of focal conic domains in smectic liquid crystal films on solid substrates. Focal conic domains are structures in smectic phases, and consist of a complex arrangement of the smectic layers which are wrapped around two singular lines, an ellipse and a hyperbola passing through each other focal point. These structures are believed to play an important role in the future development of novel self-assembling soft matter systems. The general goal of my work was to explore possible methods for the control of the dimensions and the spatial arrangement of focal conic domains in smectic films, and to study how their behavior depends on properties of the liquid crystal compounds, e. g., on their phase types and phase sequence. Since the formation and properties of focal conic domains depends on the anchoring conditions of the liquid crystal molecules on the substrate, an essential issue was the variation of these conditions. The main experimental method was AFM which enables the determination of the diameter of the focal conic domains, of the depth of the domain-induced depression in the film/air interface, and (under certain conditions) of the film thickness.

Focal conic domains form in smectic films in response to antagonistic molecular anchoring conditions: homeotropic anchoring at the film/air and degenerate planar at the film/substrate interface. On substrates possessing a planar anchoring condition homogeneously on the whole surface, the relation between the diameter of the focal conic domains and the thickness of the smectic film was studied. Focal conic domains are formed if the film thickness exceeds a

certain threshold. Above this threshold, the domain diameter increases linearly with increasing film thickness. By coating the substrate with mixtures of two different silane compounds, the anchoring strength of the liquid crystal molecules on the substrate could be varied systematically. With decreasing strength of the planar anchoring, the thickness threshold for the formation of focal conic domains increases and the slope of the linear diameter/thickness relation decreases. The experimental behavior could be well described by a theoretical model enabling the quantitative determination of the molecular anchoring strength. For a given smectic liquid crystal, a linear relation between the anchoring strength and the composition of the silane coating layer on the substrate is observed. The slope of this linear relation was found to depend on the molecular structure of the liquid crystal compound; longer molecules showed an extended range of planar anchoring.

Because of the curvature of the smectic layers, a depression in the film/air interface is present above each focal conic domain. The study of the depth of this depression allows conclusions about the elastic modulus which controls the compression/dilation of the smectic layers. The depression depth was measured for several liquid crystal compounds showing a variety of different phases and phase transitions. In compounds showing a second-order smectic-A – nematic transition, a pronounced decrease of the depression depth on approaching the transition was observed. This behavior indicates a softening of the smectic layers, since a dilation of the layers leads to a decrease of the depression depth. In compounds showing a first-order smectic-A – nematic transition, this behavior is not observed. These measurements enable an estimation of the static value of the layer compression/dilation modulus which was found to be one to two orders of magnitude smaller than the value measured by dynamical methods in the kHz range. The case of a smectic-C – smectic-A transition was also studied in three compounds, but conclusive results were not obtained since a decrease, as well as an increase, of the depression depth was observed.

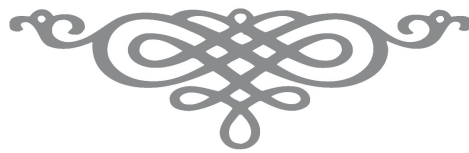
The above described studies were carried out with substrates on which focal conic domains formed in the whole surface area. I have designed a method to control the spatial arrangement of focal conic domains by creating an anchoring pattern on the substrate surface. This can be done by coating a silicon wafer (possessing planar anchoring conditions) partly with a thin gold layer. On the gold surface, the liquid crystal molecules show a homeotropic anchoring. The planar and homeotropic anchoring pattern translates into a presence (silicon region) and absence (gold region) pattern of focal conic domains in the film. The anchoring pattern has two main effects: first, the position of the focal conic is determined in the sense that they form only above the uncoated regions of the substrate; second, the size of the focal conic domains cannot

exceed the dimensions of the uncoated substrate regions. In contrast to the behaviour on non-patterned substrates, where the diameter of focal conic domains increases with the thickness of the smectic film, the diameter of focal conic domains in films on patterned substrates increases only until reaching a certain film, at which the diameter becomes comparable to the dimension of the pattern. On further increasing the film thickness, the domain diameter stays constant, but the depth of the domain-induced depressions decreases (because the curvature of the smectic layers at the surface decreases with increasing film thickness). In this way, the position as well as the diameter and, to some extent, the depression depth of the focal conic domains can be controlled.

Finally, I described preliminary results obtained on crystalline substrates, mica and MoS₂, possessing uni- or multi-directional planar anchoring conditions. On such substrates, all liquid crystal molecules are aligned parallel to the surface and point into one direction. In thin films, it was observed that the smectic layer planes bend and form a system of concentric hemicylinders, while in thick films, circular focal conic domains, similar to those obtained on silicon substrates, are formed. In the transition region between the regions with linear structures and circular focal conic domains, more complicated defect structures with corrugated patterns are observed. With increasing thickness of the liquid crystal film, the distance between the linear defects gets larger and the corrugated pattern becomes more pronounced, and finally ends with the formation of circular conic domains. Fluorescence confocal microscopy measurements indicated the presence of incomplete or strongly asymmetric focal conic domains at the transition region. This behavior might result from the larger energy cost of the hemicylinder structure in which the linear domains are separated by singular walls. With increasing film thickness, the influence of the uniaxial planar anchoring decreases and the singular walls become unstable with respect to the formation of circular focal conic domains and their singular lines (which cost considerably less energy than singular walls).

On-going and future work Based on the above investigations, I started some more detailed work on the behavior of smectic-*C* liquid crystals on silicon and MoS₂ substrates, parts of which were demonstrated in this thesis. In contrast to the smooth focal conic domains of the smectic-*A* phase, focal conic domains can exhibit more complex structures in the smectic-*C* phase, e. g., some smectic-*C* focal conic domains show a kind of ‘coffee filter’ structure in their surface. Also, the temperature dependence of the domain induced depression depth varies strongly in the smectic-*C* phases of different compounds. More systematical research is required.

In order to understand fully the inner structure of focal conic domains, more detailed polarized fluorescence confocal microscopy studies are needed. Furthermore, confocal microscope studies have been started of smectic liquid crystals doped with different kinds of dyes or quantum dots (e. g., CdSe), which could be expected to aggregate at the singular lines of the focal conic domains. Also the assembly of microparticles with the help of focal conic domains is under exploration.



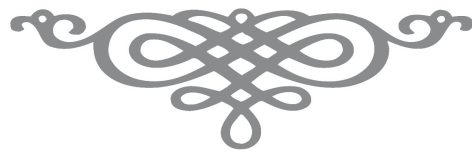
Appendices

Appendix A

Symbols and notations

Symbol	Description	value / unit
B	Compressibility/dilation modulus	N/m^2
$\mathbf{n}(\mathbf{r}), \mathbf{n}$	director	–
f	Free energy density	J/m^3
F	Free energy of a focal conic domain	J
T	Temperature	degree centigrade ($^{\circ}C$)
T_0	Phase transition temperature	degree centigrade ($^{\circ}C$)
T_{NI}	Nematic – isotropic phase transition temperature	degree centigrade ($^{\circ}C$)
T_{AN}	Smectic-A – nematic phase transition temperature	degree centigrade ($^{\circ}C$)
T_{SI}	Smectic – isotropic phase transition temperature	degree centigrade ($^{\circ}C$)
v	Volume	m^3
S	Order parameter	–
θ	Angle	degree
$\mathbf{x}, \mathbf{y}, \mathbf{z}$	Cartesian coordinates	–
K_1, K_2, K_3	Splay, twist and bend elastic moduli	J/m
π	Mathematical constant	≈ 3.14159
H	Thickness	m
H_c	Critical thickness	m

r	Radius	m
r_c	Critical radius	m
h	Depression depth	m
h_0	Idealized depression depth	m
d	Thickness of smectic layer	m
d_0	Equilibrium thickness of smectic layer	m
e	Layer dilation, $(d - d_0)/d_0$	–
k_B	Boltzmann constant	1.38×10^{-23} J/K
a	Sum of the curvatures, $1/R_1 + 1/R_2$	1/m
R_1, R_2	Radii of curvature	m
k	Elastic constant	N/m
\parallel, \perp	Parallel and perpendicular	–
σ_{air}	Air / smectic-A surface tension	J/m ²
σ_{sub}	Surface tension on substrates	J/m ²
$\Delta\sigma_{sub}$	Surface energy difference between \parallel and \perp	J/m ²
ρ	r/H	–
α, β	Dimensionless constants	–
A	Area	m ²
φ	$B = B_0(T - T_0)^\varphi$	–
x	Mol fraction of composition	–
I	Fluorescence intensity	–
ϕ	Angle between the director and polarization direction	degree
N	Force	kg m/s ² (N)
l	Vertical displacement	m
U	Van der Waals potential energy	J
Z	Distance between AFM tip and sample	m
m	mass	kg
i_0	Free amplitude	V
i_{sp}	Amplitude at set point	V
ν	Frequency	Hz
ν_0	Resonance frequency	Hz
γ_{sp}	A_{sp}/A_0	–
ΔW_{surf}	Energy gain by a decrease of the surface area	J
ΔW_{dil}	Energy cost for dilation	J
L_α, L_β	Crystalline stack of mica	–



References

- [1] P. Poulin, H. Stark, T. C. Lubensky and D. A. Weitz, *Science*, **275**, 1770 (1997).
- [2] I. Muševič, M. Škarabot, U. Tkalec, M. Ravnik and S. Žumer, *Science*, **313**, 954 (2006).
- [3] F. Reinitzer, *Monatshefte für Chemie (Wien)*, **9**, 421 (1888).
- [4] T. J. Sluckin, D. A. Dunmur and H. Stegemeyer, *Crystals that Flow: Classic papers from the history of liquid crystals*, Taylor & Francis, London, (2004).
- [5] G. H. Brown and W. G. Shaw, *Chem. Rev.*, **57** (6), 1049 (1957).
- [6] M. Schadt and W. Helfrich, *Appl. Phys. Lett.*, **18**, 127 (1977).
- [7] G. W. Gray, K. J. Harrison and J. A. Nash, *Electronics Lett.*, **9**, 130 (1973).
- [8] T. P. Brody, *Information Display*, **13**, 28 (1997).
- [9] C. A. Smith, *Circuit World*, **34**, 35 (2008).
- [10] J. A. Castellano, *Liquid Gold: The Story of Liquid Crystal Displays and the Creation of an Industry*, World Scientific Publishing, (2005).
- [11] G. T. Roberts and R. A. East, *J. of Spacecraft and Rockets*, **33**, 761 (1996).
- [12] B. Bahadur, *Liquid Crystals-Applications and Uses*, World Scientific, Singapore, (1991).
- [13] P. J. Collings and I. Hird, *Introduction To Liquid Crystals*, CRC Press, (1997).
- [14] G. Friedel, *Ann. Phys. (Paris)*, **18**, 273 (1922).

- [15] S. Chandrasekhar, *Liquid Crystals*, Cambridge University Press, (1977).
- [16] P. G. de Gennes, *The Physics of Liquid Crystals*, Clarendon Press, Oxford (1974).
- [17] I. Dierking, *Textures of Liquid Crystals*, Wiley-VCH, New York, (2003).
- [18] H. Marynissen, J. Thoen and W. Van Dael, *Mol. Cryst. Liq. Cryst.*, **124**, 195 (1985).
- [19] V. A. Berenberg and A. P. Onokhov, *J. Opt. Tech.*, **68**, 672 (2001).
- [20] D. K. Yoon, M. C. Choi, Y. H. Kim, M. W. Kim, O. D. Lavrentovich and H.-T. Jung, *Nature Materials*, **6**, 866 (2007).
- [21] C. W. Oseen, *Trans. Faraday Soc.*, **29**, 883 (1933).
- [22] H. Zöcher, *Trans. Faraday Soc.*, **29**, 945 (1933).
- [23] F. C. Frank, *Disc. Faraday Soc.*, **25**, 19 (1958).
- [24] J. L. Erichsen, *Arch. Rational Mech. Anal.*, **4**, 231 (1960).
- [25] J. L. Erichsen, *Trans. Soc. Rhelo.*, **5**, 23 (1961).
- [26] F. M. Leslie, *Quart. J. Mech. Appl. Math.*, **19**, 357 (1966).
- [27] F. M. Leslie, *Arch. Rational Mech. Anal.*, **28**, 265 (1968).
- [28] L. M. Blinov, *Electro-optical and magneto-optical properties of liquid crystals*, John Wiley and Sons, New York, (1983).
- [29] P. G. de Gennes, *The Physics of Liquid Crystals*, Clarendon Press, Oxford, p. 314 (1974).
- [30] J. W. Goodby, M. A. Waugh, S. M. Stein, E. Chin, R. Pindak and J. S. Patel, *Nature (London)*, **337**, 449 (1989).
- [31] F. Brochard, *J. Phys. (Paris)*, **34**, 411 (1973).
- [32] D. Davidov, C. R. Safinya, M. Kaplan, S. S. Dana, R. Schaetzing, R. J. Birgeneau and J. D. Litster, *Phys. Rev. B*, **19**, 1657 (1979).
- [33] H. von Känel and J. D. Litster, *Phys. Rev. A*, **23**, 3251 (1981).

-
- [34] H. Birecki, R. Schaetzing, F. Rondelez and J. D. Litster, *Phys. Rev. Lett.*, **36**, 1376 (1976).
- [35] H. J. Fromm, *J. Phys. (Paris)*, **48**, 647 (1987).
- [36] M. E. Lewis, I. Khan, H. Vithana, A. Baldwin, D. L. Johnson and M. E. Neubert, *Phys. Rev. A*, **38**, 3702 (1988).
- [37] M. Benzekri, J. P. Marcerou, H. T. Nguyen and J. C. Rouillon, *Phys. Rev. B*, **41**, 9032 (1990).
- [38] M. R. Fisch, P. S. Pershan and L. B. Sorensen, *Phys. Rev. A*, **29**, 2741 (1984).
- [39] L. Ricard and J. Prost, *J. Phys. (Paris)*, **42**, 861 (1981).
- [40] L. Ricard and J. Prost, *J. Phys. (Paris)*, **40**, C3-83 (1979).
- [41] D. Rogez, D. Collin and P. Martinoty, *Eur. Phys. J. E*, **14**, 43 (2004).
- [42] R. Bartolino and G. Durand, *Phys. Rev. Lett.*, **39**, 1346 (1977).
- [43] N. A. Clark, *Phys. Rev. A*, **14**, 1551 (1976).
- [44] M. R. Fisch, L. B. Sorensen and P. S. Pershan, *Phys. Rev. Lett.*, **47**, 43 (1981).
- [45] M. R. Fisch, L. B. Sorensen and P. S. Pershan, *Phys. Rev. Lett.*, **48**, 943 (1982).
- [46] F. Beaubois, T. Claverie, J. P. Marcerou, J. C. Rouillon, H. T. Nguyen, C. W. Garland and H. Haga, *Phys. Rev. E*, **56**, 5566 (1997).
- [47] P. Martinoty, J. L. Gallani and D. Collin, *Phys. Rev. Lett.*, **81**, 144 (1998).
- [48] P. Sonntag, D. Collin and P. Martinoty, *Phys. Rev. Lett.*, **85**, 4313 (2000).
- [49] S. Shibahara, J. Yamamoto, Y. Takanishi, K. Ishikawa and H. Takezoe, *J. Phys. Soc. Jpn.*, **71**, 802 (2002).
- [50] S. Shibahara, J. Yamamoto, Y. Takanishi, K. Ishikawa, H. Takezoe and H. Tanaka, *Phys. Rev. Lett.*, **85**, 1670 (2000).
- [51] R. Bartolino and G. Durand, *J. Phys. (Paris)*, **45**, 889 (1984).

- [52] B. Jérôme, *Rep. Prog. Phys.*, **54**, 391 (1991).
- [53] C. Mauguin, *C. R. Acad. Sci. (Paris)*, **156**, 1246 (1913).
- [54] L. M. Blinov, N. N. Davodora, A. A. Sonin and S. G. Yudin, *Sov. Phys. Crystallogr.*, **29**, 320 (1984).
- [55] J. Cognard, *Mol. Cryst. Liq. Cryst. Suppl.*, **1**, 1 (1982).
- [56] J. Cheng and G. D. Boyd, *Appl. Phys. Lett.*, **135**, 444 (1979).
- [57] S. Koshida Nand Kibui, *Appl. Phys. Lett.*, **40**, 541 (1982).
- [58] H. A. van Sprang, *Mol. Cryst. Liq. Cryst.*, **97**, 255 (1983).
- [59] G. Porte, *J. Physique*, **37**, 1245 (1976).
- [60] E. K. Frolova, O. G. Sarbey and A. S. Sybashvily, *Mol. Cryst. Liq. Cryst.*, **104**, 111 (1984).
- [61] H. Yokoyama, S. Kobayashi and H. Kamei, *J. Appl. Phys.*, **56**, 2645 (1984).
- [62] B. Jérôme, P. Pieranski and M. Boix, *Europhys. Lett.*, **5**, 693 (1988).
- [63] L. M. Blinov and A. A. Sonin, *Mol. Cryst. Liq. Cryst.*, **179**, 13 (1990).
- [64] B. Jérôme and P. Pieranski, *J. Physique*, **5**, 1601 (1988).
- [65] B. Jérôme and P. Pieranski, *Liq. Cryst.*, **5**, 683 (1989).
- [66] J. S. Foster and J. E. Frommer, *Nature*, **333** 542 (1988).
- [67] J. K. Spong, Jr L. J. Lacombe, M. M. Dovek, J. E. Frommer and J. S. Foster *J. Physique*, **59**, 2139 (1989).
- [68] J. K. Spong, H. A. Mires, Jr L. J. Lacombe, M. M. Dovek, J. E. Frommer and J. S. Foster, *Nature*, **338**, 137 (1989).
- [69] D. P. E. Smith, J. K. H. Harber, G. Binnig and H. Nejo, *Nature*, **344**, 641 (1990).
- [70] D. P. E. Smith, J. K. H. Harber, C. Gerber and G. Binnig, *Science*, **245** 43 (1989).

-
- [71] M. Hara, Y. Iwakabe, K. Tochigi, H. Sasahe, A. F. Garito and A. Yamada, *Nature*, **344**, 228 (1990).
- [72] D. P. E. Smith and W. M. Heckl, *Nature*, **346**, 616 (1990).
- [73] J. M. Geary, J. M. Goodby, A. Kmetr and J. S. Rand Patel, *J. Appl. Phys.*, **62**, 4100 (1987).
- [74] N. A. Clark, *Phys. Rev. Lett.*, **55**, 292 (1985).
- [75] P. Guyot-Sionnest, H. Hsiung and Y. R. Shen, *Phys. Rev. Lett.*, **57**, 2963 (1986).
- [76] C. S. Mullin, P. Guyot-Sionnest and Y. R. Shen, *Phys. Rev. A*, **39**, 3745 (1989).
- [77] W. Chen, M. Feller, P. Guyot-Sionnest, C. S. Mullin, H. Hsiung and Y. R. Shen, *Photochemistry in thin films SPIE*, **1056**, 104 (1989).
- [78] W. Chen, M. Feller and Y. R. Shen, *Phys. Rev. Lett.*, **63**, 2665 (1989).
- [79] H. Hsiung and Y. R. Shen, *Phys. Rev. A*, **34**, 4303 (1986).
- [80] F. J. Kahn, *Appl. Phys. Lett.*, **22**, 386 (1973).
- [81] C. E. Williams and M. Kleman, *J. de Physique*, **36**, 315 (1975).
- [82] Y. Bouligand, *J. Phys. (Paris)*, **33**, 525 (1972).
- [83] M. Kleman, *Rep. Prog. Phys.*, **52**, 555 (1989).
- [84] Z. Li and O. D. Lavrentovich, *Phys. Rev. Lett.*, **73**, 280 (1994).
- [85] J. B. Fournier, I. Dozov and G. Durand, *Phys. Rev. A*, **41**, 2252 (1990).
- [86] M. C. Choi, T. Pfohl, Z. Wen, Y. Li, M. W. Kim, J. N. Israelachvili and C. R. Safinya, *Proc. Natl. Acad. Sci. U.S.A.*, **101**, 17340 (2004).
- [87] T. Pfohl, J. H. Kim, M. Yasa, H. P. Miller, G. C. L. Wong, F. Bringezu, Z. Wen, L. Wilson, M. W. Kim, Y. Li and C. R. Safinya, *Langmuir*, **17**, 5343 (2001).
- [88] S. Shojaei-Zadeh and S. L. Anna, *Langmuir*, **22**, 9986 (2006).

- [89] Y. H. Kim, D. K. Yoon, M. C. Choi, H. S. Jeong, M. W. Kim, O. D. Lavrentovich, and H.-T. Jung, *Langmuir*, **25**, 1685 (2009).
- [90] J. P. Bramble, S. D. Evans, J. R. Henderson, T. J. Atherton and N. J. Smith, *Liq. Cryst.*, **34**, 1137 (2007).
- [91] V. Designolle, S. Herminghaus, T. Pfohl and Ch. Bahr, *Langmuir*, **22**, 363 (2006).
- [92] B. Zappone and E. Lacaze, *Phys. Rev. E*, **78**, 061704 (2008).
- [93] J. P. Michel, E. Lacaze, M. Alba, M. de Boissieu, M. Gailhanou and M. Goldmann, *Phys. Rev. E*, **70**, 011709 (2004).
- [94] E. Lacaze, J.-P. Michel, M. Alba and M. Goldmann, *Phys. Rev. E*, **76**, 041702 (2007).
- [95] J. P. Michel, E. Lacaze, M. Goldmann, M. Gailhanou, M. de Boissieu and M. Alba, *Mol. Cryst. Liq. Cryst.*, **437**, 99 (2005).
- [96] M. Kleman, *J. Phys. (Paris)* **38**, 1511 (1977).
- [97] U. C. Fischer and H. P. Zingsheim, *J. Vac. Sci. Technol.*, **19**, 881 (1981).
- [98] H.W. Deckman and J. H. Dunsmuir, *Appl. Phys. Lett.*, **41**, 377 (1982).
- [99] F. Burmeister, W. Badowsky, T. Braun, S. Wieprich, J. Boneberg and P. Leiderer, *Appl. Surf. Sci.*, **144**, 461 (1999).
- [100] I. I. Smalyukh, S. V. Shiyankovskii and O. D. Lavrentovich, *Chem. Phys. Lett.*, **336**, 88 (2001).
- [101] E. J. G. Peterman, H. Sosa and W. E. Moerner, *Ann. Rev. Phys. Chem.*, **55**, 79 (2004).
- [102] R. D. Goldman and D. L. Spector, *Live Cell Imaging: A Laboratory Manual*, New York, Cold Spring Harbor Press, (2005).
- [103] G. Binning, C. F. Quate and Ch. Gerber, *Phys. Rev. Lett.*, **56**, 930 (1986).
- [104] F. J. Giessible, *Science*, **267**, 68 (1995).
- [105] S. Morita, R. Wiesendanger and E. Meyer, *Noncontact Atomic Force Microscopy*. Berlin: Springer, (2002).

-
- [106] C. W. Yang, I. S. Hwang, Y. F. Chen, C. S. Chang and D. P. Tsai, *Nanotechnology*, **18**, 084009 (2007).
- [107] S. M. Hues, R. J. Colton, E. Meyer and H.-J. Guntherodt, *MRS Bulletin*, **18**, 41 (1993).
- [108] A. J. G. Mank, *Scanning Probe Microscopy (SPM) – an overview of possibilities*, Philips.
- [109] J. S. Barash, *Van der Waals forces*, Moscow, Nauka, (1998).
- [110] V. L. Mironove, *Fundamentals of Scanning Probe Microscopy*, NT-MDT Company, Moscow, Russia.
- [111] *A Practical Guide to SPM*, www.veeco.com, Veeco Instruments.
- [112] D. J. Müller, G. Büldt and A. Engel, *J. Mol. Bio.*, **249**, 239 (1995).
- [113] F. A. Schabert, C. Henn and A. Engel, *Science*, **268**, 92 (1995).
- [114] Z. Shao, J. Mou, D.M. Czajkowsky, J. Yang and J.-Y Yuan, *Advances in Physics*, **45**, 1 (1996).
- [115] S. Herminghaus, A. Fery and D. Reim, *Ultramicroscopy*, **69**, 211 (1997).
- [116] F. Schneider, *Rev. Sci. Instr.*, **73**, 114 (2002).
- [117] B. Alkhairalla, H. Allinson, N. Boden, S. D. Evans and J. R. Henderson, *Phys. Rev. E*, **59**, 3033 (1999).
- [118] J. E. Proust and E. Perez, *J. Phys. (Paris) Lett.*, **38**, L-91 (1977); E. Perez and J. E. Proust, *ibid.*, L-117.
- [119] O. D. Lavrentovich, *Sov. Phys. JETP*, **64**, 984 (1986).
- [120] O. D. Lavrentovich, *Mol. Cryst. Liq. Cryst.*, **151**, 417 (1987).
- [121] H. P. Hinov, *J. Phys. (Paris)*, **42**, 307 (1981).
- [122] P. Oswald and L. Lejček, *Eur. Phys. J. E*, **19**, 441 (2006).
- [123] D. Rogez, L. G. Benguigui and P. Martinoty, *Eur. Phys. J. E*, **16**, 193 (2005).

-
- [124] J. B. Fournier, *Phys. Rev. E*, **50**, 2868 (1994).
- [125] J. Kumaki and T. Hashimoto, *J. Am. Chem. Soc.*, **125**, 4907 (2003).
- [126] N. H. Thomson, S. Kasas, B. Smith, H. G. Hansma and P. K. Hansma, *Langmuir*, **12** (24), 5905 (1996).
- [127] P. Pieranski and B. Jérôme, *Phys. Rev. A*, **40**, 317 (1989).
- [128] E. B. Sirota, P. S. Pershan, L. B. Sorensen and J. Collett, *Phys. Rev. A*, **36**, 2890 (1987).



Acknowledgments

“Ich habe oft die Ernte eingebracht, für die andere gesät hatten. Mein Werk ist das eines Kollektivwesens...”

Johann Wolfgang von Goethe (1749 – 1832)

As time is flying, I am about to finish my doctoral program, it can not be completed without expressing my gratitude to all who have helped me greatly to finish this thesis.

First of all, I would like to state my appreciation to my supervisor *Prof. Dr. Stephan Herminghaus* for giving me the opportunity to conduct the interesting research under his supervision. His visionary guidance and profound knowledge are of great help to me. I also want to thank ‘*Max-Planck-Institut für Dynamik und Selbstorganization*’ (*MPI für DS*) for accepting me to be a member of this glorious institution, and providing with all kinds of necessary support. The research atmosphere and flexible environment deeply attracted me, and inspired me enormously to realize self-fulfilment during my study. And I am deeply grateful to *MPI für DS* for supporting me with the grant ‘*Max Planck Fellowship*’, and also to *Deutsche Forschungsgemeinschaft (DFG)* for the financial support.

I am in great debt to my Guide *Dr. Christian Bahr*. Without his enthusiastic guidance, I could not choose this topic and begin the thesis. He has given me all the freedom and independence to work in my own way. Whenever I approached him with a problem, he was always ready to help me out from any kind of situations. Also thanks for his patient and careful revisal of this thesis. Furthermore, his kind help made my stay in Germany easier, when I had any problems in understanding German.

Next I would like to thank the support and collaboration with *Dr. Martin Brinkmann*. His theoretical and stimulating discussion helped greatly in the data analyzing. I am grateful to *Dr. Yasutaka Iwashita* for his helpful suggestions on my experiments. We had many interesting discussions.

I also want to express my gratitude to my wonderful colleagues, Dr. Rolf Dootz, Dr. Dagmar Steinhauser, Dr. Khare Krishnacharya, Eric, Dr. Surenjav Enkhtuul, Semra, Konstantina, Habibollah, Sravanti, Shashi, Mario, Marcus and Wolf for their invaluable support and help during my stay in Göttingen. They helped me a lot with my research and my personal issues. Among their company, I never felt alone, and enjoyed myself during my doctoral life.

I want to give my special thanks to our secretary Monika. When I had any problems, she was always there. And her kindness and warm-heart made me feel at ease.

I can not forget to devote my gratitude to my Chinese colleagues, Kai and Shuang, and their family Nian and Dongxia. I shall not forget the dinners we had together, especially the New Year get-together. The wonderful cooking gave me many surprises and made me feel at home.

It would not end without thanking my Chinese friends in Göttingen for their social support and valuable suggestions. Among them are Xiaoqin Zhang, Jiong Yan, Jun Lei, Gang Zhang, Ying Yang, Yongjiang Mao, Zhensheng Zhang, Zhifeng Xue, Xin Zhang, Heng Zhang, Yanjie Zhang, and Wangda Zuo. We spent a lot of happy time, including going leek trips, hiking, having picnics, playing badminton, having parties etc.. I would never forget when I came here, they showed me around in the city, invited me to join all kinds of activities, and gave me many kitchenware. With their warm help, I could settle down in Göttingen quickly. Even though some of them have left Germany, I will remember them and our friendship for ever.

Last but not least, I wish to express my love and gratitude to my family. I am particularly indebted to my parents. Without their selfless support and encouragement, I can not reach at this stage of my life. I thank them for their countless patience and never-ending support towards achieving this goal. It was my parents' dream to see 'Doctor' in front of my name. I dedicate this thesis to them. I can never forget their sacrifices for the betterment of my life.

I also give special thanks to my husband Shaoxian. Without his unflinching encouragement, I would not start my doctoral study and succeed in completing my thesis. Thank him for revising this thesis as well. He has been giving me tremendous support and constant source of courage in my life. His encouragement and understanding inspired me to achieve my dream, and his suggestions made me recognize my abilities to try hard and get ahead. I also would like dedicate this thesis to him for his love.

I would like to thank all who contribute to this thesis, in my deep heart, for everything.

Wei Guo
in Göttingen

Erklärung

1. Ich habe diese Arbeit selbständig und ohne unerlaubte Hilfe angefertigt und dabei nur die angegebenen Quellen benutzt.
2. Ich habe noch keinen Promotionsversuch unternommen.

Göttingen, den 3 June 2009.

Wei Guo

Scientific Papers Published :

1. W. Guo, S. Herminghaus, and C. Bahr, '*Controlling Smectic Focal Conic Domains by Substrate Patterning*', *Langmuir*, **24**, 8174 (2008).
2. W. Guo, and C. Bahr, '*Influence of Anchoring Strength on Focal Conic Domains in Smectic Films*', *Phy. Rev. E*, **79**, 011707 (2009).
3. W. Guo, and C. Bahr, '*Influence of Phase Sequence on Focal Conic Domains in Smectic Films*', *Phy. Rev. E*, **79**, 061701 (2009).

Lebenslauf

Persönlicher Status

Name : Wei Guo
Geburtsdatum : 17 Februar, 1979
Geburtsort : Jinan, Shandong, China
Wohnort : Königsbergerstr. 1, 37083 Göttingen
Staatsangehörigkeit : Chinesisch

Ausbildung

Feb. 2006 – seit Doktorarbeit am Max-Planck Institut für Dynamik und Selbstorganisation, Göttingen.
(Betreuer: Dr. Christian Bahr und Prof. Dr. Stephan Herminghaus).

2004 – 2005 Junior Researcher am Chemistry Engineering and Chemistry, Technische Universität Eindhoven, The Netherlands.
(Betreuer: Prof. Dr. Ulrich S. Schubert).

2001 – 2004 Masterarbeit in Physikalische Chemie am Jilin University, Changchun, China.
(Betreuer: Prof. Yubai Bai).

1997 – 2001 Bachelor in Chemie am Jilin University, Changchun, China.